MASTER DEGREE THESIS IN NUCLEAR PHYSICS

DEPARTMENT OF PHYSICS AND TECHNOLOGY

UNIVERSITY OF BERGEN

Simulation of prompt gamma production in particle therapy and beam trajectory imaging

Author:
Martin Ssentongo

Supervisor:
Professor Dieter Rohrich

June 1, 2015

Abstract

In cancer oncology, using of Mega electron Volt (MeV) bremsstrahlung photons has been clinically practised on cancer patients since photons can deliver a significant dose to tumour volumes when projected into the body in several beam directions as in techniques such as Intensity Modulated Radio Therapy (IMRT) and Volumetric Modulated Arc Therapy (VMAT). However, photons in a single beam deposit their maximum energy just a few millimetres at the beam's body entrance and a decreasing dose deposition beyond the tumour site. Cancer research and clinical practice have resorted to use of charged particles like protons and carbon ion beams for cancer therapy since they deposit a large fraction of their energy at their extreme range in a Bragg peak with very less dose deposition after the Bragg peak targeted to the tumour. This ensures maximum dose to tumour for therapy and spares organs at risk in both forward and behind the clinical target volume. The intention of this study is to demonstrate the feasibility of prompt gamma imaging for the online verification of the Bragg peak position. In order to achieve this aim, interactions of 160 MeV proton and 300 MeV/u carbon ion pencil beams within a soft tissue phantom were simulated.

Monte Carlo simulations based on FLUKA, have been performed to analyse prompt gamma radiation produced as a result of inelastic nuclear interactions during both proton and carbon ion therapy procedures. These simulations were performed with a main view of designing a prompt gamma imaging device utilizing Compton scatter events and photoelectric effect processes of gamma radiation for real time control of incident beam during hadron therapy. Such a gamma detector system is called a Compton camera which has potential to utilize high energy photons emitted out of patients during hadron therapy which has long been a constraint in Anger cameras as they are only capable to image low energy photons of about 140 keV in Single Photon Emission Computed Tomography (SPECT).

In this project, two chief objectives were to be achieved and these were: first, to present the physical and interaction characteristics of both primary beam and secondary radiation like protons, neutrons and more so prompt gammas by their angular distribution after their production and photon energy spectrum as a result of de-excitation of the different atomic nuclei of human soft tissue. The fine energy loss and inelastic nuclear interactions with tissue nuclei for both 160 MeV proton beam and 300 MeV/u carbon ion beams as they traverse through human soft tissue have also been included in these studies. The second objective which was divided into two sub-tasks was; to simulate the imaging performance of first, a High Purity Germanium (HPGE) Compton Camera and second, a single scattering Compton camera made up of a sub-detector system of silicon to act as a photon scattering detector and a germanium absorber detector. Primary beam range and photon source distribution were investigated using an iterative algorithm for reconstruction of cones using Compton scatter angle and energy deposition at Compton scattering and photoelectric effect positions in each Compton camera since reconstructed cones carried position and directional information of emitted prompt gamma radiation.

Results from the first task of this project showed that prompt gammas from soft tissue nuclei de-excitation were emitted isotropically in all directions for both proton and carbon

ion simulations of $1x10^7$ primaries with distinct peaks at 2.3 MeV, 3.6 MeV, 4.4 MeV, 5.3 MeV and 6.2 MeV which corresponded to ^{14}N, ^{20}Ca, ^{12}C, ^{14}N and ^{16}O atomic nuclei de-excitation photon energies respectively.

For a HPGE Compton camera of dimensions 32cmx8cmx32cm placed 8 cm to the top of the soft tissue phantom at orthogonal angle to the incident primary beam, data acquisition was done using gammas first Compton scattered within the detector and secondary photo-absorbed in the same germanium crystal. Only two successive interaction events were considered with a major assumption that the scattered quantum photon was completely absorbed at its second and last interaction in the germanium crystal. The number of secondary radiation that reached the detector included neutrons, electrons, positrons, protons and photons. Photons were Compton scattered in the angular range from 0^o to 180^o with low energetic photons scattered in angles greater than 90^o. The energy spectrum of photons before Compton scattering showed an energy range from 0.1 MeV to 1.6 MeV with a sharp peak at 0.2 MeV in the 160 MeV proton beam simulation. This peak was shifted to 0.18 MeV in the 300 MeV/u carbon ion simulation and both simulations exhibited a 0.511 MeV photon peak. The angular resolution of the detector measured by angular resolution measure showed that ARM values of less than 3 mm would give better photon source predictions with a clear distinct primary beam range at 16 cm depth into human soft tissue using the germanium block Compton camera while as when using the single scattering Compton camera, the ARM values less than 6 mm accurately predicted the prompt gamma production distribution in the soft tissue phantom.

Comparing the HPGe Compton camera with single scattering Compton camera in terms of photon energy range optimization for Compton cone reconstruction, the single scattering Compton camera proved to be better than the HPGe detector since it utilized photons from 0.03 MeV to 3 MeV for Compton cone reconstruction and yet the HPGe Compton camera only used a short energy from 0.1 MeV to 1.6 MeV. But single scattering Compton camera reconstruction results were affected by Doppler broadening as photons of energies less than 0.1 MeV were inclusive in the energy spectrum. The single scattering Compton camera was further found to have a better overall efficiency of 0.07% over that of HPGe Compton camera which was 0.032%. For both Compton cameras, the reconstruction source distribution tracked the original photon production distribution at the distal fall off by a precision of 0.1 mm.

Keywords: Compton camera, single scattering Compton camera, HPGE Compton camera, time of flight, angular resolution measure, Doppler broadening, spatial resolution of the Bragg peak and overall efficiency.

Acknowledgement

I would like to forward my sincerely gratitude to all the people who have helped me make this project study a success through the time duration between August-2014 and May-2015.

First, I would like to express my gratitude to my supervisor Prof. Dieter Rohrich for the useful comments, remarks, excellent ideas and engagement throughout the learning process of this Master thesis and further more for taking time to read through this project work and suggesting appropriate measures for its successful completion.

I would like also to thank Dr. Kristian Smeland Ytre-Hauge for introducing me to various concepts in FLUKA as well as for the support on the way through programming in the Fluka scripts.

I am also pleased to acknowledge Dr. Boris Wagner, for his excellent and courageous support in numerical data handling and programming in both C++ and Root. I took great courage from your ideas in how the simulation packages really worked.

Further appreciation goes to my beloved one *Julian Namatovu*, who has supported me throughout the entire project process, both by keeping me harmonious and helping me putting pieces together. I will be grateful forever for your love.

And finally lots of thanks to Sera Sarah, Dron Nor, Lucas Hoppler and all my Family members who have given me a supportive environment for my academic work. Thank you all.

Contents

1 Introduction

One of the most leading causes of high mortality rates in old aged population today is a cellular disease known as cancer. This is a complex genetic disease which leads to formation of abnormal cells in human body with a more rapid growth behavior than normal health body cells. Various causes of the complication have been cited but all pointing primarily to environmental factors that surround human life such as edible consumables like fatty foods with low fiber content and contaminated water, inhaled air and chemicals and sunlight through which carcinogens can penetrate human body. Other human behavior treated as a lifestyle such as cigarette smoking can greatly increase the risk for cancer development. A study undertaken at Cancer Malcolm Alison, Imperial college school of medicine in London, UK shows that over 90% of cancerous infections occur in the epithelial since this category of cells has a protective role in human parts such as the skin, respiratory lining and the alimentary tracts [1].

A group of cancer cells forms a tumour in a specific body site and basing on the growth behaviour of the tumour, these are categorized into two either Benign or Malignant. Benign tumours are generally slow-growing expansive masses that in most cases just compress rather than invade surrounding cells. As such they generally pose little threat, except when growing in a confined space like the skull. Unlike benign tumors, malignant tumours are rapid growing and invade surrounding cells with the ability to detach from the main primary tumour to form secondary metastases. Just like malignant tumours, some benign tumours have malignant potential, especially those occurring in the large intestine that they extend to distant regions away from the primary site. Such tumor behaviour has called for quick clinical attention through therapeutical procedures used today for treating cancer. These include surgery, chemotherapy and radiotherapy which can be combined in appropriate fractions to deliver a complete treatment to a cancer patient.

The first thought of technique for eradicating cancer cells in clinical practice was surgery. This involves mechanical and invasive approaches in which medical specialists, surgeons, physically remove cancer cells from the body part infected. In the past few years, this has been implemented in curing prostate cancer, one of the most cancer types in male patients which is treated through a medical procedure known as radical prostatectomy. Cancer surgery proves good a technique for treating benign tumors which are local to a specific organ site unlike for metastatic cancer cells that make this technique so complex to be performed on patients since cancer cells are not confined in a particular location [2]. Besides, other costs such a bleeding, increased risk for secondary metastases and mechanical damage to non cancerous organs make this single procedure downsized.

Combined to surgery is chemotherapy which involves the use of anti-cancer drugs or chemicals called cytotoxics that aim at destroying cancer cells in the patient body. Such injected or orally taken drugs into the patient's body work by interfering with the growth rate of cancer cells since tumor cells grow faster than normal cells. And this therapeutic technique comes with a merit over surgery in a way that it can be used to shrink and treat metastatic cells spread from the primary localized tumor. This procedure is normally performed in

about a month after surgery and later radiation therapy can be given to patients. This is currently used for treating breast cancer tumors both localized and metastatic in women; however chemotherapy involves introduction of chemical drugs to the whole body which may depending on the drug used, interrupt normal functioning of healthy body cells leading to some side effects such as nausea, vomiting, hair loss and body thinning [3]. This has called for a more precise advancement for delivering treatment dose to tumor cells called Radiotherapy in cancer oncology.

Radiotherapy involves the use of radio-active sources that can be placed inside a patient, a treatment technique referred to as brachytherapy in which short range radiation is used to treat tumours like prostate cancer in men, or sources placed out of the patient's body that the irradiated energy is directed towards a confined target body part of treatment interest. This is the so called teletherapy and currently for clinical use, high energy photons of upto 25 MV generated from a Mega voltage Medical LINAC using electromagnetic stationary waves are externally directed to tumour sites. This is done using several delivery techniques such as 3D conformal radiation therapy in which photon beams are directed to the same target site from several angles. Advancement in technology has upgraded treatment delivery methods to IMRT in which photon beam intensity is regulated by use of multileaf collimators to limit high doses to only the planning target volume. For better coverage of tumour volumes, Volumetric Modulated Arch Therapy (VMAT) is currently used for delivering photon dose to tumour cells using rotating gantry machines while intensity modulating the photon beam. This method is currently in use at Haukeland Hospital, Bergen for some cancer patients such as prostate cancer patients. With the due fact that photons have an exponential fall off in intensity as they penetrate matter, organs before the planning target volume receive high photon dose and those beyond the tumour volume still receive a significant dose which with time can lead to short term side effects like skin reddening, hair loss or long term side effects such as cell mutation and development of secondary cancer in patients especially the infants with still developing body cells [4]. To resolve this challenge in radiation oncology, the use of charged particles such as protons, helium and carbon ions for delivering sufficient dose to tumour volumes was performed at the HIMAC at Chiba, HIBMC at Hyogo, Gesellschaft-fur Schwerionenforschung Darmstadt (GSI) in Germany, the National Centre of Oncological Hadrontherapy (CNAO) in Pavia - Italy, and Gunma University's Heavy Ion Medical Center in Maebash for heavy ion therapy [5].

Hadron therapy for cancer treatment has progressively evolved in the field of radiation therapy as one of the recent research advances in medical physics. In some clinical set ups, radiation therapy performed by use of high energy photons has been replaced by installation of cyclotrons and synchrotrons to accelerate light and heavy charged particles like protons and carbon ions to energies of 680 MeV and 340 MeV/u respectively for clinical therapy of deeply sited tumors within the cancer patient body. This advance in radiation therapy comes with a merit of precise and increased dose deposit to cancer cells with reduced dose to organs in regions of the plateau and distal fall off of the maximum delivered dose peak at the particle range called a Bragg peak.

Due to charged particle interaction with cellular atoms in the patient body through ioniza-

tion, excitation, elastic collisions and nuclear fragmentation formation as a result of inelastic nuclei interactions, short lived positron emitters like ^{11}C, ^{15}O and ^{13}N are produced which emit positrons in short distances of a few millimeters to annihilate with abundant electrons in the patient body thus producing back to back 511 keV gammas, currently taken into use as a tool for on-line dose monitoring and particle range during hadron therapy by use of Time Of Flight - Positron Emission Tomography (TOF-PET) detectors [6]. However, the delay time lag, positron emitter metabolic washout [7] and position shift of positron from the exact spot of their production has called for use of other secondary radiation like protons and prompt gammas for real time on-line dose distribution studies and primary particle range monitoring so as to accurately position the Bragg peak in the gross target volume reducing adverse effects of secondary cancer development in Organs At Risk (OAR).

Use of charged particles for cancer therapy generates prompt gamma radiation out of the patient body of continum energy spectrum divided into three stages. High energetic gamma-rays of E>30 MeV are mainly produced during nucleon-nucleon bremsstrahlung at the very beginning of the interaction. Between 10 and 30 MeV, prompt-gamma rays are emitted during the decay of giant resonances, the so called Giant Dipole Resonances (GDR), a collective oscillation between protons and neutrons in the nucleus and below 10 MeV, the main and remaining contribution for gamma production are photons coming from the remaining excited nuclei at the final stage of the reaction [8].

The main objective of this project has been divided into two parts. First, to study physical and interaction characteristics of both primary beam and secondary radiation produced during hadron therapy using Fluka which is a Monte Carlo simulation package. Such secondary radiation included protons, neutrons and most important were the prompt gamma photons with an energy range from a few keV and 10 MeV. Secondary and finally was the objective to simulate the performance of two Compton cameras to accurately predict the origin of photons. The Compton cameras simulated were HPGe Compton camera and single scattering Compton camera using a 160 MeV proton beam or 340 MeV/u carbon ion pencil beam projected into a human soft tissue phantom.

Chapter 2 highlights radioactivity as a conceptual process in physics and how radiation produced as a result of particle decay interacts with matter. A discussion of accelerators currently in use today for production of both charged particles and uncharged radiation has been highlighted. The last section reviews the concept of energy deposition of radiation in matter and how living human tissue interacts with radiation on the cellular level.

Chapter 3 details the physics of radiation such as massless photons and charged particles like electrons, protons and carbon ions utilization for treatment of cancer cells. The amount of radiation energy deposited and absorb per unit length referred to as Linear Energy Transfer (LET) has been linked to how much biological impact a particular radiation type can affect human cells during therapeutic procedures, a term referred to as Relative Biological Effectiveness.

Production of electrons and photons for clinical purposes and how the treatment plan is

implemented through the various photon delivery techniques have been included in this chapter. Passive and active scanning techniques for delivering charged particles produced from particle accelerator have been discussed with a final overlook on the modern offline and online imaging techniques such as PET imaging, prompt gamma online imaging and proton vertex imaging used for verifying particle range and dose distribution in the course of radiation dose delivery.

In **Chapter 4**, an introduction to Monte Carlo Simulation packages designed for High Energy Physics (HEP) and medical physics studies have been reviewed with much emphasis on Fluka as a tool kit used in this project. The detailed input file format by cards and output files have been outlined and how user defined input variables incase the user is required to modify the programming code depending on the complexity of the desired problem, can be passed on to the Fluka programming code using accessible user routine files.

Chapter 5 presents both Monte Carlo simulation methodology and results. The set-ups of performed Fluka simulations using 160 MeV proton beams and 300 MeV/u carbon ion beams are well elaborated in details with description of the simulation procedures and obtained results about secondary radiation, their physical characteristics such as angular distribution and their energy spectra.

Chapter 6 presents the imaging detectors simulated for use in detecting secondary photons produced during hadron therapy. These cameras include high purity germanium block Compton camera and single scattering Compton camera. This Chapter also reveals the energy resolution, spatial and angular resolution of each camera and to what figures can these resolution parameters be set for better performance of each camera.

Chapter 7 concludes this project work by a brief discussion of results obtained in the due course of this study and a general conclusion finalizes the project.

2 Radiation Physics

In this chapter, we review the general basic principles of physics that are applied in radioactivity of unstable nuclei to form stable isotopes, how charged particles with mass interact with matter and how massless and charge-free photons like gamma and x-rays mainly interact with matter propagated through. The need of charged particles for clinical use calls for their generation for medical based work and this is discussed under particle accelerators currently in use today. The last sections review measurement of energy deposition in matter and how living human tissue interacts with radiation on the cellular level to cause variations in cell development.

Spontaneous disintegration of unstable radio-nuclides into stable daughter nuclides is known as radioactivity discovered by Henri Becquerel in 1896 and measured in the units of Activity called Curie, named after Marie and Pierre Curie the discoverers of Radium and Polonium in 1898. One curie, abbreviated as Ci, is equal to 3.7 x 10^{10} disintegrations or counts per second.

Since the process of radioactive decay is random for individual atoms, the probability of the decay during a given time frame (t) can be measured basing on a proportionality quantity called decay constant between the number of atoms to decay (dN) and amount of radioactive atoms available (N). The number of atoms that remain after a given period of decaying time is related with an exponential decrease to the number of the original number of atoms before the start of the decay process predicted in what is called the Radioactive Decay Law

$$N(t) = N_0 e^{-\lambda t} \tag{1}$$

And the time taken for the radioactive atoms to decay half their original amount is related to the decay constant by the equation 2, where this time is known as Half-Life, $T_{\frac{1}{2}}$ of the radionuclide:

$$T_{\frac{1}{2}} = \frac{In2}{\lambda} \tag{2}$$

From equation (1), the Activity A(t), defined by the number of disintegration per second at any time can be expressed in relation to the original Activity of the decaying nuclide, a similar exponential decay relationship as in equation (1)

$$A(t) = A_0 e^{-\lambda t} \tag{3}$$

For $A_0 = N_0\lambda$ and from equation 3, it shows that activity of a given radionuclide decreases exponentially with time.

2.0.1 Types of radioactive decay

In general, unstable radionuclides can decay by emissions of particles such as alpha particles, beta particles and when the produced nuclide called the daughter nuclide has not lost all its excess energy during the decay, it remains in an excited state called metastable state for a while then finally decays to ground state by emission of discrete energy photons.
through the barrier for the decay to occur.

The spontaneous change of charge in decay is referred to as beta (β)decay. This can happen through $\beta-$decay, $\beta+$decay or by Electron Caputre. Due to excess neutrons in the nucleus of an atom, a neutron converts into a proton through a weak interteraction by emission of an electron and an electron-antineutrino producing a daughter nuclide of increased atomic number by 1 and of same mass number as the initial nuclide. The energy of this decay called $\beta-$decay and momentum, are randomly shared by both electron and an electron-antineutrino producing a beta spectrum with a broad energy distribution between zero and the maximum energy or Q-energy of the decay, however the energy distribution would be discrete but rather continuous, figure 2.1, because of the excess energy carried on by the electron-antineutrino. The beta decay Half-life is seen to be inversely proportional to the fifth of the Q-Energy value of the decay and the average beta energy is about $\frac{1}{3}$ of the maximum energy or Q-Energy.

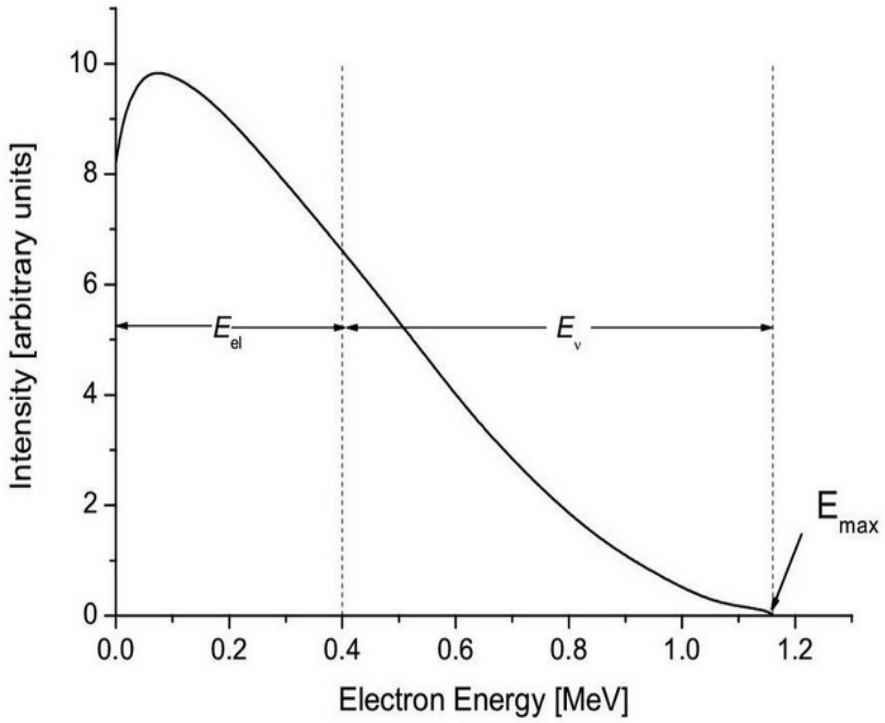

Figure 2.1 Beta decay spectrum showing a continuous energy distribution due to electron and ν_e sharing both energy and momentum [9]. From this diagram representation, an electron posses 0.4 MeV and its correspondent anti-neutrino posses the remainder 0.76 MeV since maximum energy is taken to be 1.2 MeV.

This energy distribution is also true for $\beta+$decay in which a proton changes to a neutron causing a nuclide to spit out an antimatter electron called a positron forming a daughter nuclide of reduced atomic number by 1 but with the same mass number as a parent radionuclide, and a positron neutrino is given off. The discrete energy values observed at the top of the continuous distribution in Beta decay experiments are a result of the daughter nuclides produced in the beta decay being in a metastable state, still excited that on de-exciting into their ground state in a process called Internal Transition, they emit discrete gamma photons of energy equal to the energy difference between the two energy levels. The gamma rays may

be emitted out of the atomic nucleus or absorbed by an inner most atomic electron and it is the electron ejected out of the atomic structure. Such electrons are called Auger Electrons and they proceed to interact with surrounding matter.

For unstable atoms having excess number of protons, a proton may combine with an inner most electron from the orbital K-shell in a process called Electron Capture producing a neutron in the nucleus of the atom with a consequence of less atomic number by 1 but with unchanged mass number. Excess energy is given off as a neutrino however a gap created in the lower energy level of the atomic structure is filled successively by electrons in upper energy levels, producing X-ray photons with discrete and characteristic energy distribution. This characteristic x-ray radiation was first detected by Alverez in 1938 and the Electron Capture process is always in completion with β+decay to occur though β+decay is most dominant.

2.0.2 Interaction of charged particles with matter

Charged particles like protons and carbon Ions propagate through matter by interacting with its constituents atoms by inelastic collisions with atomic electrons. Incident charged particles lose energy to orbital electrons thus excitation and ionisation which can lead to formation of delta rays. In addition elastic collisions or coloumbic scattering of the charged particles with atomic nuclei leads to broadening of the incident particle beam at low primary particle energies. Inelastic collisions with atomic nuclei leads to formation of daughter nuclides which can be just excited or short-lived positron emitting isotopes like ^{13}N, ^{11}C and ^{15}O. These are used in medical imaging specifically in Nuclear Medicine for studying dose distribution with aid of PET scanners through detecting the position of electron-positron annihilation in Human body tissue during hadron therapy.

When a charged particle is traversing through matter, it loses its kinetic energy through excitation and ionization to atomic electrons and the mean rate in loss of energy for charged particles per unit length $-\frac{dE}{dx}$ travelled is described by Bethe Bloch formula (4) which shows that at low momentum of a moving charged particle whose mass is greater than that of electron mass, the energy loss per unit length is dependent on the particle velocity (β), density of the medium and Energy (E) of the charged particle for non relativistic cases.

$$\left\langle -\frac{dE}{dx} \right\rangle = 2\pi N_a r_e^2 m_e c^2 \rho \frac{Z z^2}{A\beta^2} \left[In \left(\frac{2m_e \gamma^2 v^2 E_{max}}{I^2} - 2\beta^2 - \delta - 2\frac{C}{Z} \right) \right] \tag{4}$$

where
N_a is Avogadro's number, 6.022 x 10^{23}mol^{-1}
m_e is mass of an electron at rest, 511 MeV/c^2
r_e is radius of an electron, 2.817 x 10^{13}cm
c is the speed of light, 3.0 x 10^8m/s
ρ is density of the medium through which the charged particle traverses
Z is atomic number of material medium.
A is mass number of material medium.
z is charge of incident particle

$\beta = \frac{v}{c}$ velocity of charged particle
E_{max} is maximum energy transferred to an electron in a single collision
$\gamma = \frac{1}{\sqrt{1-\beta^2}}$ is relativistic term as a result of high particle velocity
I is the average Ionization energy of an electron
δ is the Density correction
C is the shell correction

With increase in particle momentum, energy loss reaches its lowest value corresponding to particles called Minimum Ionization Particle (MIPs) that undergo minimal energy loss and further velocity increase leads the particle into relativistic cases in which the energy loss increases slightly because the electric field around the charged particle flattens and extends its fluence at larger distances from its trajectory but later a Fermi's plateau, figure 2.2, is seen in energy loss rise due to the consequence of electron screening from distant atoms caused by Density effects and Polarisation of the medium as shown in the Bethe Bloch formula above.

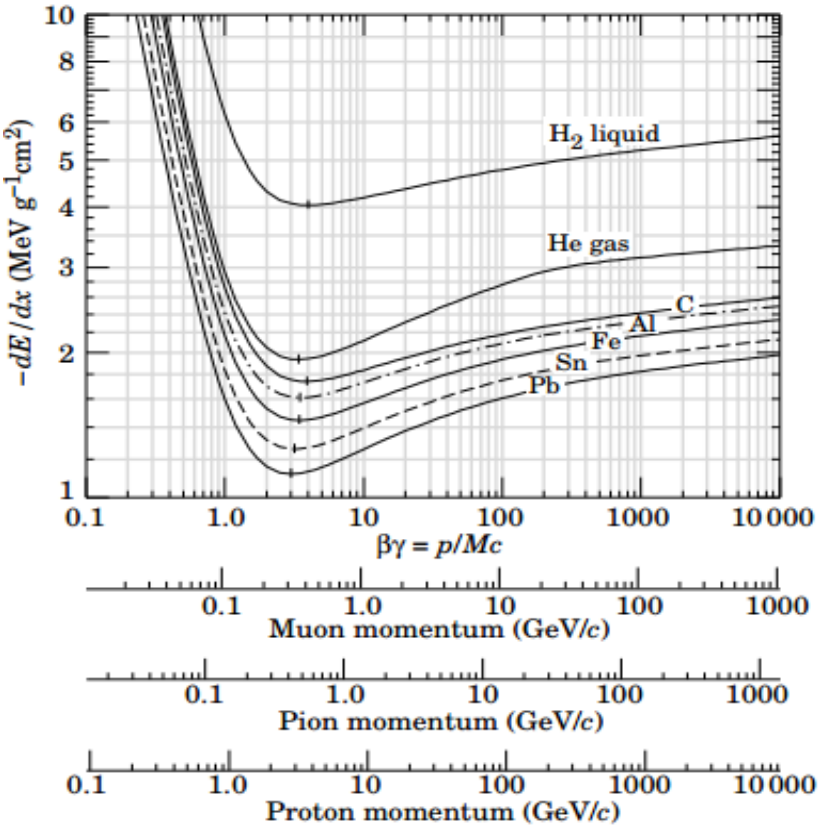

Figure 2.2: Energy loss variation with charged particle momentum extracted from [10]

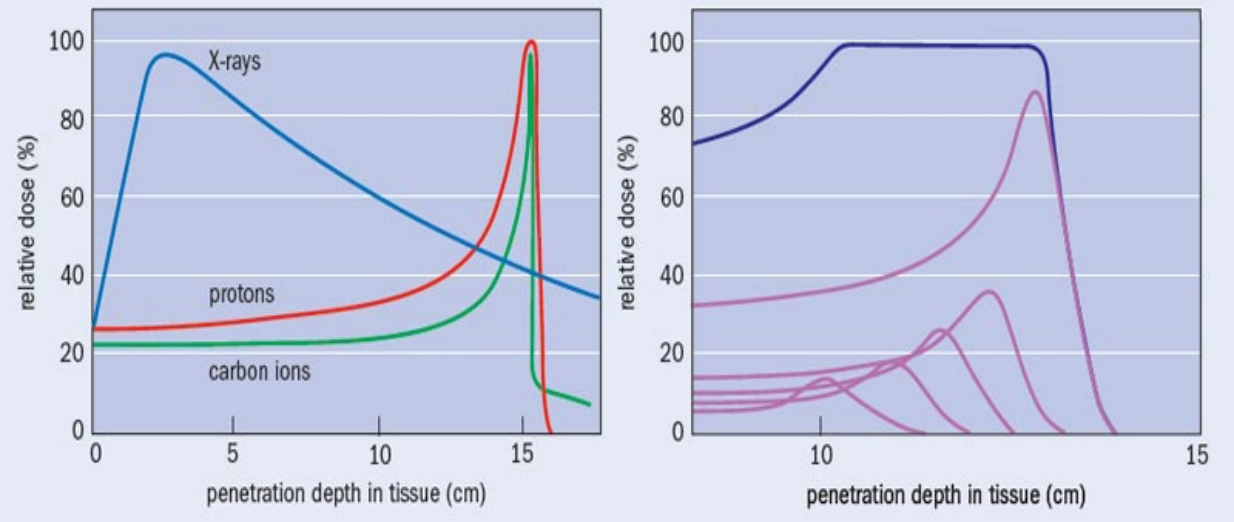

Figure 2.3: Dose-Depth curve extracted from [11] and shows relative Dose deposition using a 150 MeV proton beam, 18MV gamma photons and 250 MeV/u carbon ion beams. Increase in beam energy increases its penetration depth and highly charged carbon ions have less energy straggling in the peak region. To the right, successive decrease of incident beam energy creates a flattened Bragg peak called a Spread Out Bragg Peak (SOBP) which is targeted to cover the tumour volume.

From the Bethe Bloch formula, the stopping power is dependent on the velocity, density of the material traversed, and the charge of the charged particle indicating that the particle deposits a lot of energy to atomic electrons as it slows down and loses even more energy when it has a higher charge like carbon ions compared to protons. This gives rise to a sharp peak of energy loss with a narrow width called the Bragg peak, figure 2.3 with respect to the particle range in the medium, however not all particles come to rest by losing energy at the same rate, this causes widening of the Bragg peak in a condition called Energy Straggling.

2.0.3 Interaction of photons with matter

Electromagnetic photons such as gamma rays and x-rays interact with matter through which they propagate in a variety of ways depending on their energy and the nature of the matter traversed. Three main interaction mechanisms occur and these include: Photoelectric Effect, Compton Scattering and Pair Production as they will be discussed in turn, however it is noted that unlike charged particles that lose energy when they interact with matter, photons never lose energy on matter interaction but rather have decrements in their initial Intensity, **I**. This is called Intensity Attenuation when photons penetrate matter of thickness,x as illustrated by the equation (5):

$$I(x) = I_o e^{-\mu x} \tag{5}$$

where I_o is initial photon intensity.
$I(x)$ measured photon intensity after interaction with matter of thickness, x
μ is the material linear attenuation coefficient which is a function dependent on the total cross section(σ_{tot}) for Photoelectric Effect (σ_{PE}), Compton Scattering or Compton Effect (σ_{CE}) and Pair Production (σ_{PP}).

2.0.4 Photoelectric effect

This occurs when an incident photons of relatively low energy (E_γ) but more than the electron-Ionization energy or Binding Energy (E_B) interacts with an inner most orbital electron that all the photon energy is absorbed by the electron and it is emitted out of the atom or just excited, carrying with it all the transferred energy and momentum since the photo-electron is much lighter than the entire atom. The kinetic energy carried away by the photo-electron ($E_{e,KIN}$) is given by;

$$E_{e,KIN} = E_\gamma - E_B \tag{6}$$

The cross section, measured in Barns, for photoelectric effect decreases with increasing energy of the incident photon,figure 8, meaning that more energetic photons are most likely to penetrate through matter without photo-absorption than low energy photons and for fixed energies, the cross section is proportional to the fifth power of the Atomic number of the atoms in which the photon is interacting and inversely dependent of the energy of the photon. Cross section for Photoelectric Effect in Cadmium Telluride is higher than that in Silicon since Cadmium Telluride has a higher Z-value than Silicon for a particular Photon energy. The relationship is shown in Equation 8 below;

$$\sigma_{PE} \sim \frac{Z^5}{(h\nu)^{\frac{7}{2}}} \tag{7}$$

The general decrease of the Photoelectric effect cross section with increasing photon energy is interrupted by Absorption edges seen at K, L, M and N energy shell levels. These arise as a result of the incoming photon having energy equal or slightly greater than the corresponding atomic shell energy levels [12] that it can eject an electron from one of these energy levels. The K shell corresponds to higher photon energies followed by L, M and finally with N as photon energies drop, figure 2.4.

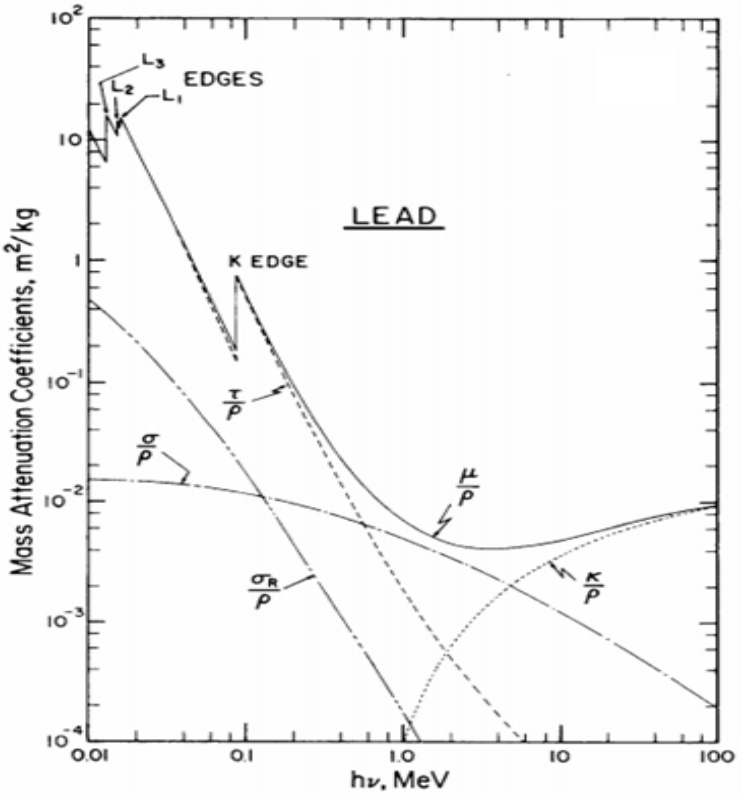

Figure 2.4: Mass attenuation coefficient variation with photon energy for Photoelectric effect in Lead, extracted from [13].

2.0.5 Compton effect

Compton scattering occurs when an incident photon of energy (E_0), interacts with an outer most assumed to-be stationary orbital electron, transferring some of its energy to the electron that it recoils with energy ($E_{e,KIN}$) through an angle, ϕ, and the photon is scattered through an angel, θ, with energy (E^1_γ). However some small amount of incident photon energy is transferred to the atom equalling or greater than the binding energy of an electron to cause ionisation. From conservation of momentum and Energy, the scattered photons deviates from its path by the energy value of:

$$E^1_\gamma = \frac{E_0}{1 + \varepsilon(1 - cos\theta)} \tag{8}$$

where $\varepsilon = \frac{E_0}{m_e c^2}$ is the reduced energy, a ratio of Photon energy to rest-energy of the scattering electron. In the case of maximum energy transfer in which the photon is back scattered in its incident path, the expression of scattered photon energy reduces to $E^1_\gamma = \frac{E_0}{1+2\varepsilon}$ for $\theta = 180^0$. This shows that the photon scattered energy E^1_γ is always less than the initial photon energy before Compton scattering event and as a must, from energy-conservation, energy must be transferred to the recoiling electron given by;

$$E_{e,KIN} = \frac{\varepsilon(1 - cos\theta)E_0}{1 + \varepsilon(1 - cos\theta)} \tag{9}$$

When there is a head-on collision of the photon with the electron such that electron travels forward with maximum Kinetic energy, the energy supplied to the electron gives rise to the Compton edge, clearly showing that the recoiling electron can not absorb all the energy of the incident photon, otherwise it would be photoelectric effect. The Compton edge formula is given by the equation :

$$E_{e,KIN} = \frac{2\varepsilon E_0}{1 + 2\varepsilon} \tag{10}$$

The process of Compton scattering can be put to full utilization in photon imaging by use of Compton cameras in which Compton scattering processes are optimised in the scattering detector of the camera. The cross-section or mass attenuation coefficient (ν_m/m^2Kg^{-1}) for Compton effect increases with decreasing Atomic number, a precaution for Silicon (Z=14) preference over germanium material (Z=32) when choosing a scatterer detector for the Compton camera and the cross section is roughly constant at low gamma energies less than 1 MeV, however after 1 MeV it gradually falls off as the photon energy increases to 100 MeV. This relationship between Compton cross section and photon energy is shown by variation of $\frac{\sigma}{\rho}$ in figure **??** above.

The probability that the incident gamma photon is Compton scattered into a unit solid angle assuming an unbound electron from its nucleus was, in details, studied by Klein and Nishina in their equation, Klein-Nishina formula (Equation 11) which shows the differential cross-section for different photon incident energies in polar coordinates shown in figure 2.5. From this figure, photons of fairly low energy have a high cross section of undergoing through a large Compton scatter angle thus not forward scattered like those with sufficiently high incident energy. Assumption of having the recoiling electron initially at rest is taken into account however much in reality, the electron has momentum around the orbit of its nucleus and at low incident photon energy, this causes a great contribution to Doppler broadening affecting the angular distribution of the Compton angle.

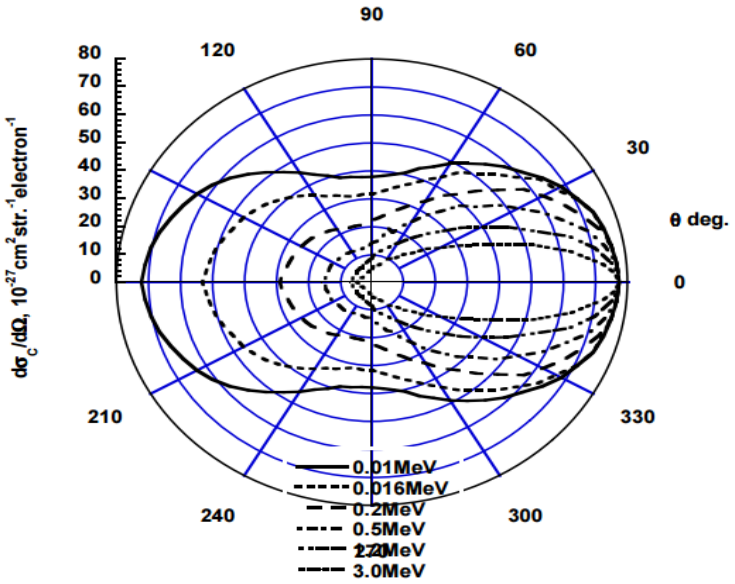

Figure 2.5: Klein-Nishina cross-section as a function of the Compton scatter angle for different energies. High energetic photons in MeV energy range are scattered through narrow Compton angles in the forward direction as compared to keV photons scattered through wide Compton scattering angles. This plot has been extracted from [14].

$$\frac{d\sigma_e(E_o,\Omega)}{d\Omega} = r_o^2 \left(\frac{1+cos^2\vartheta}{2}\right)\left[\frac{1}{1+\alpha(1-cos\vartheta)}\right]^2\left[1+\frac{\alpha^2(1-cos\vartheta)^2}{[1+\alpha(1-cos\vartheta)](1+cos^2\vartheta)}\right] \tag{11}$$

where $\alpha = \frac{E_0}{m_e c^2}$ and r_0 is the classical electron radius given by $r_0 = \frac{e^2}{4\pi\varepsilon_o m_e c^2}$ where e is the elementary charge. This formula has been extracted from [15].

2.0.6 Pair production

When a photon of sufficient energy of approximately 1.02 MeV and above interacts with matter, the photon is converted into an electron and a positron near a nucleus of an atom. This is because of the strong electric field of the positively charged atomic nucleus felt by the incident photon and as a result of energy and momentum conservation, the nucleus recoils in a short distance since it is massive. The least energy required for production of electron and positron in pair creation is 1.02 MeV since the rest energy of each electron and anti-electron is 0.511 MeV. The produced electron and anti-matter positron energetic in motion further interact within the medium in a way that electrons may undergo multiple scattering and bremstralung formation as well as positrons annihilating with freely abundant electrons in the medium to produce back to back 0.511 MeV photons detected as photons out of the medium for PET nuclear medicine imaging.

However when the pair production becomes possible, it becomes a dominant interaction process for photons of higher energy. The cross section for Pair production increases with raising photon energy above 1.02 MeV and varies by the squares of the Atomic number of the medium through which the photons are traversing. This is illustrated in equation 12 and

the variation of the mass attenuation coefficient an equivalent to its cross section is shown in figure 2.5 having Pair production cross section $\frac{\kappa}{\rho}$ increasing after 1.02 MeV:

2.0.7 Interaction of neutrons with matter

When a 160 MeV proton or a 300 MeV/u Carbon ion beam is projected into a soft tissue phantom as the study is in this project, the charged particle beam interacts with the phantom and as a result of nuclear interactions with nuclei, neutrons are produced within the phantom. These interact with the medium depending on their energies, for neutrons with energies above 100 keV interact with medium through elastic and inelastic scattering in which they lose a few eV to atomic nuclei as they undergo multiple scattering [16]. With many scattering events, they lose energy to less than 0.1 eV that they are slowed down to undergo a capture process in which they are absorbed by atomic nuclei forming excited daughter nuclides that decay by emission of gamma photons. The mass attenuation coefficient for capture process is inversely proportional to the neutron velocity.

For prompt gamma simulations, an energy threshold of 1 MeV can be implemented in the simulation set-up so as to eliminate the noise from neutron induced gammas with energies less than 1 MeV from the desired prompt gammas [17]. In simulations in which such neutrons are included, thermal neutrons are absorbed within the phantom and they never reach the outside detectors but fast neutrons penetrate through the phantom and reach out to the imaging detector.

2.1 Charged particle accelerators

Unlike x-ray photons that are produced when accelerated electrons emitted from the cathode plates in a Linear Accelerator (LINAC) hit a metal target, protons and carbon ions are accelerated mainly by two cyclic charged particle accelerators called Cyclotron and Synchrotron. Both accelerators have an application of magnetic field to the revolving charged particle beam however their design and physical application of magnets differ as described in the preceding sections.

2.1.1 Cyclotron

As a spiral charged particle accelerator first built by Ernest Orlando Lawrence with his graduate students at University of California in 1929, a cyclotron consists of two hollow D-shaped electrodes (Dees) held in a vacuum in which a magnetic field from two opposite poles of electromagnets made up from low carbon-steel, is experienced. The Dees, as showed in figure 2.6, are connected to a high frequency AC voltage which keeps changing the polarity of the Dees in the time period of half the Period (T) of revolution of the charged particle.

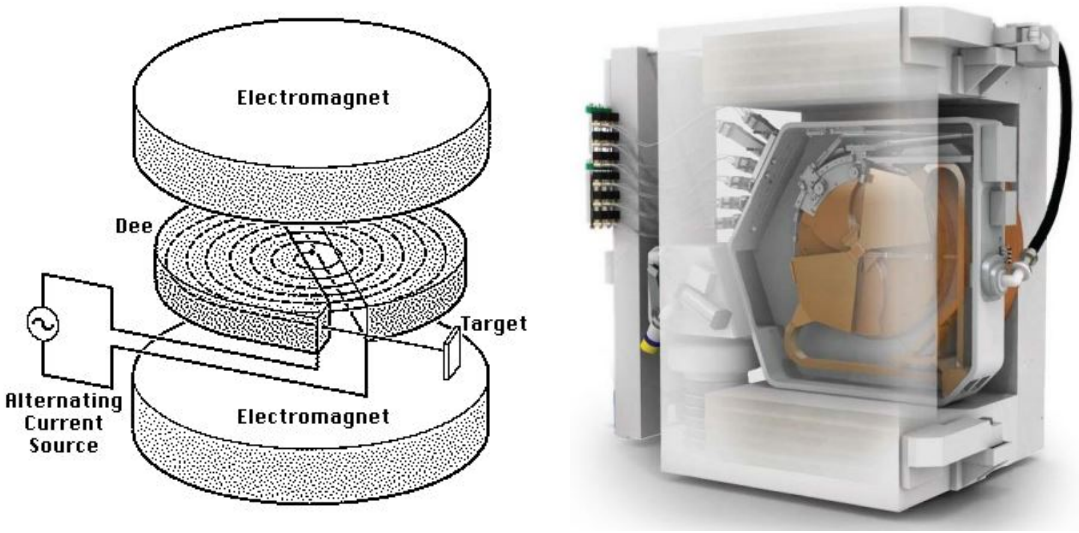

Figure 2.6: Schematic diagram of a cyclotron and a PETtrace 800 cyclotron based on a 16.5 MeV proton accelerator with an 8.4 MeV deuteron option at Uppsala, Sweden [18].

The ion source at the center between two electrodes produces the charged particles which are accelerated into one of the Dees by an electrostatic attraction and transverse in a spiral path inside the electrode due to the magnetic field perpendicular to their propagation path and velocity and when there is a change of electrode polarity, the charged particle accelerates into the opposite electrode with an increase in path radius, velocity, momentum and energy. This spiral motion due to the strong electromagnetic field continues until their escape from the electrode with a sufficiently high kinetic energy of 200 MeV. However, the energy and momentum gained by the charged particles is limited by the strength and size of the magnets.

The period, velocity and frequency of the accelerated particle can be obtained by equating the two electromagnetic forces, Lorentz force and centripetal force that act on the orbiting particle perpendicularly to obtain;

$$qvB = \frac{mv^2}{r} \tag{12}$$

The velocity of the charged particle can be expressed as $v = \frac{qBr}{m}$ and it is related to its angular velocity,w by v=wr and angular velocity to frequency by $\omega = 2\pi f$. And on simplification yields the expression for the Resonant frequency or Cyclotron Frequency as

$$f_o = \frac{qB}{2\pi m} \tag{13}$$

The condition for resonance under the implementation of a cyclotron is that the applied voltage across the Dees should be equal to the cyclotron frequency with an oscillation period of

$$\mathbf{T} = \frac{2\pi m}{qB} \tag{14}$$

showing that the time take for the particle to make a complete revolution in the two electrodes of radius r, is independent of the particle speed, v. The charged particle emerges out ot the

electrodes with a maximum kinetic energy of

$$\mathbf{E}_{KIN} = \frac{q^2 B^2 r^2}{2m} \tag{15}$$

The cyclotron can be used for both production of charged particle beams for production of radionuclides like 18-Flourine, 13-Nitrogen , 11-Carbon, 15-Oxygen, 123-Iodine, 201-Thallium and 38-Potassium used in Nuclear medicine and PET medical imaging for investigation of cellular glucose uptake like the use of 18-Flourine as FluoroDeoxyGlucose (FDG) by bombarding the accelerated particle to a chosen target as illustrated in table 1, and for production of the charged particle beam like protons of 1x10^9 primaries for cancer radiotherapy since particles of sufficient energy of 230 MeV can penetrate deep into human body by approximately 32 cm depth [19].

Radionuclide	Reaction	Decay	Energy (MeV)
^{11}C	^{14}N(p,α)	β^+	11-17
^{13}N	^{16}O(p,α)	β^+	19
^{15}O	^{15}N(p,n)	β^+	11
^{18}F	^{18}O(p,n)	β^+	11-17

Table 1: Summary of Cyclotron-Produced Isotopes by their mode of decay, reaction and energy. This table has been extracted from IAEA report about cyclotron produced radionuclides, principles and their practice [20]

To control the depth of the charged particle through matter since its penetration depth is proportional to its energy, an energy selection system consisting of a degrader (range shifter) of variable thickness, from 17-20cm, usually made of carbon wedge is used to interrupt the particle beam-line. However this always comes with a consequence of beam emittance, divergence and scattering when degrading from 230 MeV to 70 MeV which is controlled by using collimator slits usually made up of copper, brass, steel or lead. The collimated particle beam with varying energies that form the spread out Bragg peak (SOBP) is positioned to the target site (tumour) through bending, steering and focussing by the quadrupole magnets in a pencil-beam shape. Figure 2.7 shows the various types of range shifters which can be distinguished in discrete designs, made of a set of plates that are inserted into the beam line.

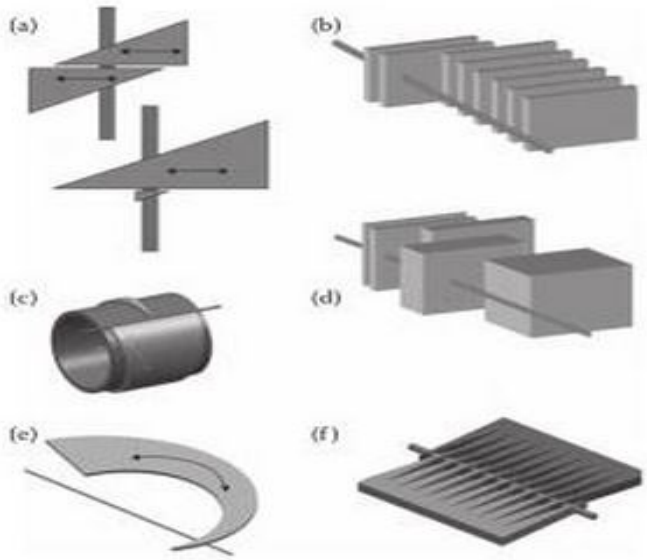

Figure 2.7. several design concepts of degraders [21].

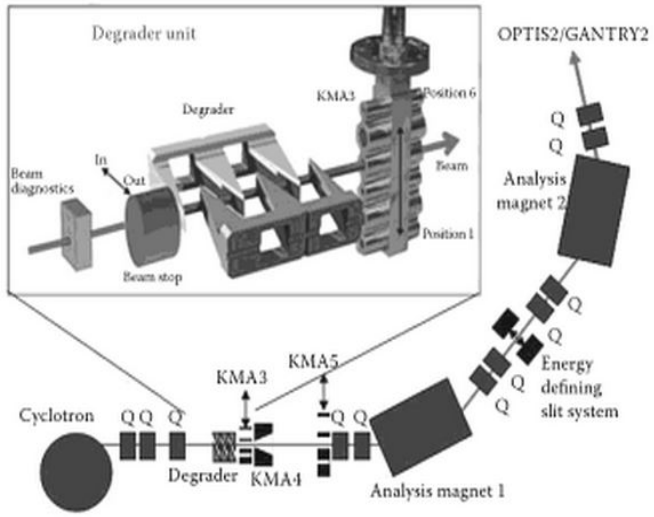

Figure 2.8. Schematic representation of the beamline. The above two figures 2.10 and 3 were extracted from [21].

Figure 2.7 shows a) a two versions of a system based on two or one adjustable wedges, b) Insertable slabs of graphite, c) Rolled-up wedge. d) Insert-able blocks with different thicknesses, e) Rotatable Plexiglass curved wedge, f) Adjustable multi-wedge Design. And Figure 2.8 shows a Schematic diagram of the beam-line, solid rectangles are quadrupole (Q) and dipole magnets. Location of collimators (KMA) and energy defining slit system are indicated.

2.1.2 Isochrous cyclotron

Cyclotrons had their evolution start from Uniform-Field Cyclotron in which the vertical magnetic field was uniform in both the vertical plane and the azimuth or radially direction of the machine. This was the very first cyclotron device used for Nuclear Physics research

however its limit of ion beam acceleration to energies of only about 15 to 20 Mev gave raise to Azimuthally Varying Field (AVF) cyclotron. This is also known as an isochrous Cyclotron for cyclic particle acceleration. Such cyclotrons have a characteristic increase in ion beam focussing as they are designed in a way that a constant magnetic field is applied perpendicular to a varied horizontal plane by introduction of Hills and Valleys. Beam particles passing through the Hill regions experience a more magnetic field force thus bending much more than when in the space-filled valley region because the magnitude of the vertical magnetic field is approximately inversely proportional to vertical gap width. proper choice of focussing elements in order for the magnetic variation to balance the relativistic mass increase results into a constant revolution frequency, a condition true for Isochronous cyclotron. Such a design as illustrated in figure 2.9 increases the cyclotron efficiency when accelerating particles to higher energies in relativistic regimes and also gives provision for generation of high intensity particle beams.

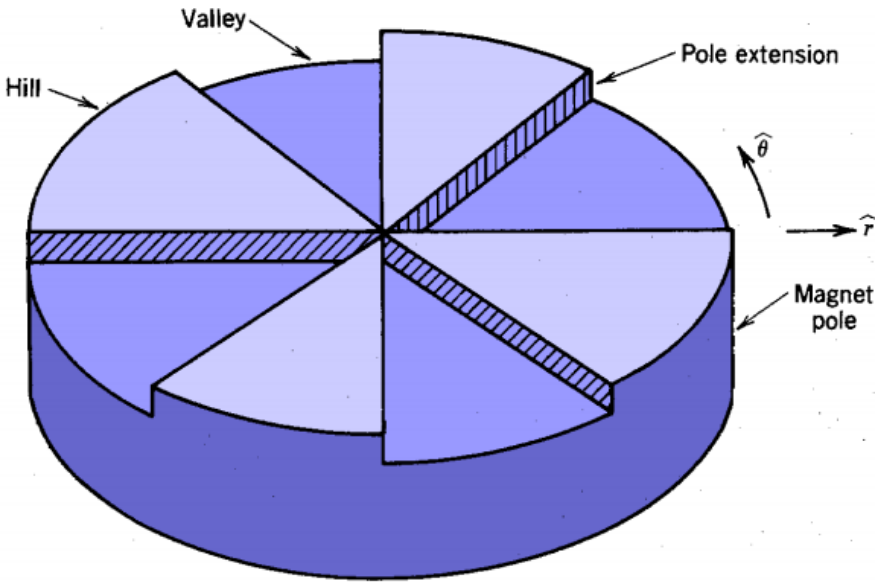

Figure 2.9: An azimuthally varying field cyclotron [22] showing the Hills and valley sectors for ion beam focussing. These cyclotrons have been upgraded to Separated-Sector Cyclotrons and Spiral Cyclotrons with a main target of increasing vertical confinement force for beam focussing.

2.1.3 Synchrocyclotron

A synchrocyclotron is an upgrade of the classical cyclotron particle accelerating device which accelerates charged particles in cyclic path with a constant Radio Frequency. However for Synchrocyclotron, charged particles are accelerated with a frequency of the driving Radio Frequency electric field applied at the Dee electrodes varied in order to compensate for increase in mass of the accelerated particles as their velocity begins to approach the speed of light in relativistic considerations. This upgrade has led to attainment of higher charged particle energies such as 200 MeV for deuterons, 400 MeV for alpha-particles and 1 GeV for protons. Currently, superconducting Synchrocyclotron have been built for proton therapy

since high magnetic fields are used to build compact systems which resolve the constraint of space in hospitals.

2.1.4 Synchrotron

Edwin McMillan first constructed an electron synchrotron in 1945, although Vladimir Veksler had already published the principle in a Soviet journal in 1944. The first proton synchrotron was designed by Sir Marcus Oliphant and built in 1952 and later in 1959, it was put to use. A synchrotron is basically made up of the Linear Accelerator (LINAC) as the particle injector, a cyclic evacuated ring made up of dipole magnets for bending the accelarating beam in a closed loop, quadruple magnets for beam focussing and sex-tupole magnets used for further focussing and steering of the beam by making corrections for the chromatic effect of a quadrupoles [23] and finally an extraction system which delivers the highly accelerated and energized pencil beam to treatment rooms or research Laboratories. In June-1994, carbon ion therapy begun at National Institute of Radiological science (NIRS) using the first Heavy-Ion Medical Accelerator in Chiba (HIMAC) that consists of an injector made up of a 10 GHz NIRS-ECR ion source for producing carbon ions or an 18GHz NIRS-HEC ion source for producing higher energy ions, an 800 keV/u RFQ Linac and a 6 MeV/u Alvarez linac used for initial linear acceleration of ions from the source. This is followed by the dual 800 MeV/u synchrotron rings and a beam delivery system to the three treatment rooms, figure 2.10.

Carbon ions produced by the 10 GHz NIRS-ECR ion sources are, through a Low Energy-Beam Transport line (LEBT) injected into the 800 keV/u RFQ and Alvarez Linac cascade, both operated at frequency of 100 MHz with diameter of drift tube of over 2m in order to accelerate the ion charged beam upto 6 MeV/u before being injected into the dual synchrotron rings via the charge stripper installed at the output end of the alvarez Linac to strip the C+4 into C+6 ions.

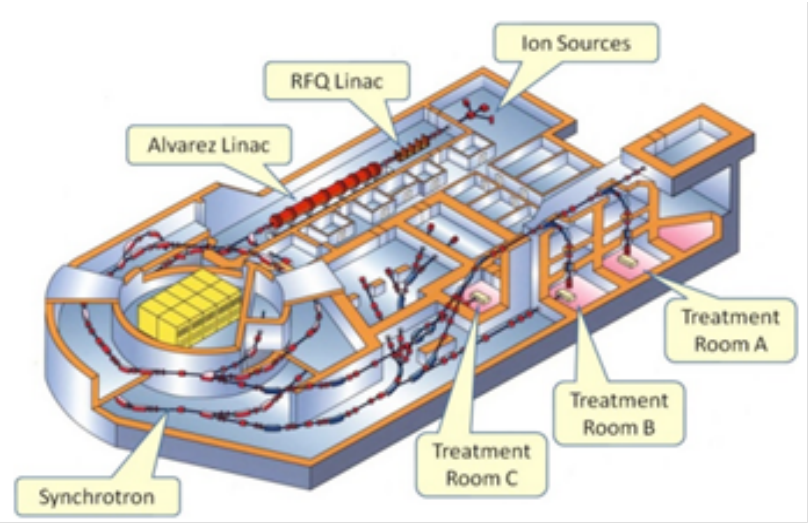

Figure 2.10: Eye bird view of HIMAC synchrotron facility at Chiba [24].

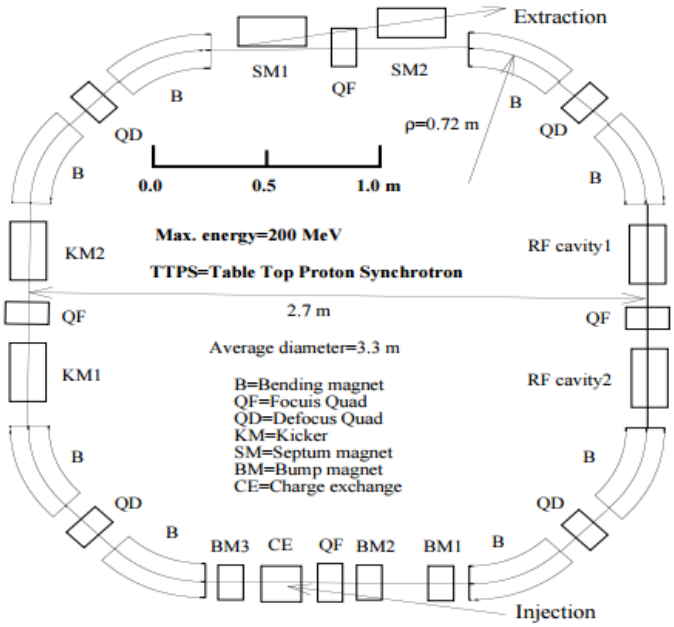

Figure 2.11. Layout of the synchrotron ring extracted from [25].

Modern medical based synchrotrons are designed to be compact in order to limit the amount of space needed for the equipment and this is done by optimizing its lattice without losing its performance using superconducting magnets [26]. The circumference of the synchrotron can be only 60m with a diameter of 12m and made up of a lattice structure consisting of 6 cells each with two dipole magnets at a bend angle of 30^o, as showed by figure 2.11.

The beam injected into the evacuated ring at a pressure of 10-11 Torr is accelerated to a maximum energy of 430 MeV for carbon ions, as it is bent by the magnetic field of strength 1.6 T produced by the dipole magnets and the beam rotating with Revolution frequency (RF) ranging from 1.06 to 3.07 MHz [27] before being either slowly or quickly extracted. For slow particle extraction performed by sextupoles through beam focusing and steering, a repetition rate for the beam should be 0.5 Hz and for fast particle extraction, it is 1 Hz. Extracted particle beam is delivered to the treatment room or research laboratory through the delivery system.

2.1.5 Electron Linear Accelerators (LINAC)

These have been used in clinical set-ups for cancer therapy with the first clinical linear accelerator installed in June 1952 at the Hammersmith Hospital, London, UK and the first patients treat with this technology on the 7^{th} of September 1953. They involve use of high frequency standing electromagnetic waves to accelerate high energy electrons through a vacuum to produce bremsstrahlung x-rays when they hit a high atomic number target such as Tungsten cooled by water. The absorbed electrons energy is converted into a bremsstrahlung spectrum of x rays with their maximum energy equal to the incident electron energy. The mean photon energy of the beam is approximately one third of the maximum energy.

For medical radiation therapy, linacs are designed basically in two ways to accommodate

both electron and x-rays operating modes depending on the linac manufacturer. For modern radiotherapy, high energy x-rays in the range 4-25 MV and electron energy range 6-22 MeV are used to treat tumours depending on the tumour depth, site and treatment plan required for maximum dose delivery to cancer cells, for example the Varian Clinac 18 unit produces electron beams with maximum electron energy of 18 MeV and x-rays of energy 10 MV [28].

In the electron therapy mode, a narrow electron pencil beam of about 3 mm in diameter is directed to hit a lead scattering foil instead of a metal target. The scattering foil is made of a thickness that enhances scattering of most of the incident electrons with a smaller fraction of the electrons converted into bremsstrahlung. Scattering of the electrons produces uniform electron fluence across the treatment field and the dose rate of the electron beam is monitored by an ionization chamber. Spread out electrons are passed through secondary collimators and an accessory mount to shape them according to the shape of the tumour, figure 2.12. This kind of linac mode which produces electrons in the energy range 6-22 MeV is used to treat superficial tumors since electrons penetrate less into body tissue less than 5 cm deep. Such application is suitable for cancer therapy of the lips, neck, head and skin cancers.

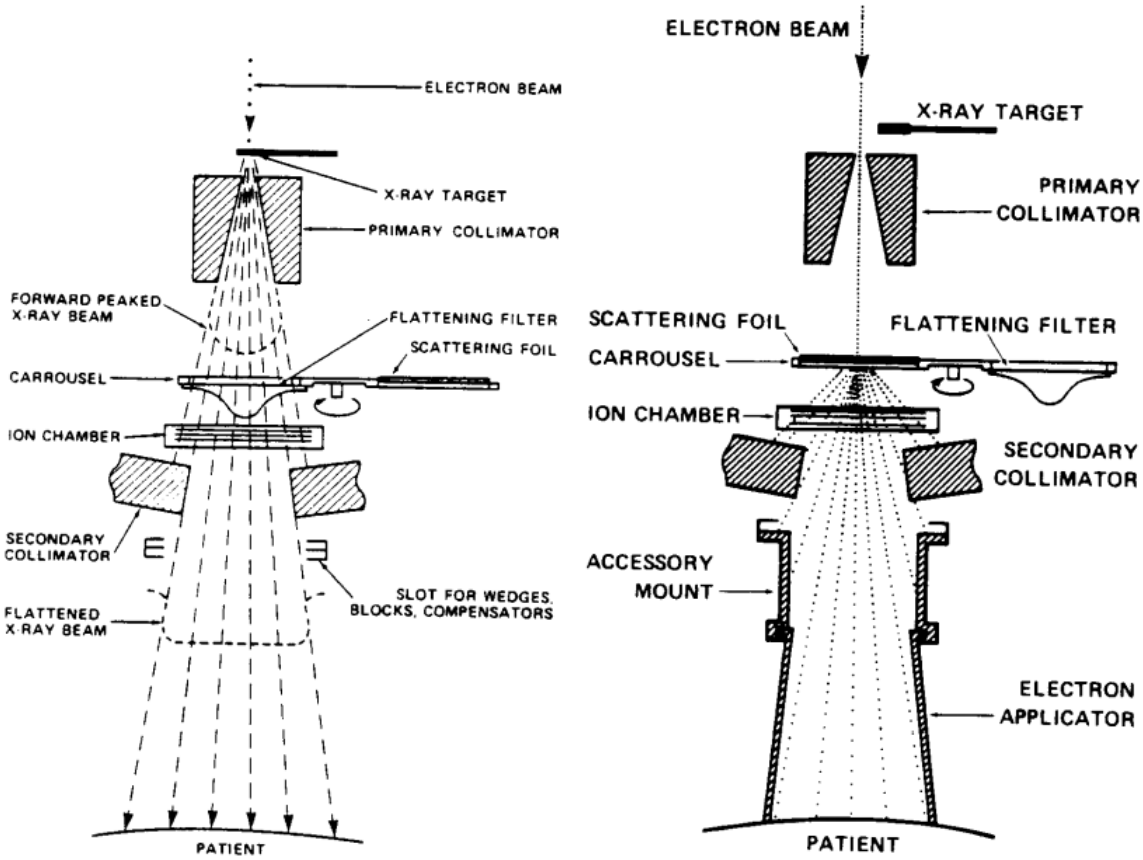

Figure 2.12: Components of treatment head LINAC. **To the Left**: X-ray therapy mode. **To the right**: Electron therapy mode. Extracted from Karzmark Cj. Morton RJ. Aprimer on theory and operation of LINAC in Radiation therapy. U.S Department of Health and Human Services, Bureau of Radiological Health, 1981 [29].

In the x-ray mode, the produced x-rays after the pencil electron beam hits the target, have a non uniform intensity with high intensity in the mid-forward direction of the x-ray beam. A flattening filter usually made up of lead, tungesten, uranium steel or aluminium, is used to unify the x-rays beam by its intensity as it is passed through the ion chamber with a bias voltage in the range 300 to 1000 V connected across its electrodes with a purpose of monitoring dose rate, integrated dose and the field symmetry [28]. Later the beam is passed through secondary collimators either lead or tungsten made with opening range between 0 and 40 cm to shape and match the tumor size of interest so as to reduce the damage to other organs at risk surrounding the tumour, figure 3.2.

2.2 Radiation dosimetry - Fluence and Kerma

When radiation transverses matter, it interacts with it along its path through excitation and ionization when having sufficient energies to cause ion pairs and this can be measured in radiation quantities such as exposure, absorbed dose, dose equivalents and its related quantities. The number of charges or ions produced per unit mass in air by photons of energy less than 3 MeV is referred to as Exposure which was measured in roentgen equivalent to $1R = 2.58X10^{-4}C/Kg$as expressed in the current International System (SI) units of Coulomb per Kilogram. However exposure has been replaced in terms of radiation measurement with Dose or Absorbed Dose, the amount of energy deposited by ionizing radiation in a medium per unit mass measured in Gray (Gy) equivalent to 1 Gy = 100 rad, the old SI unit of dose as Rads equivalent to 1 rad = 100 ergs/g. Accounting for the radiation type, Dose Equivalent (H_T) is considered as the dose times the weighting factor;

$$H_T = \Sigma W_R D \tag{16}$$

where W_R takes into account the Relative Biological Effectiveness of the radiation type with photons and beta particles having a W_R value of 1.0 and alpha particles which are densely ionizing having W_R of 20 as they produce more ions pairs per radiation length traversed. Equivalent dose is measured in Sieverts with basic units similar to absorbed dose since W_R is a just numerical factor.

However, different body tissues like borne marrows and brain cells, Table 3, have different sensitivity to particular radiation types depending on the reproduction levels of the cells. Accounting for the different cell sensitivities, the Effective equivalent dose which is a measure of the cancer risk to the whole living organism is taken as a measurement of radiation energy deposited in cells. The effective dose is obtained by summing individual organ equivalent doses multiplied by the corresponding tissue weighting factors;

$$E = \Sigma W_T H_T \tag{17}$$

with $\Sigma W_T = 1$ where W_T are dimensionless tissue weighting factors characterizing the relative sensitivity of various body tissues. Eleven tissues and organs are listed in International Commission of Radiological Protection (ICRP) report 60 (Table 2) with individual weights w_T. A revised set of thirteen tissue weighting factors is defined in the ICRP 2006 Draft Recommendations [30] Table 3).

Table 2. Retrieved from ICRP recommendations for tissue weighting factors w_T published in 1991.

$Organ$	w_T	$\Sigma_T w_T$
$Gonads$	0.20	0.20
$Thyroid, Oesophagus, Bladder, Breast$	0.05	0.30
$Lung, Stomach, colon, bonemarrow$	0.12	0.48
$Bonesurface, Skin$	0.01	0.02

Table 3. Taken from ICRP recommendations for tissue weighting factors w_T drafted in 2006.

$Organ$	w_T	$\Sigma_T w_T$
$Lung, Stomach, colon, bonemarrow$	0.12	0.72
$Gonads$	0.08	0.08
$Thyroid, Oesophagus, Bladder, Liver$	0.04	0.16
$Bonesurface, Skin, Brain, Salivaryglands$	0.01	0.04

Fluence is one of the quantities used to describe mono-energetic radiation beams which can be either photons or charged particle beams. Beam description can be parameterized in terms of fluence as Particle fluence, energy fluence, particle fluence rate and energy fluence rate known as flux. Particle fluence is defined as the number of particles crossing a unit cross section area with a standard unit of m^{-2} and a consideration is taken that the particle direction is perpendicular to the area. Equation (18) shows particle fluence

$$\Phi = \frac{dN}{dA} \tag{18}$$

Where dN is the number of particles crossing an area of dA. For plane particle fluence, fluence is dependent of the particle incident angle while as for a spherical area, it is independent of the particle incident angle since all particles at any time are orthogonal to the sphere surface. The term energy fluence refers to the amount of radiant energy dE incident and crossing a unit area. This is shown in equation

$$\Psi = \frac{dE}{dA} \tag{19}$$

SI unit for energy fluence is J/m^2 and energy fluence can also be calculated from particle fluence using the equation below expressing it as a product of particle fluence and particle E.

$$\Psi = \frac{dN}{dA}E = \Phi E \tag{20}$$

However to describe polyenergitic beams, one needs to replace particle and energy fluence with particle fluence spectrum and energy fluence spectrum, defined by the equations (21) and (22) respectively

$$\Phi_E(E) = \frac{d\Phi}{dE}(E) \tag{21}$$

and

$$\Psi_E = \frac{d\Psi}{dE}(E) = \frac{d\Phi}{dE}(E)E \tag{22}$$

where $\Phi_E(E)$ and $\Psi_E(E)$ are particle fluence spectrum and energy fluence spectrum respectively. The increment of particle fluence in a time interval is referred to as particle fluence rate with units of $m^{-2}s^{-1}$and the energy fluence increase with time is called flux and this is also known as Intensity, the amount of power that flows in a unit area. The SI units of this quantity are either W/m^2 or Joules per meters squared per seconds squared.

Indirect ionizing radiation such as neutron and photons interact with matter by transferring the kinetic energy into production of charged particles for example, for gamma radiation produces electrons through processes like Compton effect, pair production and Compton scattering. The produced charged particles further transfer their energy in the traversed medium by ionization and atomic excitation. The average amount of energy transferred by such indirectly ionizing radiation to ionizing radiation per unit mass is referred to as Kerma (K), abbreviated from Kinetic Energy Released per unit Mass with the SI unit as J/Kg which is equivalent to 1 Gray.

$$K = \frac{dE_{tr}}{dm} \tag{23}$$

Specifically for charged or ionizing radiation such as electrons, the amount of energy lost by such a charged particle in collisions of medium mass m, except secondary electrons, is known as Cema [31]. It shares the same SI units as Absorbed dose or kerma as one Joule per Kilogram or Gray.

2.3 Radiation biology

Radiation interacts with human living cells of size-range 10-100μm and specifically atoms that are constituents of the cells through inelastic collisions leading to excitation and ionization of the cell atoms but in most cases, ionization which occurs in a time frame of 10^{-10} to 10^{-16}s, dominates depending on the type and energy of the radiation to which living tissue is exposed. Heavy and charged particles like proton, alpha particles and carbon ions are more ionizing than mass-less charge-free photons.

Living cells in the human body are made up of about 60% water and the nucleus consisting of the Deoxyribonucleic Acid (DNA), a molecule in the cell nucleus that contains the genetic instructions for the development and function of living things. Ionizing radiation may interact with the atoms of the DNA by ionizing them directly through breaking the DNA strands and such an interaction, if sufficient chromosomes in the DNA are not able to replicate properly, leads to a cell being terminated from survival. This is the Direct effect of radiation on cells however, the probability of ionizing radiation to interact directly with DNA atoms is small since DNA is a small portion of the cell with most of the cell filled with water. Radiation rather interacts with water molecules by breaking the covalent bonds between Hydrogen and Oxygen atoms to produce ions. In the cell, these ions recombine to form compounds like water which is neutral and free radicals that form oxidizing agents such as Hydrogen Peroxide. Such a low PH oxide instead attacks the DNA and causes damage to it, a term known by Indirect Effect of Radiation to living cells

Cells are considered to be damaged when their strands are broken by radiation however, the body through DNA-repair enzymes is able to repair the broken strands. If the strands are correctly repaired as the initial DNA configuration, the cell recovers from radiation exposure damages and undergoes reproduction process as normal. However when strands are incorrectly repaired by the enzymes, this leads to a cell mutation and replication of such cells leads to development of cancer tumours. Scattered groups of mutated cells lead to metastatic condition in cancer patients.

Human exposure to radiation comes with consequences depending on the radiation type and dose absorbed by cells. Such exposures to ionizing radiation were first registered in 1895 with the discovery of x-ray radiation by Roentgen and the first human injury that led to induced cancer from radiation exposure was noted in 1902. Later in extended years of 1920's and 1930's, more cancer induced cases were reported from radiographers and miners who were exposed to radiation from radium industries, underground inhaled radioactivity in mines and other special occupation groups. However long-term biological effects as a result of smaller and repeated radiation doses were never noticed till after the second world war [32].

Detectable radiation effects are observed depending on how short or long the latent period is in regards to the radiation response by living cells. Depending on the dose and radiation type, cells may respond differently to radiation exposure and short term effects like infertility, radiation sickness and skin reddening in which cell response increases with exposure dose, but with a threshold dose below which no response or mortality is recorded, is called a Deterministic biological effect. Such an effect with a threshold aids in establishing acceptable levels of exposure to radiation in order to limit its damage.

However, the deterministic effects of radiation response exposure do not take into account the risk of small fraction of dose to living cells due to the threshold. The study of very small dose variation with the probability of occurrence of cell mutation gives rise to a linear relationship between the two parameters due to the tendency of cells repairing after small dose exposures and this has shown that increase in dose increases the risk of developing cells mutation with time since a long latent period to detect response is considered. This is the Stochastic effect of radiation on human tissues which can lead to delayed cancer incidences and hereditary defects.

3 Radiation therapy

In this chapter, the Physics of radiant energy such as massless photons and charged particles like electrons, protons and carbon ions has been reviewed with major aim for treatment of cancer cells. Amount of radiation energy deposited and absorbed per unit length has been linked to how much biological impact a particular radiation type can affect human cells during therapeutic procedures.

Also, production of both electrons and photons for clinical purposes using Medical linear accelerators has been reviewed and how the treatment plan is implemented through the various photon delivery techniques. For charged particles, passive and active scanning techniques for delivering charged particles produced from particle accelerator have been discussed with latter, a final overlook on the modern on and off-line imaging techniques such as PET imaging, prompt gamma on-line imaging and proton vertex imaging used for verifying particle range and dose distribution in the course of radiation dose delivery.

Radiation has been put to ultimate use of clinical practice as a tool to kill cancer cells since radiation can damage the cell DNA strands either through single strand or double strand DNA breakage. This practice with a golden aim of cancer treatment using radiation is referred to as radiation therapy, one of the three ways used is to treat cancer with surgery and chemotherapy being the other two methods. The other clinical use of radiation besides therapy is its diagnostic use in medicine called radiology in which radiation is used to image internal body organs of human body if anatomy structure is required for examination especially before therapeutic procedures. Radiation may be directed through the body externally like in CT or emitted from the sources inside the body tissue in modalities such as SPECT/PET that it is detected from the outside by radiation detectors such as Anger Camera.

Treatment using radiation can be done either internally where sources like iodine, cesium are encapsulated in small capsules and invasively implanted into the patient's body at the tumour site in the technique called brach therapy or externally where the radiation source for example Cobolt 60 source used in gamma knife is placed outside of the patient's body and the emitted gamma radiation is directed to the planning target volume within the patient. This is called teletherapy and usually for clinical procedures, gamma photon dose is delivered to patients in standard fractions of 2 Gy per fraction for weeks. However before any treatment planning and procedures are done, imaging of the required tumour is required to precisely locate its position and extent of growth. Today in clinical settings, this is done using standard imaging modalities such as Magnetic Resonance Imaging (MRI) and Positron Emission Tomography (PET) for investigating the metabolic mechanism and functioning of tumours and using Computed Tomography (CT) to diagnose the physical anatomy of tissue. But for more detailed acquisition, the modalities are combined into one such as PET-CT and PET-MRI.

Due to high dominance of Compton scattering over photoelectric effect during the use of high energy gamma radiation used for radiation therapy, medical technology has advanced

to the use of relatively low energy photons called x-ray photons produced clinically using medical linear accelerators with mega-voltage of 25 MV for cancer treatment. They come with a high cross section for pair production in the patient body, required to cause damage to human cells through production and formation of molecular radicals in cellular cytoplasm to damage cell DNA as a photon is a low Linear Energy Transfer (LET) radiation.

3.0.1 Linear energy transfer and Relative biological effectiveness

The amount of energy transferred by a given ionizing radiation and adsorbed by a material medium per unit length in which the radiation travels is referred to as Linear Energy Transfer (LET) measured in keV/μm which is usually positive however, different radiation types have different LET values such as therapeutic ^{60}C gamma photons have 0.2 keV/μm, 150 MeV protons have 0.5 keV/μm and 2.5 MeV alpha particles have LET value of 166 keV/μm [33]. This is attributed to the fact that LET is directly proportional to the square of charge and inversely proportional to the square of particle velocity, categorizing ionizing radiation into low LET radiation like photons and protons, medium LET and high LET radiation such as alpha particles and carbon ions. Fast moving charged protons have higher LET than photons.

Different LET radiations may be transferring the same amount of energy per unit mass, absorbed dose in Gy, to the same medium but rather never produce equal biological damage to the medium. The term relating the ability of such radiation types to produce an equal biological impact is referred to as Relative Biological Effectiveness (RBE), defined as the ratio in dose of a standard radiation type chosen as 250KV x-rays to the dose of any radiation under test consideration to produce the same biological effect in tissue, shown in equation (24)

$$RBE = \frac{D_{ref}}{D_{test}} \tag{24}$$

where
D_{ref} is the reference dose from 250KV x-rays and
D_{test} is the dose of the radiation under test to produce the same biological effect.

RBE is greatly dependant of the radiation dose, biological end point and LET of a particular radiation. Increase in LET increases RBE for a consideration in mammalian cells due to the fact that rise in LET causes more damage to the cells as more ionization of cellular atoms occurs leading to greater biological damage and the rise elevates to its maximum when 100KeV/μm is reached and beyond this point, a fall of RBE is evident as LET increases. This is referred to as over killing of the tumour target cell by densely ionizing radiation such as carbon ions. This is illustrated in figure 3.1

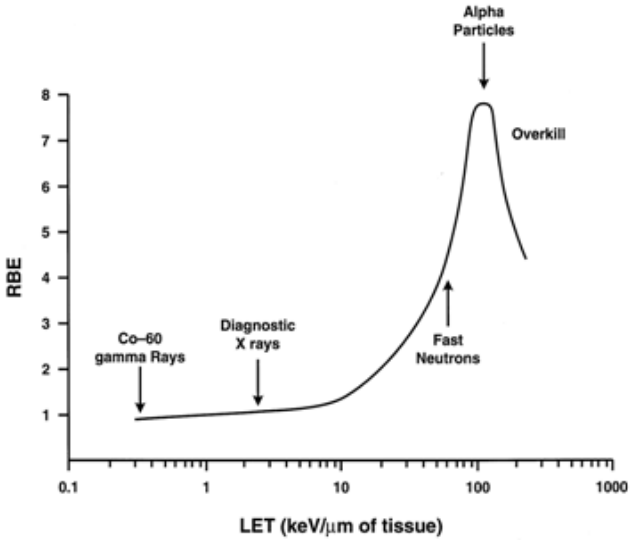

Figure 3.1: Relationship between RBE and LET for low LET radiation such as gamma rays and x-rays, and high LET radiation such as alpha particles [34].

For all clinical radiation therapeutical procedures done using photons, the RBE value used is 1 and for proton therapy is 1.1 regardless of the dose, fraction or position of radiation beam delivery. But for carbon ion therapy, high LET particles are used to deliver treatment dose with RBE from 3 to 5 times the values of both proton and photon therapy. This merits carbon ions as the best treatment radiation type for hypoxic radio-resistant tumours as the escalation in RBE values is at the maximum range of charged particles positioned to the tumour target volume.

3.1 Photon therapy delivery techniques

3.1.1 3D Conformal radiotherapy

A technique in which a photon or electron beam with uniform intensity is confined by the gantry tungsten collimators to match the shape of the tumor size for 3 dimension treatment. Before therapeutical procedures are done 3 Dimensional patient images are first obtained in the clinical setting using Positron Emission Tomography, Single Photon Emission Computed Tomography, Magnetic Resonance Imaging or PET-CT to obtain functional and anatomical tumor information so as to locate precisely the tumour volume of interest for proper treatment planning. This comes with a merit of escalating the dose to the tumour site and limiting the risk of morbidity to the surrounding health tissues, for example this technique has shown precisely high dose delivery and distribution to localized prostate cancer with reduced dose to bladder and rectum [35] during localized prostate cancer radiation.

3.1.2 Intensity Modulated Radiaotherapy (IMRT)

IMRT is another conformal radiation therapy technique that involves use of a photon beam conformed to a shape that fits the tumor volume, delivered in a number of angles with a varied intensity using beam fluence-modifying devices such as wedges, compensating filters

and MultiLeaf Collimators(MLC). However, modern IMRT treatment plans are generated using inverse planning systems which help by use of computer optimization techniques to determine distribution of intensities across the tumour volume with the capacity of generating concave dose distributions and providing specific sparing of sensitive normal structures.

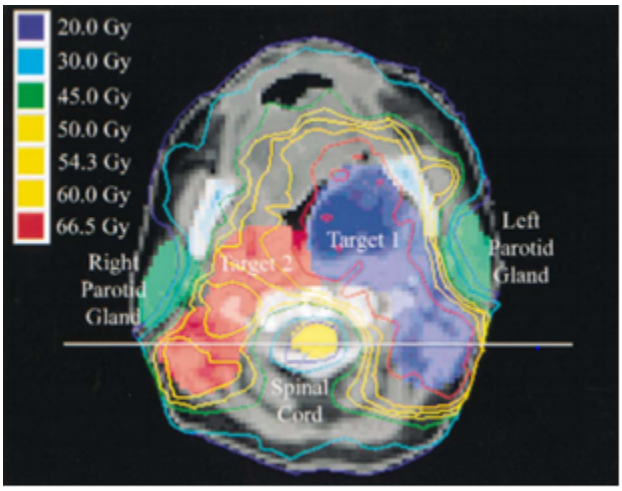

Figure 3.2 Transverse cross-section for a Typical head-and-neck IMRT treatment plan showing conformal avoidance of the spinal cord and parotid glands while simultaneously delivering multiple dose prescriptions (66.5 Gy and 54.3 Gy) to the two target volumes. White line corresponds to the position of the coronal cross-section. [36]

However to a less extent as a long time effect, IMRT has a downsized impact of development of second cancers and solid cancers to patients since it is delivered in multiple directions to cover the tumor volume, exposing larger volumes of normal tissues to small radiation doses. This is a high risk of second cancer in infants with still developing cells since such somatic cells are very sensitive to radiation and further an increment risk of solid cancer in the elderly [37].

3.1.3 Volumetric Modulated Arc Therapy (VMAT)

A step forward from intensity modulated radiation therapy in treatment delivery to patients, first described by Rock Mackie in 1993, is the Volumetric modulated arc therapy in which a single or more gantries are rotated round the patient through 360^0 to allow radiation dose delivered accurately and efficiently to planning target volume externally without intensity modulation of the radiation beam from the rotating gantry [38]. This has increased dose confinement to the target volume reducing greatly toxicity to health tissues.

Volumetric modulated arc therapy can be performed using either two dose rate techniques, that is constant dose rate (cdr-VMAT) or variable dose rate (vdr-VMAT) during the gantry rotation. vdr-VMAT comes with a merit of additional flexibility in dose delivery and dose conformity to the target as compared to cdr-VMAT. Results from a study for comparison between VMAT, IRMT and 3D-CRT as delivery techniques of radiation to prostate cancer patients [39] have showed that vdr-VMAT technique resulted in more favorable dose distributions than the IMRT and cdr-VMAT techniques, sparing more of the critical organs with

optimum dose delivery to the prostate cancer. And for best clinical practice and patient care, VMAT largely reduces the number of Monitor Units (MU) required to deliver dose per treatment fraction and reduces too treatment time. However, an acceptance of low dose spread over a large volume of tissue [40] should be taken into account as the gantry rotates around the patient , showed in figure 3.3 in which the pink and dark blue isodose lines illustrate 25% and 10% dose respectively to the entire sliced body volume of the pelvis.

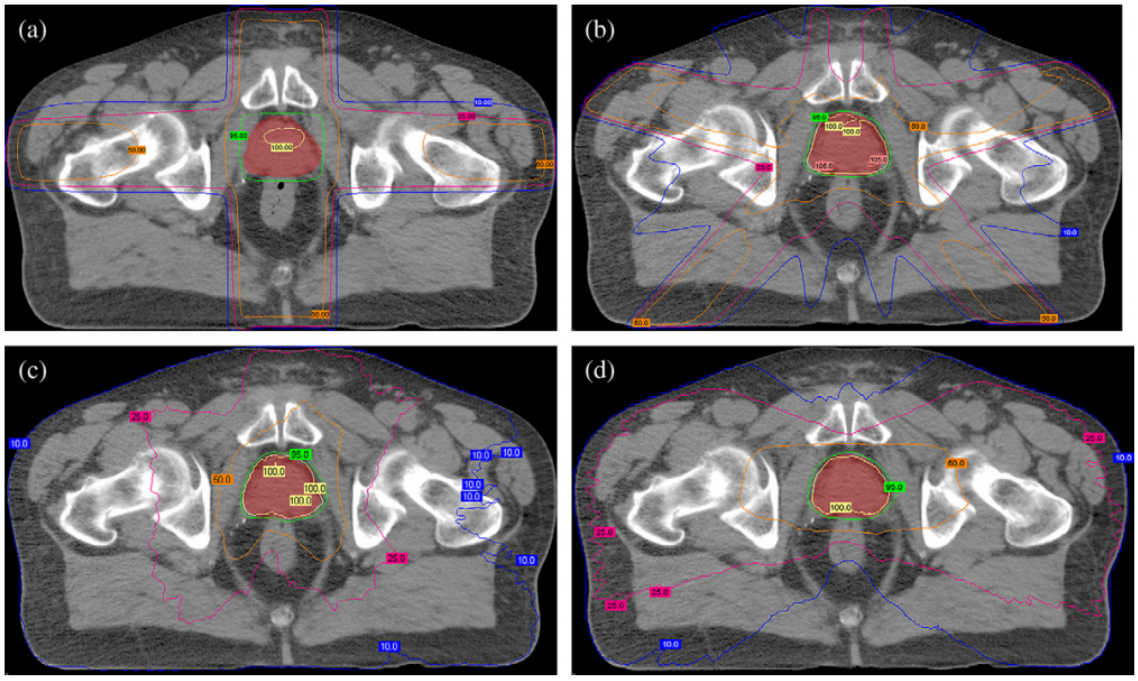

Figure 3.3: Representation axial CT slices showing isodose distribution for (a) 3D conformal radiation therapy, (b)5-field IMRT, (c) cdr-VMAT and (d) vdr-VMAT. Planning target volume indicated in red. Dose of 7,400 Gy was prescribed to PTV, with 98% of PTV covered by 95% of the prescription. Isodose lines indicated as follows: yellow-100%, green-95%, orange-50%, pink-25% and dark blue-10%. [39]

3.2 Charged particle delivery techniques

3.2.1 Passive delivery technique

For heavy ion beam therapy, particle delivery is performed either passively or through active beam scanning. The passive beam delivery system consists of the wobbler magnets, scatterer, ridge filters, compensator and beam collimators. The beam after extraction from the synchrotron is passed through a pair of wobbler magnets 90% out of phase with each other, which control the amplitude of the magnetic field with the pencil particle beam circulating around the beam axis and later passed through the a metal foil scatterer for beam broadening, producing a uniform dose distribution at the iso-center.

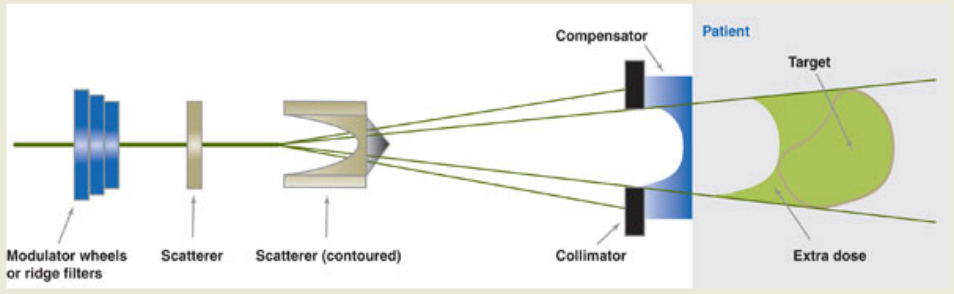

Figure 3.4: Passive beam delivery system components [41].

The beam is passed on to the ridge filters to spread out the Bragg peak in the depth-dose distribution so as to match the size of the target irradiated. The ridge filters are made from aluminium with a spacing of each bar ridge of 5 mm, figure 3.4, and it doesn't move during particle beam irradiation. They spread the Bragg peak in a range of 2cm width to 12 cm width for the aluminium height of 6 cm [42]. Further from the filter, the beam is projected through the compensator in order to precisely match the SOBP with the distal target shape and finally through the multileaf collimators for defining the irradiation field shape depending on the target of interest geometry. This setting however is for stationary targets during beam irradiation. For moving targets such as respiratory organs in a human body, a respiratory gating system that corrects for motion of the target is incorporated into the passive delivery technique.

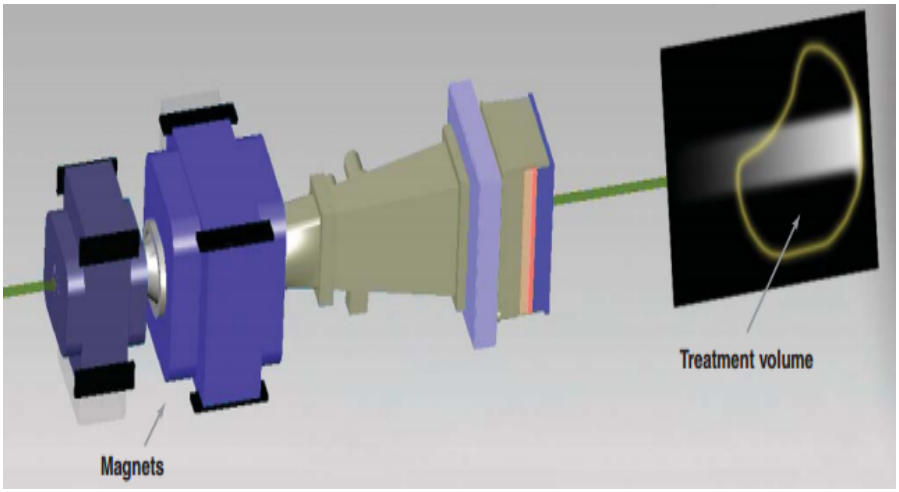

Figure 3.5: Active scanning extracted from [41]. Orthogonal magnets deflect the charged beam horizontally and vertically to physical move the spots onto the tumour site.

3.2.2 Active delivery technique

Implementation of the active beam scanning, unlike the passive technique requires no need for wobbler magnets and scattering system. Only scanning magnets are required which control the beam position by magnetic deflection for transverse direction of the beam at the target. Shifting the beam hot spot to the next scanning plane is done by adjusting the beam

energy from the accelerator. Scanning transversely through the target is performed in either spot scanning, raster scanning or continuous raster scanning in which the pencil beam is continuously turned on until all spots in a single slice of the target are irradiated.

To adjust the Bragg peak to the next slice, energy of the beam needs to be varied and this is performed by either using plastic range shifters inserted in the beam path as illustrated by figure 3.5, or by energy scanning in which the beam energy is directly varied from the synchrotron. Direct variation of energy from the synchrotron is preferred due to no introduced material in the particle beam which would produce other secondary radiation such as neutrons resulting to extra undesirable dose during hadron therapy procedures.

3.3 Online imaging techniques during ion beam radiation therapy

The idea of treating cancer tumours with charged particles like protons and carbon ions is soon progressively been utilised due to its merit in dose delivery with most of the radiation dose deposited in the last millimetre range of the particles in the named Bragg peak, however accurate precision is highly a requirement so as to correctly position the Bragg peak dose to the tumour volume such that overdose of healthy tissues and under-dose of the tumour are avoided. This has called for real time monitoring of the ion pencil beam during treatment procedures.

Real time imaging during treatment with ion beams has been possible since secondary radiation is able to emanate out of the patient with no primary radiation to the patient emitted out after beam interaction with the patient. Figure 3.6 extracted from [15] shows the different types of secondary radiation produced and emitted out of a PMMA phantom per incident ion during proton therapy of energy 160 MeV with most of it made up of secondary electrons as a result of inelastic collisions of the incident proton beam with orbital atomic electrons in the patient. Gamma radiation produced is as a result of PMMA nuclei de-excitation from inelastic proton collision with water nuclei for production of prompt gamma rays and 511KeV gamma rays produced as a result of formation of positron emmitters from nuclear reactions, secondary protons yielded from nuclear fragmentations and other secondary radiation includes alpha particles, neutrons, deutrons and stable isotopes.

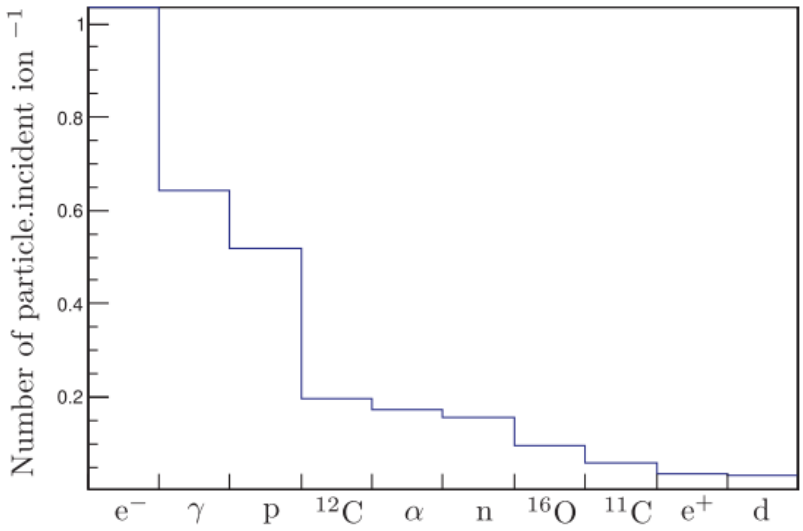

Figure 3.6: Yield of secondary radiation in a PMMA phantom during 160 MeV proton therapy extracted from [15].

To use secondary radiation for real time imaging during treatment, it needs to have a weak interaction probability to reach the externally placed detectors and further, a correlation between emitted radiation and dose deposition should be strong [43]. Modern day technology has utilised secondary 511 keV gamma rays for $in-vivo$ monitoring using PET scanners, prompt gamma rays detected either by collimated Anger cameras or Compton cameras and secondary protons utilised for imaging in the technique called Proton vertex imaging. Each of these imaging modifications has being briefly discussed in the preceding subsections.

3.3.1 PET imaging for ion beam therapy

Positron emission tomography as an imaging technique has been used for fractionated dose monitoring since 1997 and over 180 patients predominantly suffering from tumors of the head and neck, have been investigated on using this modality. For the evaluation of the sysmatic clinical benefit of PET technique, the imaging modality in Germany was integrated into the experimental carbon ion therapy unit at Gesellschaftfur Schwerionenforschung Darmstadt, Germany (GSI) [44], with advancements and changes in the PET scanner for detector configuration as well as data acquisition and processing durations to meet the requiremnts for ion therapy monitoring.

During patient treatment with stable ion beam such as ^{12}C, part of the beam collides with atomic nuclei of the planning target volume of tumour cells and through inelastic collisions and nuclear fragmentation formation produces positron emitter isotopes. Mostly ^{11}C, ^{15}O and ^{10}C with short half lives of 20 mins, 2 mins and 19 mins respectively are produced along the beam line and their positrons travel short distances about millimetres before annihilating with orbital electrons in the target volume to produce back-to-back 511MeV gamma rays detected by scintillator crystals of the PET scanner. Bismuth germanent (BGO) preferably is used as a detector crystal in the PET scanners due to its high cross section for photo-absorption of gamma radiation with no radioactivity noise from the crystal itself which is not

the case with LYSO scintillators. Figure 3.7 shows the double head positron camera which has been integrated into the carbon ion therapy beam line at the heavy ion synchrotron of GSI.

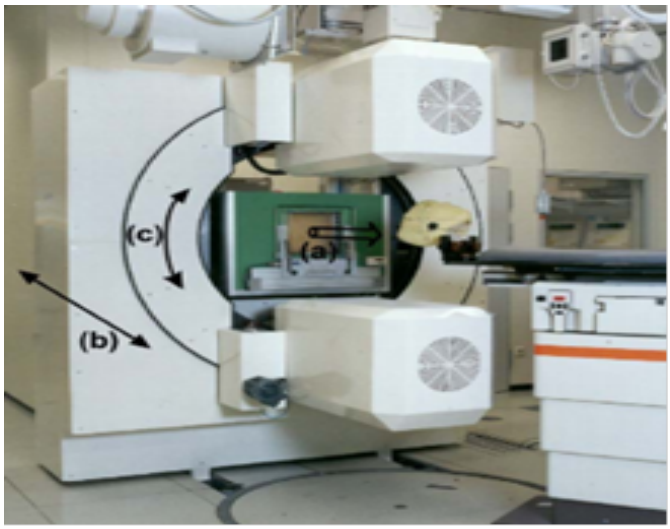

Figure 3.7, The in-beam PET facility at GSI Darmstadt [44].

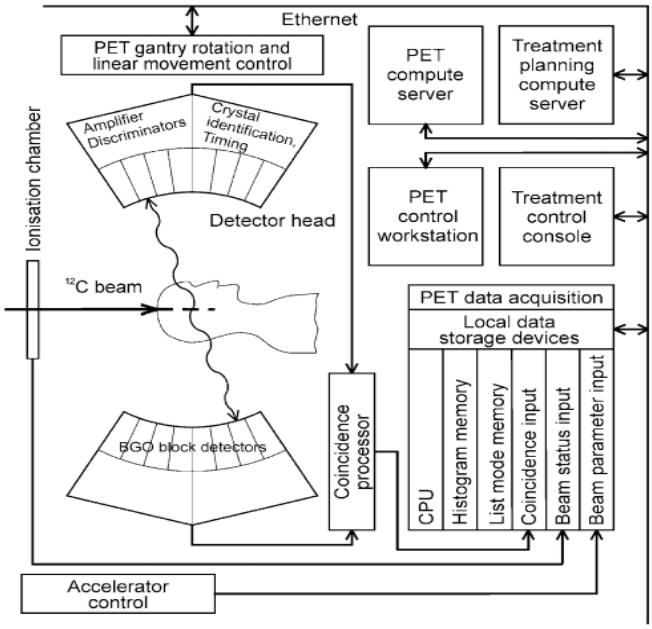

Figue 3.8, Data processing scheme at the in-beam PET facility, GSI [44] .

Position information obtained from the scintillator detectors is passed on to the data processing scheme, figure 3.8, which is designed differently depending on the electronic manufacturer. Correlation of reconstruceted PET images with CT images is done via the ethernet connection to study and monitor accurate dose delivery, however the challenges with this PET imaging technique are the time consuming off-line data processing up to 1 hour per patient and the long data acquisition times due to limited number of positron emitters produced during fragmentation processes of ion beam therapy. This has led to thoughts of better real

time modalities like prompt gamma detection and proton vertex imaging.

3.3.2 Mechanically collimated camera

At Grand Acclrateur National d'ions lourds (GANIL) in France, such a gamma detection system has been used in which the incident ion beam of carbon ions is first passed through a tagging hodoscope to correctly position the ion beam to a desired range position and registers the time frame of the charged particles. Due to inelastic collisions of the ion beam with nuclei in the target, prompt gammas are emitted radially from the target and these are passed through a collimator consisting of parralel plates usually made up of materials of high atomic number with high cross section for photoelectric effect such as lead or tungsten to photon-absorb spread out gamma rays and let through parrallel gammas to the collimator slits to scintillator crystals at the back of the collimators.

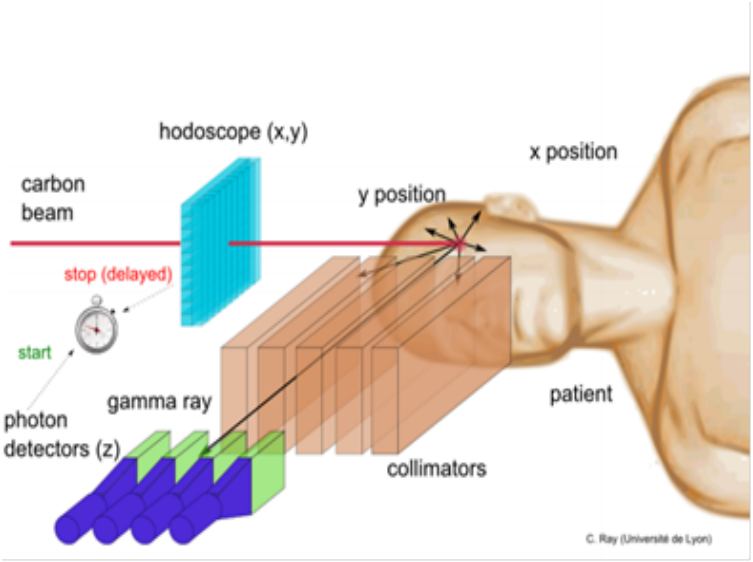

Figure 3.9: Configuration of the monitoring system during proton beam therapy and prompt gamma detection by Collimator camera [15].

Scintillator crystals preferably used are either LYSO or $LaBr_3$ due their high light yield to the Photo-Multiplier Tubes (PMT), high density and cross section favouring photoelectric effect and a good timing resolution in nano-seconds. These scintillator crystals provide timing resolutions for the detected gammas and this information together with the timing registered by the hodoscope aid in distinguishing between prompt gammas and neutrons using the Time Of Flight (TOF) technique since neutrons don't correlate with the ion beam range in the target. Thus the neutrons only contribute to the background noise in the TOF spectrum.

3.3.3 Compton camera

Another imaging system used for monitoring emission of prompt gamma radiation is a Compton camera. In Astronomy, such a camera was used to image photons with energy between

0.4 MeV and 50 MeV approximately [45] for the study of a rich variety of high energy processes and in Nuclear Medicine, they were used for imaging gamma rays from higher energy isotopes for medical use. They were also used for improving cameras use in Single Positron Emission Computed Tomography (SPECT) by lowering the dose for a given image quality or by improving image quality while delivering similar dose to patients.

The history of Compton cameras lies way back from the first imaging gamma ray detector called the Anger Camera which consisted of a lead pin hole collimator positioned in-front of a very sensitive position scintilation crystal usually made up of NaI(Tl). The first Compton telescope was designed to be a collimator rather than an imager with angular resolution of 20^0 and it consisted of a single scintillation cell at the front of nine cells [46]. The first imaging Compton camera made up of a block of germanium detector which served a plane for the camera was first built by Singh and Doria [47] which replaced the traditional mechanically collimated parallel pin hole camera used in convectional SPECT for detecting 140 keV gamma sources from decaying unstable ^{99m}Tc isotope radiaophamaceuticals injected in the patient's body. Later on Martin in [48] replaced the single position sensitive scintillator in form of a plane with a ring of 8 NaI detectors that observed a point spread function of 1.5 cm for a point source of ^{137}Cs gamma rays at 662 keV. Further development of the camera was implemented by Kamae in [49] who designed a Compton camera for determining gamma ray energy, direction and polarisation using a stack of position sensitive Silicon strips for detecting multiple Compton scattering events. Finally, a high resolution semi conductor Compton camera was built by Piercey [46] which used a single germanium as scatter detector with four germanium absorber detectors at the back. Of recent, McKisson in [50] has used an open four germanium detector array for both as scatter and absorber detectors. This has been used to acquire three dimensional images without actual tomography of the camera, a merit of Compton Cameras over Anger Camera used for medical diagnostics in SPECT.

The Compton camera uses the kinematics of Compton scattering to produce a source image without use of a mechanical collimators designed as alternatives to classical Gamma Cameras. A Compton camera consists of two or more position and energy sensitive detectors placed apart from each other. The first detector is the scatter detector usually made up of fairly low atomic number element from semi-conductors such as Silicon, Germanium or even Gaseous Time Projection Chambers (TPC) for a single Compton scattering event of the gamma ray to occur since energies in the range 100 keV to 1 MeV increase the cross section for Compton scattering [51], figure 3.10. However, Si detectors usually made up of n-type are preferred since they provide a higher percentage of Compton scattering and less Doppler broadening than the other semi-conductors. The second detector is the absorber detector made of high density inorganic scintillator material such as LYSO, NaI(Tl), Bismuth Germinate (BGO) and $LaBr_3$ to increase the cross section for Photoelectric-effect since the scattered photon has reduced energy which favours photon absorption. From Table 4, LYSO is preferred to other scintillator materials as the best option since it has relatively high density, high absorption efficiency of $3x10^{-4}$ with narrow energy resolution of 7.3, however it comes with a cost of recorded untrue events in the spectrum since it is radioactive by 277Bq/cm^3 leading to a preferred choice of BGO scintillator crystals.

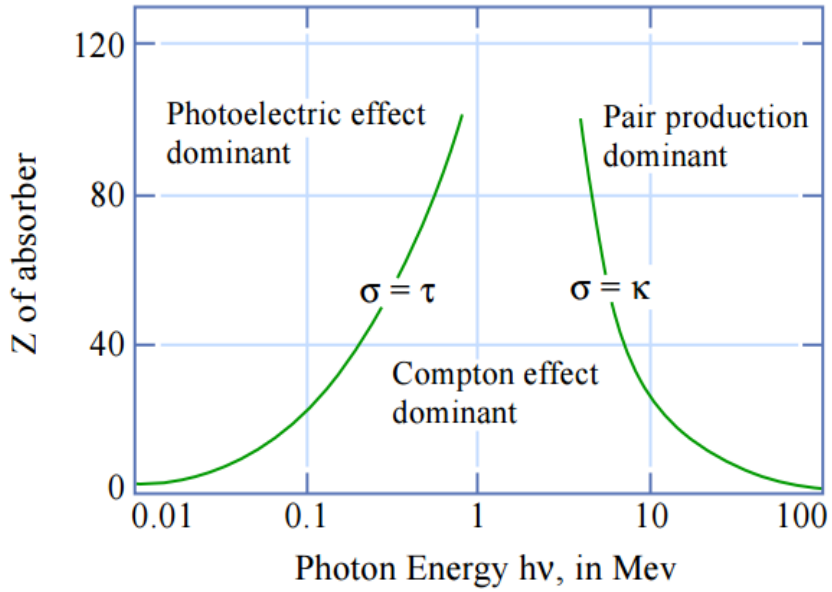

Figure 3.10, Region of relative dominance of the 3 main processes through which photons interact with matter on logarithmic scale [15].

Material	LYSO	$LaBr_3$	BGO	NaI(Tl)
Dimensions, cm(30 X 30 X ...)	4	5	4.5	6
Density (g/cm^3)	6.50	5.08	7.13	3.67
Intrinsic Radioactivity (Bq/cm^3)	277	0.4	0	0
FWHM, mm	7.3	9	7	11

Table 4, Properties of scintillator materials used in absorber detectors extracted from [45].

The scattered photon from the scatter detector is completely absorbed by the scintillator detector known as absorber detector having undergone just a single Compton scatter from the scattering detector however not all scattered photons are completely absorbed at their second and finally interaction event. Such photon incidences are best detected by Compton Telescopes [52] since they never consider total and complete photon absorption after an initial gamma ray has been scattered. But for the case of total absorption of photons at their second interaction event, the detectors exploiting this feature are Compton cameras and such precise interaction events determine the total detection efficiency and sensitivity of the Compton camera. And to maximize the accuracy of determining the scattering angle for the detector, the distance between the scatterer and absorber detectors is maximised. The camera should have an improved spatial resolution defined as the Full Width at Half Maximum (FWHM) of the point spread function (PSF) so as to clearly distinguish between two near source points of emission of gamma rays. Energy resolution of the scatter Silicon detector is calculated using the Fano formula given by

$$\triangle E_{FWHM} = 2.355w\sqrt{N_{ENC}^2 + \frac{FE}{w}} \tag{25}$$

where w=3.65 eV is the pair creation energy in silicon, N_{ENC} is the equivalent noise charge, F=0.115 the Fano factor and E is the energy deposited in silicon. Detection efficiency of

the Compton camera is also evaluated using the formula:

$$D_E = \frac{N_r}{N_i} \tag{26}$$

where N_r is the number of reconstructed Compton events, i.e. corresponding to an energy deposit in only one layer of the scatterer detector stack if a multiple layer scatterer detector is used [15] and in the absorber detector, and N_i is the number of photons emitted isotropically in 4π sr.

When the incident photon energy E_0, is known, it is possible to reconstruct cones containing the incident photon trajectory by measurement of energies deposited in both the scatterer and absorber detectors respectively using a Compton angle, θ, given by equation 27 in which m_e is the electron mass at rest and c the speed of light. The photon energy deposition points by intersection form the axis of the reconstructed cone and the apex of the cone corresponds to the Compton scatter point in the scatterer detector.

$$cos\theta = 1 - m_e c^2 \left(\frac{1}{E_1} - \frac{1}{E_0} \right) \tag{27}$$

where

$$E_0 = Edep1 + E_1 \tag{28}$$

$$E_1 = Edep2 \tag{29}$$

where E_0 is initial photon energy incident from phantom before reaching the scatterer, E_1 is photon energy after Compton scattering from the scatterer and it is equal to the energy deposited in the absorber detector $Edep2$. $Edep1$ is the energy deposited in the Si detector transferred to the Compton electron in the Si scattering detector. The deposited energy in both the scatterer and absorber detector is used to calculate the Compton angle for reconstruction of cones along the cone diagonal axis. Poor energy resolution gives a larger uncertainty in the angle of the cone as discussed later in Chapter 5, leading to a larger uncertainty in the position of the cone base thus resulting into blurring of the final reconstructed image. Other cone reconstruction uncertainties may arise as a result of position errors in the precise location of the Compton cone diagonal axis through the Compton scatter point and photoelectric effect points [50]. However to improve on the Compton Camera source point detection efficiency, an array of scattering Silicon detectors can be used like in a single scattering Compton camera in which the tracker layers , figure 3.11, are used to track the Compton electron recoiling after Compton scattering of the photon. The Compton electron information which would have been discarded, is used to restrict the Compton cone to an arc segment improving camera reconstruction efficiency. However, this requires the kinetic energy of the Compton electron to be large enough to penetrate at least one layer of the tracker array which requires typically a minimum energy of the incident photon of about 1 MeV [53].

The possible sites of origin of poly-energetic gamma rays to the scattering detector lie on the circumference of the circular base of the cone reconstructed. Images are created by overlapping cones from many interaction points (figure 3.12) and three Dimensional images can be

obtained from a fixed position on one side of the source without the need for tomography. Preferably, the Compton camera is position orthogonal to the incident primary beam to the phantom.

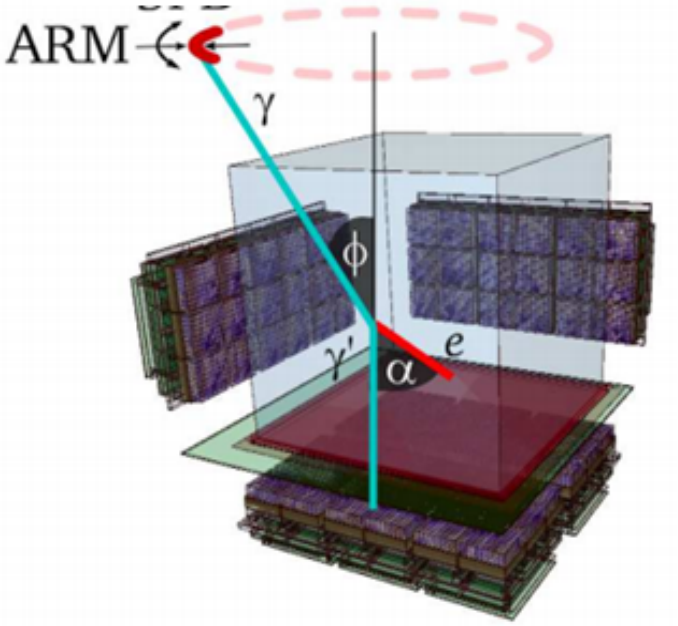

Figure 3.11: An electron tracking Compton camera made up f a gaseous Time Projection Chamber (TPC) for measuring the energy of Compton recoil electrons and tracking their progress and its absorber as Pixel Scintillator Arrays (PSAs) for measuring the energies and positions of the scattered gamma rays [54]. ARM measures the spatial resolution of the camera. γ and γ^1 represent photon before Compton scattering and after scattering through an angle ϕ. The red line shows the track of the Compton electron.

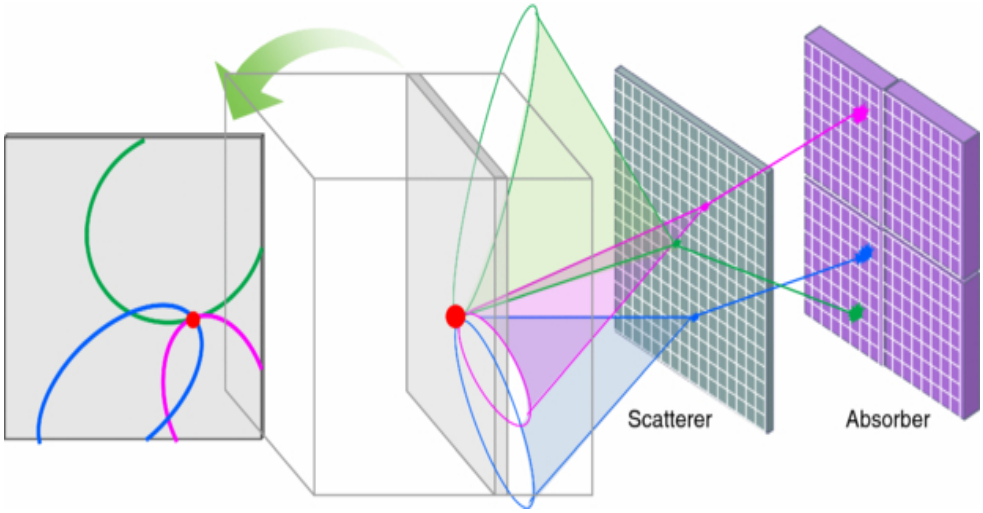

Figure 3.12: Reconstructed cones as a result of gamma scattering from the scatter detector and the red point is the reconstructed gamma source in the phantom. This has been extracted from [55].

As a result of the scattered photon being absorbed by the scintillator detector through photoelectric effect, the electrons in the scintillator are excited from their initial valence band to conduction bands across the band gap filled with an impurity and on de-excitation through the impurities, light photons are yielded and directed to Photo-detectors called Photo multiplier tubes (PMT) which through photoelectric effect produce electrons for electric signal which are further amplified in an amplifier before passed through Analogue-Digital converter (ADC) for digital signal and using the Anger Logic formula in the electron system, the position of emission of the incident gamma ray from the target material like the patient is obtained.

3.3.4 Proton vertex imaging

This is another real time on-line monitoring technique for controlling the ion range and dose monitoring in patients similar to prompt gamma imaging through which secondary protons are emitted out of the patient irradiated with either primary beam of protons or carbon ions during radiation therapy. The secondary protons originating from the primary ion trajectory posses a most probable velocity and emission direction close to that of the primary pencil beam that they are likely to penetrate the target volume (patient) and can be detected by particle detector with high efficiency [56] located downstream from the patient.

Proton vertex imaging can be done in two ways, either by double-proton interaction vertex imaging (DP-IVI) through which two secondary protons from the same origin called the vertex are considered for coincidence or by Single-proton interaction vertex imaging (SP-IVI) in which a vertex of the emitted proton is obtained by prolonged proton path in coincidence with the primary ion beam trajectory determined by the beam Hodoscope. Figure 3.13 illustrates the principle of both double and Single-proton interaction vertex imaging techniques simulation set-ups [56] on a PMMA cylinder with detection system of 50m thick silicon detector of area 10X10cm^2.

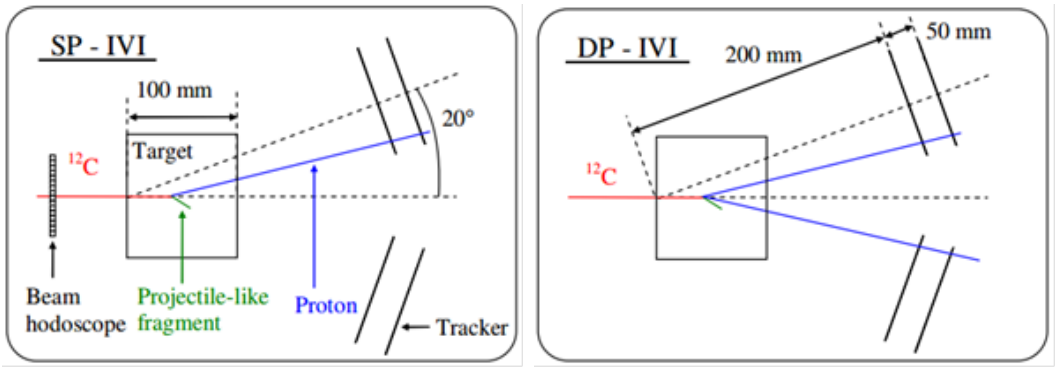

Figure 3.13: Principle of proton IVI setup. **(Left)** In the SP-IVI, only one secondary proton trajectory is required provided the incident ion beam position is determined by the tagging hodoscope. **(Right)** In the DP-IVI, two protons are produced from the same interaction vertex requiring two sets of tracking detectors for reconstruction of the interaction point along the incident beam line. Detectors are placed 5 cm apart and at 200 mm from the ion beam entrance to the target volume [56].

Simulations that have been performed in [56] show that the secondary emitted protons carry sufficient information about the range of the incident ion beam during particle therapy. Simulated results for a spherical head phantom of diameter 200 mm are shown in figure 3.14 in which the vertices yield per mm increased with increase in the incident carbon ion energy from 150 to 300 MeV/u with respective to the phantom depth. And for qualitative analysis, an error function was fitted to the distribution, the inflection point position (IPP) [43]

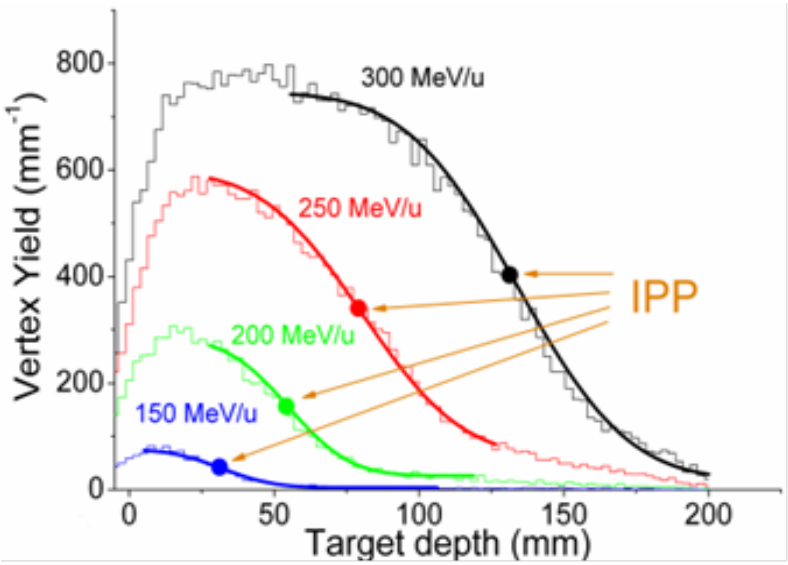

Figure 3.14: simulated results from [56] of the spherical head-phantom for the vertex yield at different carbon ion energies. IPP denotes the inflection point position of a fitted error function.

3.3.5 Proton Computed Tomography (pCT)

Most of the imaging done for patient anatomy before radiation therapy is performed using conventional x-ray CT for both photons and charged particle radiotherapy however this imaging method comes with a cost of excess dose deposited in the patient body for imaging. Additional, its accuracy for proton treatment planning is limited due to the difference in physical interactions between photons and protons with human tissue and the advantages of applying protons for imaging includes the possibility of checking and verifying the correct delivery of a proton treatment plan while the patient is in the treatment position along side reduced dose exposure to patients during imaging when using protons that have relatively a sharp precision in maximum dose delivery aimed outside of the patient or phantom volume.

To reduce on the above mentioned limitations while using photons under convectional x-ray CT scan, a new imaging technique has been developed since its proposal by Cormack in 1976 called Proton Computed Tomography (pCT). This involves use of a proton beam irradiated into a patient body volume of interest placed between two silicon made tracking telescopes for tracking proton entrance and exist position and direction so as to accurately reconstruct a map of Relative Stopping Power (RSP) and measure the energy loss deposited

in the calorimeter placed behind the second telescope as shown in figure 3.15 With such detector arrangements shown, the location and direction of protons projected into the patient at the entrance and exit of the patient or phantom can be precisely estimated and recorded using either straight line path (SLP) approximation, cubic spline path (CSP) or using their most likely path (MLP) within the object though the results in real sense tend to be affected by multiple coulombic scattering of the protons within the positively charged nuclei fields of the treatment volume [57].

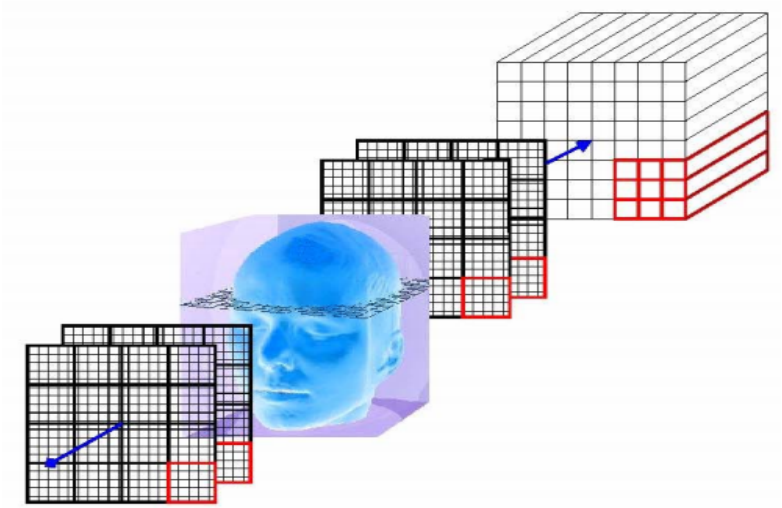

Figure 3.15: schematic set up of a proton computed tomography system consisting of an entrance and exit telescope and a multi-array crystal calorimeter to the extreme right [58].

However to obtain detailed information about the patient volume of interest, rotation of the patient target volume as illustrated in figure 4.19 if it were the human head of medical interest, is required and a large number of protons to penetrate the target is too a big necessity and from [59], 10^9 protons are a good number for human head imaging. For patient body penetration, sufficiently energetic protons are used so as they can deposit their maximum energy in form of Bragg peak in the calorimeter. For example 200 MeV protons can penetrate an adult human skull (nominal width of 20 cm in anterior posterior direction) and 250 MeV protons can penetrate an adult trunk (nominal width of 34 cm, excluding arms) [60].

4 Monte Carlo simulations

In this chapter, a brief introduction to Monte Carlo Simulation packages such as Fluka, Geant4, VMCpro, PHITS and MCNPX used for High Energy Physics and Medical Physics studies have been reviewed with much emphasis on Fluka as a tool kit used in this project. Its detailed input file format by cards and output files have been outlined and how user defined input variables in case the user is required to modify the programming code depending on the complexity of the desired problem, can be passed on to the Fluka programming code using accessible user routine files.

4.1 Monte Carlo simulations

Monte Carlo simulation is a type of simulation that relies on repeated random sampling and statistical analysis to compute the results. This method of simulation is very closely related to random experiments, experiments for which the specific result is not known in advance. Monte Carlo simulations use mathematical models like in Natural science and engineering fields to describe the interactions in a specified system using mathematical expressions called models. These models are determined by a number of input parameters, dependent on various external parameters that when processed by the models result into an outcome or many outcomes called output parameters. These are collected from a number of simulation runs and a statistical analysis is performed on the results to make a decision about the course of action [61].

Monte Carlo methods have been put to use for simulating phenomena with significant uncertainty in inputs and systems with a large number of coupled degrees of freedom. Areas of application include Astrophysics in which they are used to model both evolution of Galaxies and transmission of microwave radiation through planetary space. They also have applications from complicated Quantum Chromodynamics calculations to designing heat shields and aerodynamic forms. In experimental Particle physics or High Energy Physics (HEP), these are used to studying collision of particles like proton-proton collisions at CERN and statistically analyse produced particles. Further more in Particle Physics, they are used for designing particle detectors, understanding their behaviour and comparing experimental data to theory. Monte Carlo simulations have also been actively utilized in Medical Physics for studying dose distribution and energy deposition of charged particles like protons and carbon ions during hadron therapy as a result of ion transport through body simulated tissue. Photon radiation such as x-rays and gamma rays used for radiation therapy and imaging have been simulated using Monte Carlo simulations packages aswell.

In this project, a Monte Carlo simulation tool kit of FLUKA version 2011 has being used to study the propagation of charged particles through a soft tissue phantom, energy loss per unit length of charged particles to orbital electrons, primary beam range in the phantom and dose distribution as a result of energy deposition in the target volume. Energy deposition and absorb dose in the phantom has been correlated to the production of prompt gammas produced as an end result of atomic de-excitation after inelastic interaction of primary ions with soft tissue molecules.

4.2 FLUKA - Fluka input file

FLUktuierende KAskade, abbreviated as FLUKA, means the fully integrated Particle Physics Monte Carlo simulation software package which has been under development since 1989. It is a fortran written Monte Carlo simulation tool kit for the interaction and transport of particles and nuclei in matter. With very high precision, it can simulate interaction and propagations in matter of about 60 different particles, including photons and electrons from 1 keV to thousands of TeV, neutrinos, muons of any energy, hadrons of energies up to 20 TeV and all the corresponding antiparticles, neutrons down to thermal energies and heavy ions. The program can transport polarized photons like synchrotron radiation and optical photons and it has also been designed to track correctly charged particles with and without application of both magnetic or electric fields. Time evolution and tracking of emitted radiation from unstable residual nuclei can be also performed online. FLUKA has many applications in Particle Physics, high energy experimental Physics and Engineering, shielding, detector and telescope design, cosmic ray studies, Dosimetry, Medical Physics and Radio-biology with a recent line of development concerning Hadron therapy.

For the user to begin a fluka simulation, an input template is user chosen and access to an input file in Fluka with an extension .inp is only possible through a Graphical User Interface known as Flair which has been developed using Python as a programming language [62]. For most applications, no programming code is required from the user since FLUKA has been designed with standard output quantities. However, if special Fortran programming requirements are needed by the user, user routines such as mgdraw are used to access all parameters of interest both on primary beam and secondary particles generated.

A fluka input file is basically defined entirely by the user depending on what application the user intends to study, however there are core entries in Fluka that must be part as fundamentals to every fluka program and the input information is fed in cards using the Flair user interface. The main input cards include;

1. **INPUT TEMPLATES**
The user can choose from default Fluka templates available in FLUKA depending on the particle transport desires of interest. Available templates in Fluka include, Basic, Decay, Heavy-ions, Empty, Lattice, No geometry and Voxel templates. However, for beginning practice purposes with Fluka, the Basic template is usually preferred. For the project of proton and ion therapy, the HADROTHE default card is preferred to other default card settings since it does not have uselessly low default transport thresholds, which would be very CPU demanding but rather disposes of a fine Energy loss which facilitates accurate particle range predictions [17]. Between 125 MeV and 5 GeV per nucleon, nucleus-nucleus interactions under the HADROTHE default settings are treated with an extensively modified version of the rQMD (relativistic Quantum Molecular Dynamics) model, while the BME (Boltzmann Master Equation) model is in-charge of handling interactions below energies of 125 MeV per nucleon down to the Coulomb barrier. Inelastic hadron nucleus interactions are described by the PEANUT (pre equilibrium approach to nuclear thermalization) model. [17]

2. **BEAM AND BEAMPOS CARDS**
In these two cards, the user can define the beam particle type to be transported, its shape in X and Y direction which can be Gaussian, Rectangular or Function, beam energy and momentum, its starting position and direction to which it is desired to be propagate through the intended target set in the Geometry card. But in cases where beam sources may not easily be defined, Fortran routines are written and compiled along with the ".inp" input file.

3. **GEOBEGIN AND GEOEND CARDS**
Geometry of a Fluka setup can be defined in between the Geobegin and Geoend cards. This is done using Regions and Bodies. Examples of default bodies in Fluka include box and cylinders which are defined by their dimension sizes like length, width, height, and radius. Bodies are placed in regions, all assigned desired materials like water and air using a card called **ASSIGNMA**. For more specialised materials and compounds, if required in a simulation, can be directly accessed into an input file from the Fluka Material Data Base which contains about 500 predefined compounds. The final external region is always assigned to be a Blackhole for stopping particle transport and trajectories inoder to shorten simulation run-time.

Geometry can also be defined using the Geometry Editor of Flair or Geoviewer which gives the user a direct interaction with the regions and bodies. It comes with an addition merit of quick debugging of the geometry using a debugger since error in geometry is easily viewed by the user in **red** error messages.

4. **SCORING CARD**
Having defined the Physics processes such as BME, EMFLUO, IONFLUCT, PAIRBREM, PHOTONUC, if required, to be simulated during a Fluka run, quantities like particle fluence, energy deposition of the primary radiation beam and dose distribution can be scored using the score card. This is done by the users choice of detectors or estimators depending on what quantity is to be scored. Detectors used include;

4a. USRBIN
This detector is used for scoring distribution of one of several quantities in a regular spatial structure not dependent on the geometry. Quantities scored include energy and dose deposition, Stars as a result of inelastic interactions of the primary beam with the target material, fission, specfic activity and activity, particle fluence, net charge and momentum transfer.

4b. USRBDX
This defines a detector for particle boundary crossing fluence or current predefined by the user. The results of this estimator are given as double differential distributions in energy and solid angle in the units of $cm^{-2}GeV^{-1}sr^{-1}$ per primary incident particle beam.

4c. USRTRACK
The estimator tracks length fluence of particles during a Fluka simulation specified by the user basing on minimum and maximum kinetic energy of the particles scored. The results of USRTRACK are always given as Differential distributions of fluence in energy, in units of $cm^{-2}GeV^{-1}$ per incident primary unit weight.

4d. AUXSCORE
This allows to associate scoring detectors of given estimator types such as USRBIN with dose equivalent conversion factors and to filter scoring detectors according to auxiliary particle distribution. Other estimators include **USRCOLL** which defines a detector for hadron or neutron fluence collision and **USERDUMP** detector used for defining a collision tape and accessing secondary produced radiation like protons and prompt gamma radiation through activating calls to the user routine MGDRAW. This estimator card has been greatly used to dump information about emission of secondary radiation in this Project using the preferred mdgraw.f user routine. A few other user routines that can be run along with the Fair Fluka input file include abscff.f, comscw.f, endscp.f and usrout.f. More routines can be found the Fluka manual [62].

5. **START CARD**
This aids in allocating the number of primary particles to be transported through the target medium.

Simulated results for particle transport through a user chosen target are printed in an output file with an extension .out which reports all details and events of the simulation in a summary file and in cases of errors during the simulation run, an error file showing possible error sources in the run is included in the output file. Different estimators and detector mentioned above output data in different user chosen formats either formatted or unformatted and special detectors like **SCORE** outputs data into a standard output format 11 included in the output file. Detectors such as **USRBIN** can read output data files with extension .bnn and plot data in 1D or 2D however, detectors like **USRDBX** and **USRYEILD** can only read binary output fortran data files when first run in fortran programs such as USXSUW and USYSUW respectively which read binary output files and compute standard deviations. They return three files of which the first is a binary file read at any time by the program, the second file is an ASCII text file contaning commented information for the printed results for easy user intepretation and the third is another ASCII text file containing tabulated data in 4 columns easy for data plotting by either **USRDBX** or **USRYEILD** estimators.

Alternatively, other simulation tools that have not been used in this project work such as **Geant4**, **VMCpro**, **PHITS** and **MCNPX** can be used to investigate particle transport through matter.

5 Discussion of results

5.1 Simulation methods and results

In this chapter, Monte Carlo simulation results of both beams of 160 MeV proton and 300 MeV/u carbon ion beams projected into a soft tissue cube are represented. Energy deposition of the primary beam, primary particle fluence, yield of prompt gamma radiation with respect to production positions, inelastic nuclear interactions between the primary beam particles and soft tissue atomic nuclei, production of secondary radiation such as photons, neutrons and protons and finally energy and angular distribution of both photons and secondary protons.

5.2 Simulation methodology

A default Fluka template of HADROTHE which disposes of a fine energy loss that facilitates accurate particle range predictions and nuclear interactions for proton therapy has been used in all simulations. A 160 MeV proton pencil beam of FWHM 0.01 cm with a lateral Gaussian distribution is projected into a cube of dimensions 20cmx20cmx20cm. The material assigned to the cube is soft tissue extracted from the material data base as soft tissue (ICRP) consisting mainly of Hydrogen-2, Oxygen-8, Nitrogen-14 and Carbon-12. Other constituents include Mg, P, Cl, Ca, Zn, Na, Si, S, K and Fe. The pencil beam is positioned -5 cm from the z-direction with origin (0,0) coordinates for x and y direction respectively. It is projected in the positive z-direction through the soft tissue target encapsulated with a void region filled with vacuum and finally with a black hole to terminate particle transport and trajectories.

For my study considerations, simulations of 10^7 primary protons of 160 MeV and 300 MeV/u carbon ions have been run along with a Fluka user routine known as Mgdraw.f which is user accessible through the USRDUMP scoring card. The Fortran user routine script contains information of the secondary produced particles such as prompt gammas via the USDRAW entry of which secondary particle information is stored in the COMMON BLOCK known as GENerator STacK (GENSTK) 'INCLUDE' file of the Mgdraw file. Whenever a hadronic inelastic ineraction occurs in the simulation, the mgdraw file via the usdraw entry is called to store secondary particles with their parameters such as particle identity, its kinetic energy, direction of propagation, its weight and age. Other entries in the mgdraw card include BXDRAW, EEDRAW, ENDRAW and SODRAW. Simulation of the primary proton trajectory was run for 5 cycles to collect data from the fluka estimators and used detectors included USRBIN, USRTRACK and USRDBX as previously described in Chapter 4. To score gamma fluence and secondary proton fluence, a USRBIN detector was used of the exact dimensions of the soft tissue cube in order to score all particles crossing from the target volume to vacuum per unit area. The same detector is used to score dose deposition of the primary protons in the soft tissue. Angular distribution of prompt gammas and secondary particles is registered by the USRDBX estimator.

5.3 Results

5.3.1 160 MeV proton beam simulation

The interaction of the charged primary proton beam with soft tissue involves ionization and excitation of orbital electrons leading to energy loss of the charged protons to the medium. The amount of energy per unit length lost by protons increases with penetration depth of protons since the primary beam is gradually slowed down in velocity interacting more with the medium as predicted by the Bethe Bloch theory and this occurrence exactly corresponds to the amount of energy deposited by the primaries in the medium per unit mass propagated. This is the so called absorbed dose and figure 5.1a) shows dose deposited in the cubic soft tissue with respect to the proton depth. From figure 5.1a) and 1b), the proton range deep inside the target volume is visualized to be about 16 cm using the generated Bragg peak with a very sharp distal fall off of dose. Beyond the Bragg peak, there is a very small dose deposition nearly negligible and this is due to dose deposition by secondary neutrons that move in the forward direction of the main primary proton beam depositing energy in the soft tissue cube. The sharp and maximum dose deposition of the primary proton particles has been one of the key advantages of using proton therapy as organs at risk beyond the tumour target volume are spared from unnecessary radiation dose.

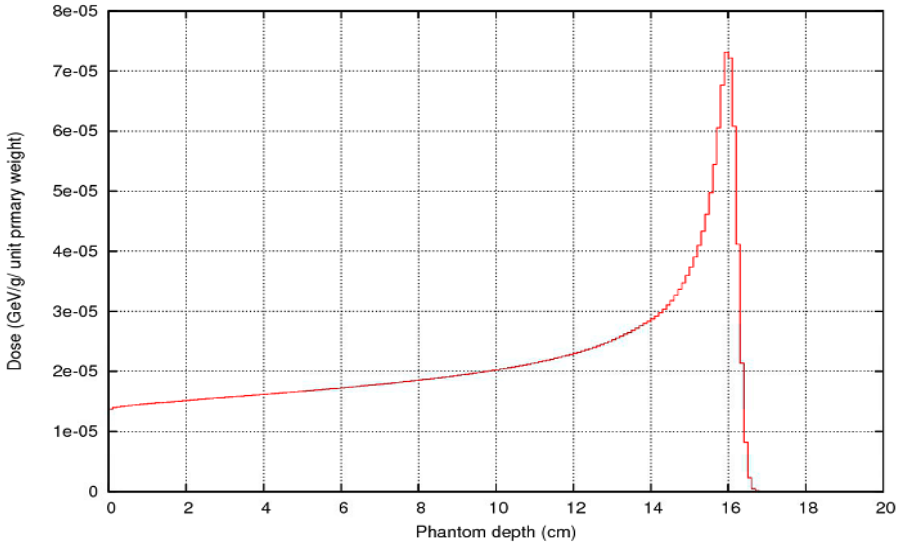

Figure 5.1a) Simulated dose-depth profile of a 160 MeV proton beam (10^7 primaries) into a phantom consisting of soft tissue.

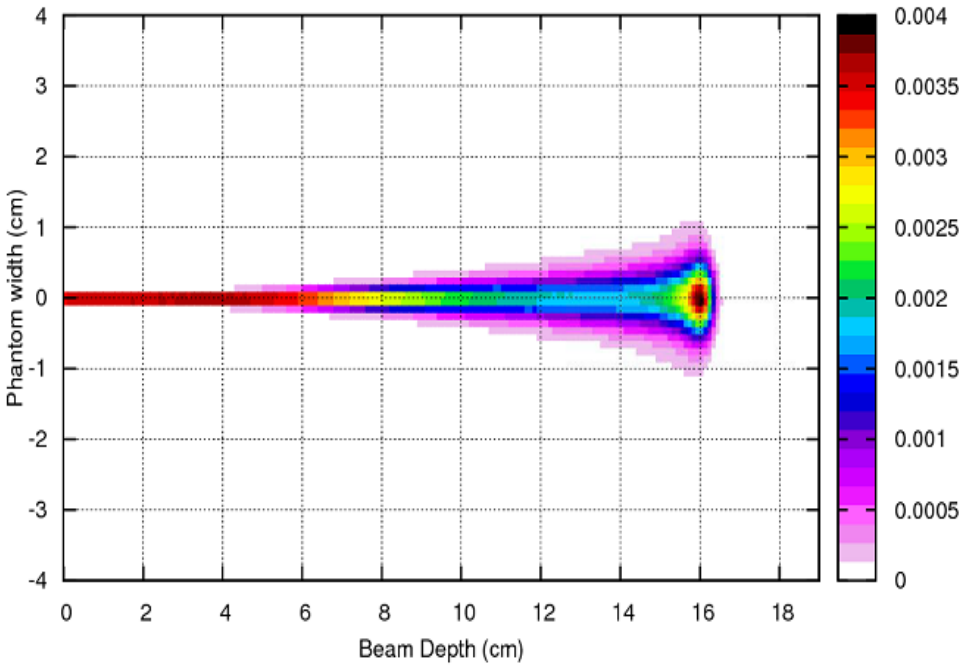

Figure 5.1b) 2 Dimension dose depth profile showing the proton range and Bragg peak position.

The proton pencil beam widens as it travels through soft tissue due to elastic interaction and scattering of the primary proton beam with soft tissue nuclei forming a beam broadening. From figure 5.2.1, analysing the angular distribution of protons, most of the protons are emitted in angles less than 90^0 with few back scattered at angles greater than 90^0. These are due to formation of daughter nuclides which decay by release of a proton that can be spit out of the nucleus in any direction. This figure shows an exponential decrease in the number of protons detected as the angle between the secondary proton trajectory and that of the main beam increases to 90^0. This shows that secondary protons which are a result of inelastic nuclear interactions are forward directed in the original direction of the primary beam with most protons having total energy values in between 8 MeV and 12 MeV while a progressive decrease in number of protons counts is recorded with increment in proton energy. Such protons arise as a result of being elastic scattered off their initial direction of propagation having lost most of their energies along the primary beam. The concept of detecting secondary protons has been fully utilized in positioning of proton scintillation detectors during Proton Vertex Imaging owing to the directional knowledge of secondary protons as clearly illustrated in Chapter Three Figure 3.13. Figure 5.3 shows the distribution of secondary proton count with respect to their energies of ejection.

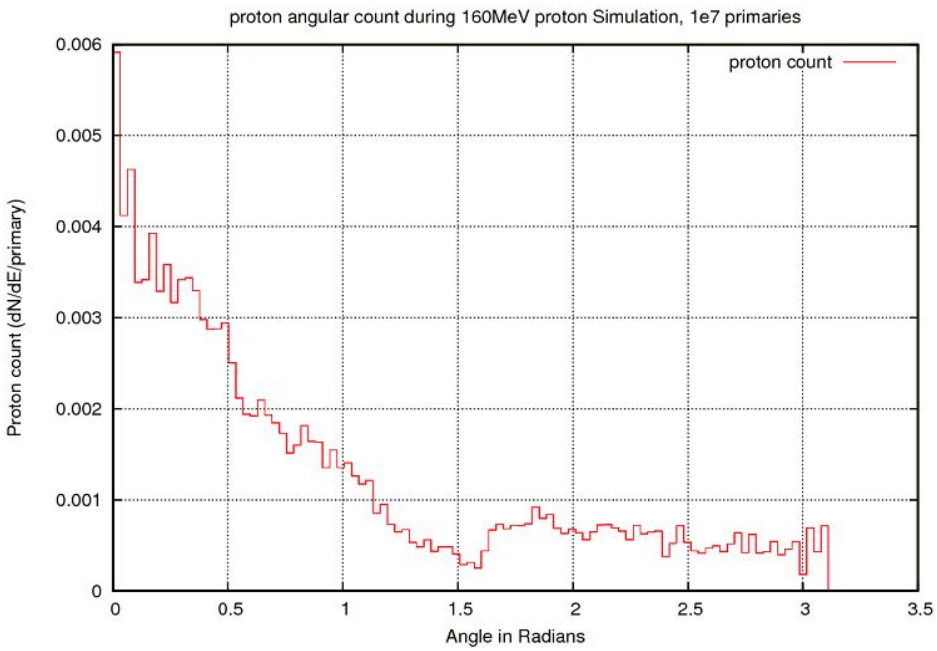

Figure 5.2.1: Angular distribution of secondary protons during a 160 MeV proton beam simulation. A few protons are emitted opposite to the primary beam direction with the majority projected at angles less than 90^0.

Figure 5.4 and 5.5 illustrate the proton fluence of the primary pencil beam with phantom depth. The number of protons crossing a unit area gradually falls off from 0 cm to 16 cm depth after which the fall off is seen to be rapid in an interval range of 12 mm. This gives practical information about the primary proton range.

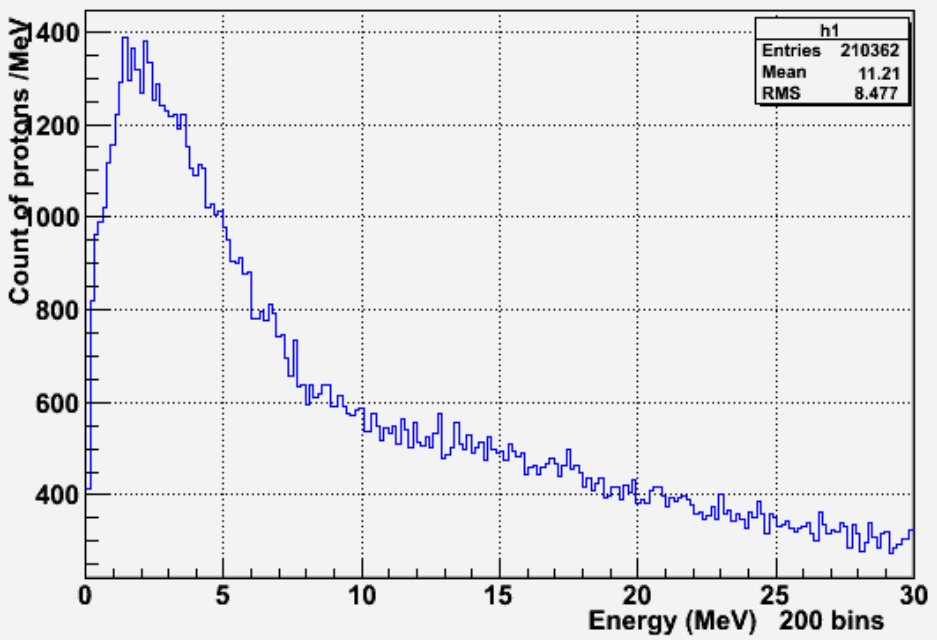

Figure 5.3: Energy distribution of secondary protons in the forward direction obtained during a 160 MeV proton pencil beam simulation.

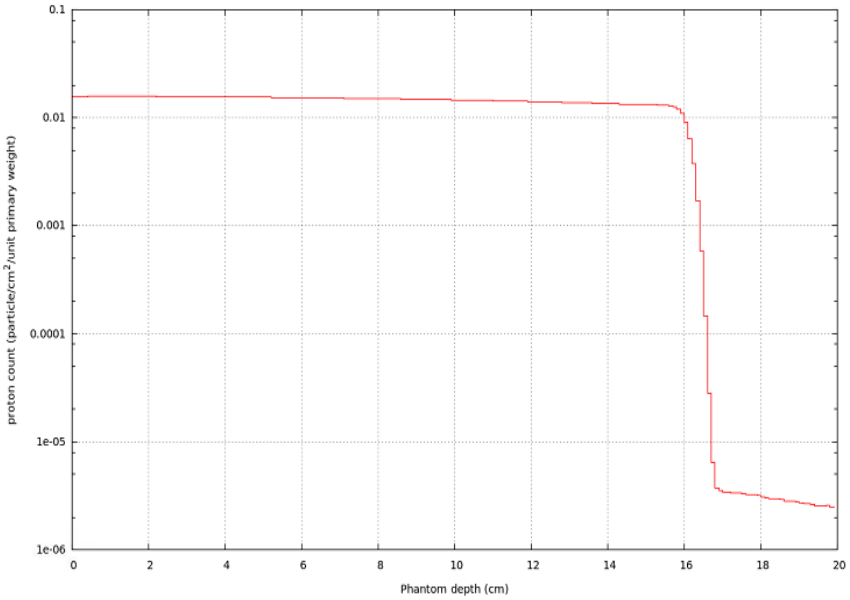

Figure 5.4: A logarithmic plot of proton fluence with a steep fall off near the maximum proton range. A small count of protons is evident beyond the main beam proton range, a contribution from secondary protons after nuclear reactions.

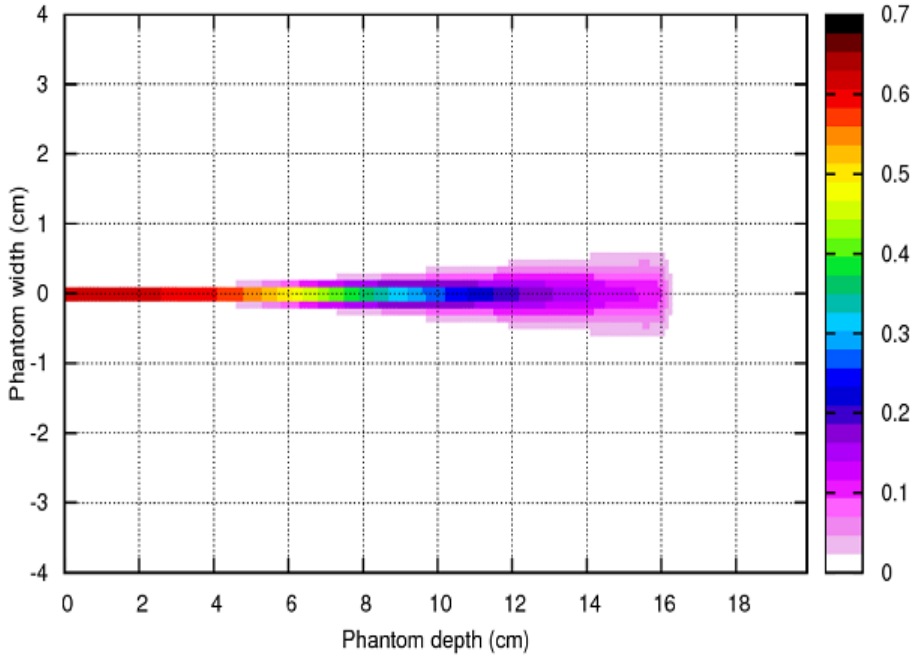

Figure 5.5: Two dimension Monte Carlo proton fluence representation of 160 MeV proton into soft tissue.

As mentioned earlier on, the primary beam of protons loses its kinetic energy through interactions such as electron orbital ionization and excitation and inelastic nuclear interactions. From the 160 MeV proton beam simulation using Fluka, a study of counts of inelastic nuclear interactions that lead to formation of nuclear excitations have been included in the study. The number of such interactions per primary proton particle also known as stars

in the simulation package gradually increases from a few millimetres depth to 14.8 cm and a sharp fall off in the counts is evident beyond 15 cm depth, about one centimetre before the Bragg peak region at 16 cm mark in the phantom. This is because much of the proton beam energy has been lost to the target as the primary beam is slowed down. No count of inelastic interactions is recorded beyond the Bragg peak region, Figure 5.6, as no primary proton particle exceeds the maximum range of particle transport.

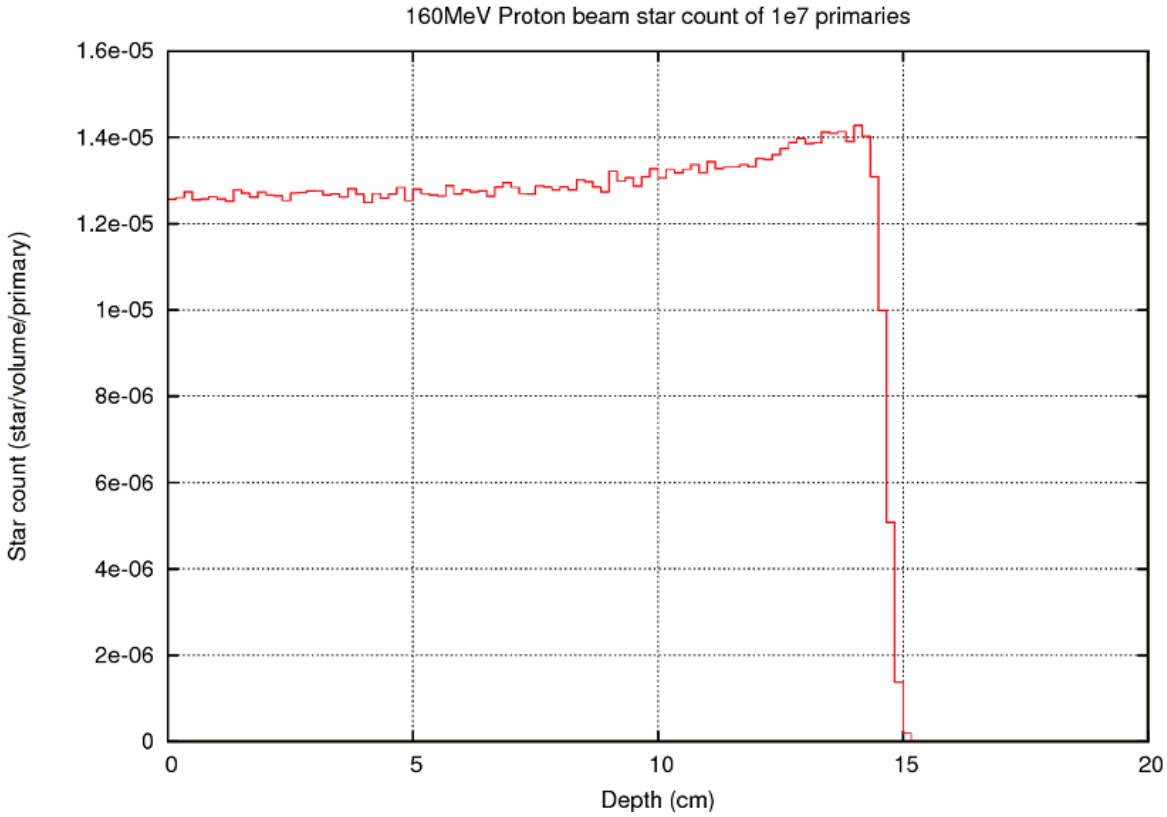

Figure 5.6: Monte Carlo simulation of inelastic interaction yield with proton depth into a soft tissue phantom during a 160 MeV proton beam simulation.

Prompt gamma radiation which emanates out of the target during irradiation of the target volume with 160 MeV proton beam has been our main target of interest. These are due to inelastic interactions that occur between the primary proton beam and soft tissue nuclei that daughter nuclei in excited states are formed and on de-exciting, gamma radiation is emitted out of the target volume. The sample of soft tissue used in this simulation contains mainly of ^{14}N, ^{12}C and ^{16}O. These are the major elements when in excited states decay through gamma emission. Other soft tissue constituents include Magnesium, Sulphur, Potassium, Iron, Zinc, Calcium, Chlorine, Phosphorus, Sodium and Hydrogen atoms. Gamma fluence has been recorded, figure 5.7, for the number of prompt gamma leaving the target volume per unit area and during the simulation, no energy threshold has been included to eliminate low energy photons. The simulation includes gamma radiation which is due to neutrons produced as a result of nuclear interactions. Such gamma radiation has typically energies

less than 1 MeV. The energy range from 0 MeV to 1 MeV also includes electron-positron annihilation gammas with characteristic energy of 0.511 MeV. This annihilation gamma radiation currently is used in clinical set-up to monitor proton and carbon ion range and dose distribution using Positron Emission Tomography (PET) scan detectors made of scintillation crystals after particle therapy for cancer tumours.

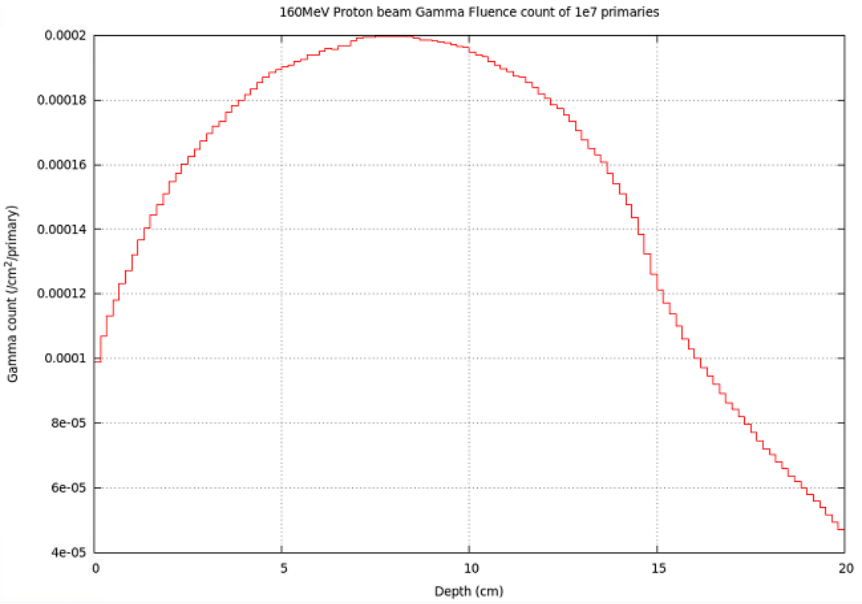

Figure 5.7: Count of gamma radiation leaving soft tissue per unit area during the 160 MeV proton pencil beam simulation.

A mono-energetic 160 MeV proton pencil beam generates poly-energetic prompt gammas when irradiated in the soft tissue. Prompt gammas emitted are of various energies since the soft tissue used in the simulation is composed of various chemical components of different densities, ionization energies and composition to the soft sample. An energy spectrum of the prompt gammas is shown in figure 5.8 with peaks at energies of values 2.3, 4.4, 5.1, and 6.2-7.1 MeV. The de-excitation energy of 4.4 MeV corresponds to gammas emitted from an excited ^{12}C nucleus and 5.1 MeV together with 2.3 MeV [63] correspond to an excited nucleus of ^{14}N. A contribution to the 2.3 MeV energy peak is attributed to the slow neutrons captured by Protium (^{1}H) nuclei to decay by emission of gammas with this energy value as a result of de-exciting to Deuterium (^{2}H). Deuterium is one of the secondary particles produced after nuclear interactions within the soft tissue phantom [64]. A shorter peak of prompt gammas emitted from excited ^{16}O nuclei is evidenced in the range 6.2 to 7.2 MeV and it is these three to four energy peaks exploited as main sources for prompt gamma radiation used to monitor on-line proton range into target volume and for in vivo dose distribution analysis of energy deposited by charged particle into the target since their production rate in time interval of a pico-second directly correlates to energy deposition in the target.

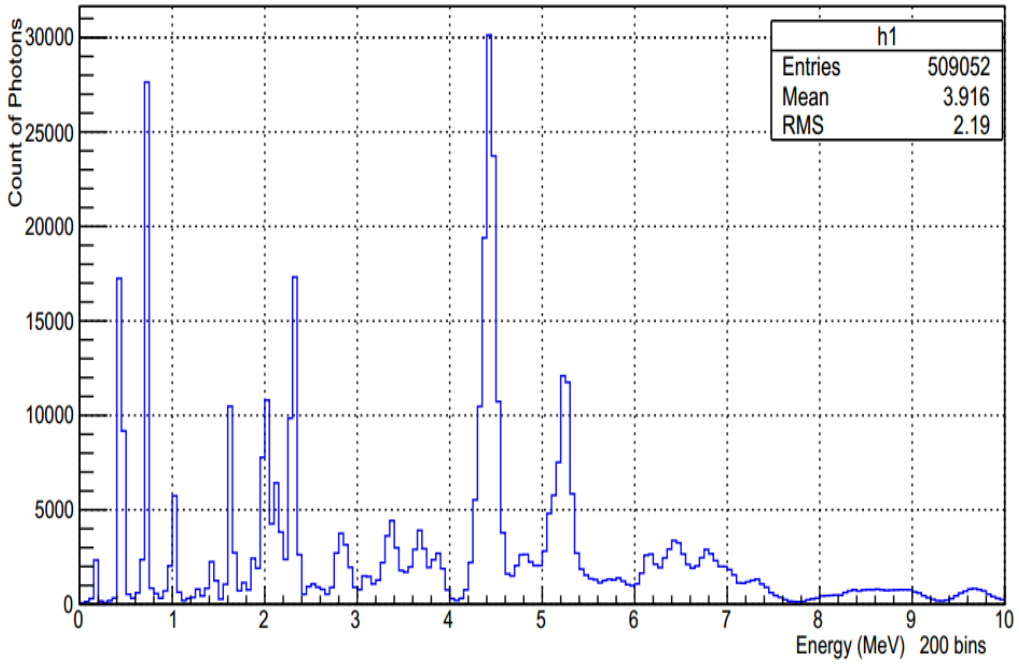

Figure 5.8: Energy spectrum of photons produced during a 160 MeV proton beam simulation.

5.3.2 300 MeV/u carbon ion pencil beam simulation

As part of the hadron group of particles used for particle therapy, carbon ions have taken a big step in cancer treatment and their interaction in the simulated body tissue has been included in this study. A carbon ion pencil beam of 300 MeV/u with a Gaussian distribution of FWHM value of 0.1 mm and 10^7 primary particles has been used as the main radiation beam to a soft tissue volume of dimensions 20x20x20cm^3 placed 20 cm in the positive z-direction of the beam with the primary beam starting at 5 cm mark from the back of the phantom.

Due to the heavier mass and charge of carbon ions, when irradiated into the target volume, they lose most of their energy through ionization leading to formation of electrons and ions. Densely ionizing carbon ions deposit most of their energy at the extreme end of their propagation trajectory, the Bragg peak showing a clear similarity with protons as shown in figure 5.8, however the carbon ion Bragg peak positioned at 16.3 cm has a 4 mm width at FWHM, smaller than that exhibited by proton energy loss which is 2 cm, with an escalated biological effectiveness in the peak region of about 3-5 times more than that of protons causing irreparable clustered DNA damage to tumour cells. This feature of carbon ions has been taken merit of in therapy procedures as a tool for treating deeply sited and strong radiation resistant tumours in medical clinics.

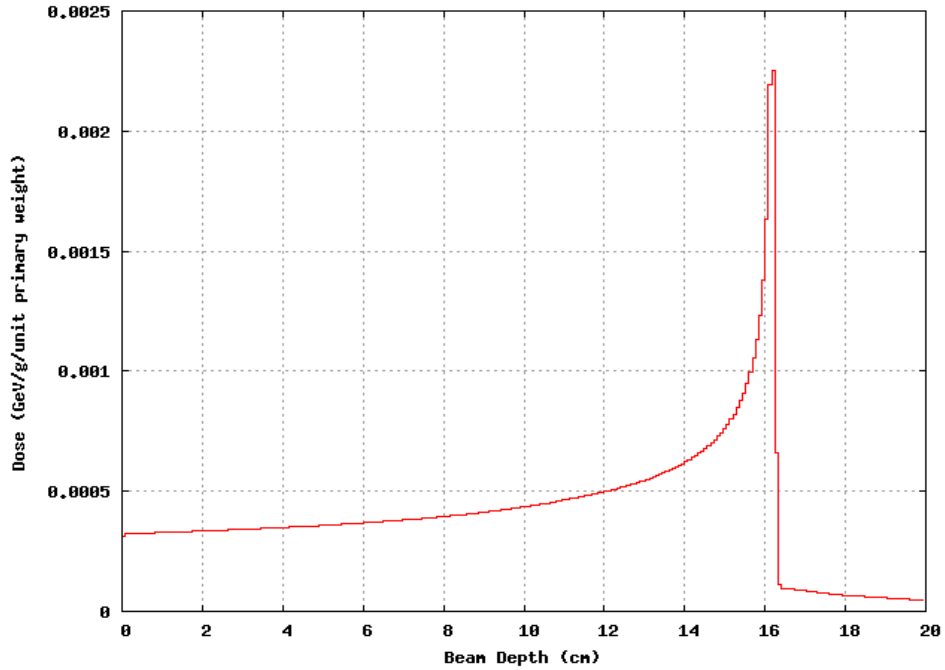

Figure 5.8: Graphical representation of dose absorbed in the soft tissue volume during a 300 MeV/u ^{12}C ion beam simulation. Some dose is registered beyond the peak fall off region.

From figure 5.8, a low dose profile beyond the sharp distal fall off is registered in the simulated interaction of carbon ions with soft tissue. This arises as a result of formation of nuclear fragments such as neutrons, protons and alpha particles that gain sufficient energy from the primary carbon ion beam that they undergo energy loss to soft tissue at distances beyond the Bragg peak depositing a significant dose. This excess dose deposition beyond the critical tumour site protruding to health cells in the vicinity of the tumour cells can lead to development of secondary cancer.

From the study of protons illustrated in figure 5.1b), the beam of protons undergoes large elastic scattering and straggling in the Bragg peak region more than the carbon ion beam. This is due to protons being less massive than carbon ions that they are easily scattered off their beam path as they slow down with a decrease in their energy and increased coloumbic repulsion between positively charged protons and soft tissue nuclei of the same charge. Figure 5.9 shows the 2D view of a 300 MeV/u carbon ion beam and how it undergoes minimal lateral scattering and transverse straggling in the Bragg peak region.

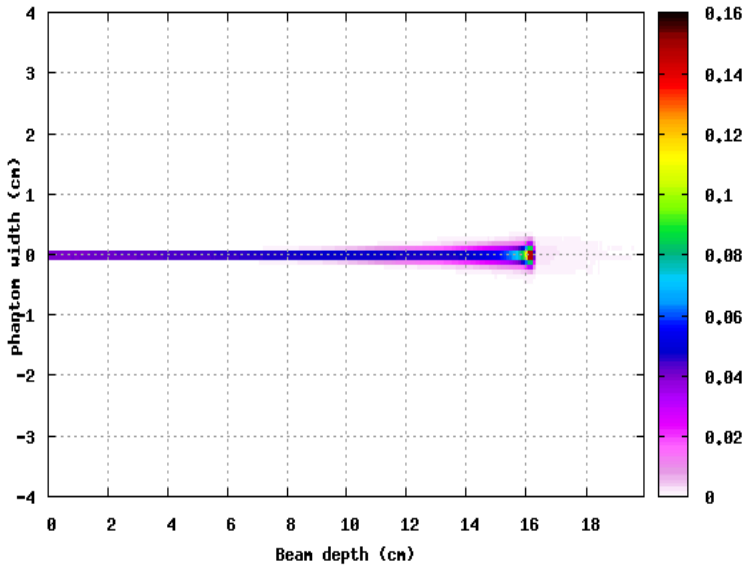

Figure 5.9: Two dimensional view of carbon ion incident projection with less lateral scattering and transverse straggling.

The count of nuclear inelastic interactions as a result of heavy carbon ions directly colliding with tissue nuclei which lead to formation and emission of prompt gamma radiation analysed in the recent studies in [8] has been as studied before for 160 MeV proton beam simulation, included as part of investigation for studying prompt gamma emission illustrated in figure 5.10 for a heavy ion beam. From the plot, the number of such interactions leading to formation of nuclear fragments and excited nuclei is evenly distributed with respect to the carbon ion beam depth with an approximation of 5 times more inelastic nuclear interactions occurring per primary carbon ion than per proton particle analysed earlier on in figure 5.6. The star count with beam depth reaches its maximum depth range at 15.8 cm, a few millimetres behind the Bragg peak with a few registered inelastic nuclear interaction counts beyond the Bragg peak. This is due to the secondary produced neutrons and protons leaving the main beam trajectory and interacting with atomic nuclei. A total of 17,720 nuclear inelastic interactions was registered for this simulation with 81.0% of the total number occurring as a result of the primary carbon ion beam and the rest of the percentage contributed by the secondary fragments formed such as tritium, deuteron, neutrons, 4-helium and 3-helium but especially from neutrons.

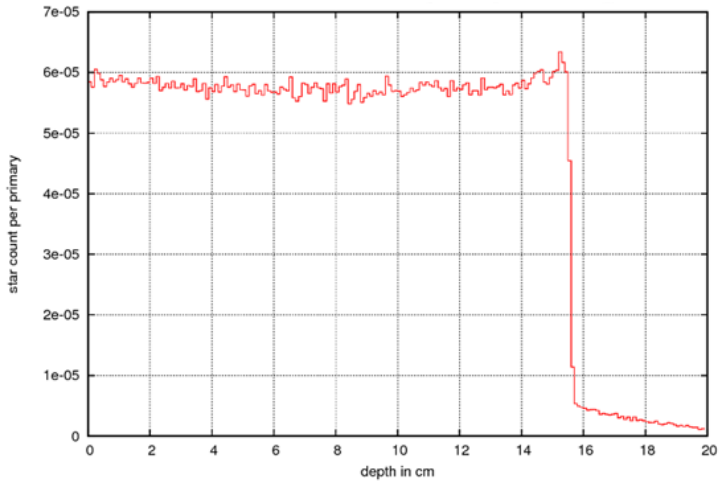

Figure 5.10: Distribution of inelastic interaction points along the ^{12}C ion penetration depth during a 300 MeV/u ^{12}C simulation of 10^7 primaries.

The prompt gamma radiation emitted as a result of de-excitation of nuclei exhibit a large spectrum of energies ranging from a few keV to over 10 MeV but for our study purposes, an energy range till 10 MeV was considered, figure 5.11, as it was the case for 160 MeV proton beam. Sharp peaks are seen at 2.2 MeV, 4.4 MeV, 5.2 MeV and 6.6 MeV corresponding to de-excitation of ^{14}N,^{12}C, ^{14}N and ^{16}O nuclides respectively. High energetic photons above 10 MeV that are not included in this study scope are as a result of de-excitation of collectively excited nuclei as a result of heavy ions collisions and inelastically interacting with atomic nuclei in a phenomenal called Giant Dipole Resonance (GDR) leading to vibration and oscillation of both protons and neutrons in opposite directions before the entire nucleus is de-excited for highly energetic gamma emission before a neutron is emitted out of the nucleus [65]. A slowly raising peak in between the energy range of 3 MeV to 4 MeV is due to nuclei de-excitation of ^{20}Ca nuclei in the soft tissue sample. Formation of PET isotopes such as ^{11}C, ^{13}N and ^{15}O which lead to emission of positrons that annihilate with abundant electron supply at short distance of about a millimetre in the target volume to form low energy gamma radiation has been included for this study as well as gammas due to thermal neutron capture in the soft tissue sample.

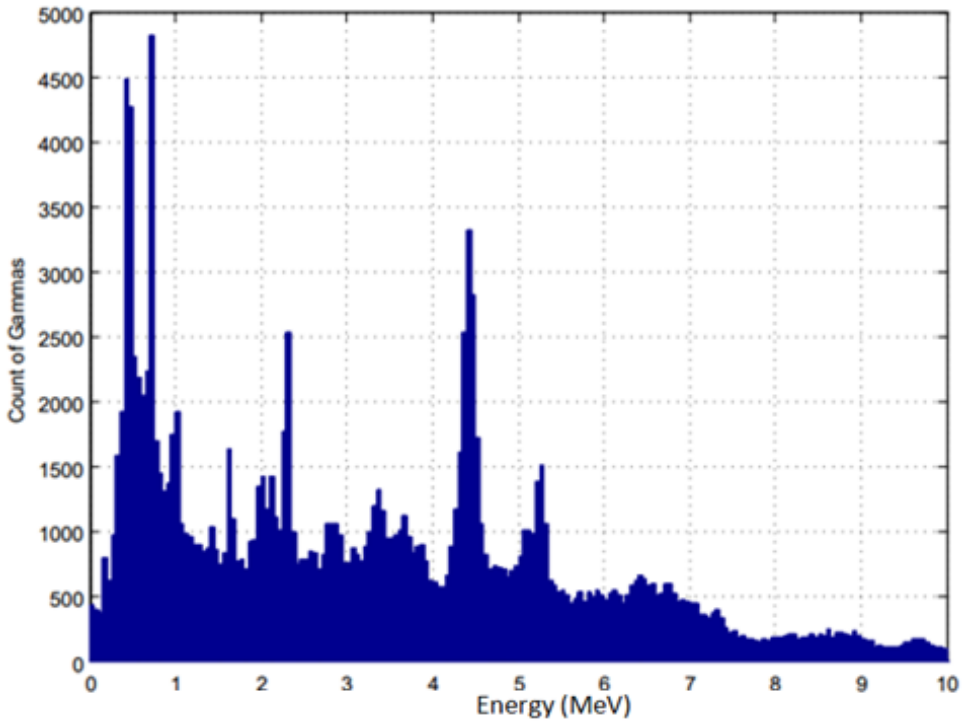

Figure 5.11: Energy spectrum of photons produced during a 300 MeV/u ^{12}C beam simulation on soft tissue.

The 300 MeV/u carbon ion simulation with Fluka, version 2011 has registered a number of secondary radiation with 23.1% of the secondaries generated in inelastic interactions per beam particle giving rise and formation of 4-Helium, 5.2% due to 3-Helium, 3.2% due to Triton, 8.7% to Deuteron, 22.2% due to neutrons and 30.8% contributed by secondary protons as represented in figure 5.12. From the energy spectrum of the emitted neutrons, most of the counted neutrons arising as a result of nuclear interactions are thermal neutrons with energies below 0.7 MeV and it is these neutrons captured in the soft tissue volume to form low energy gammas. Few counts of secondary neutrons with energies over 2 MeV are emitted out of the target, figure 5.13, to reach the detector thus contribution to background and it is these neutrons that lead to a considerable noise in imaging systems.

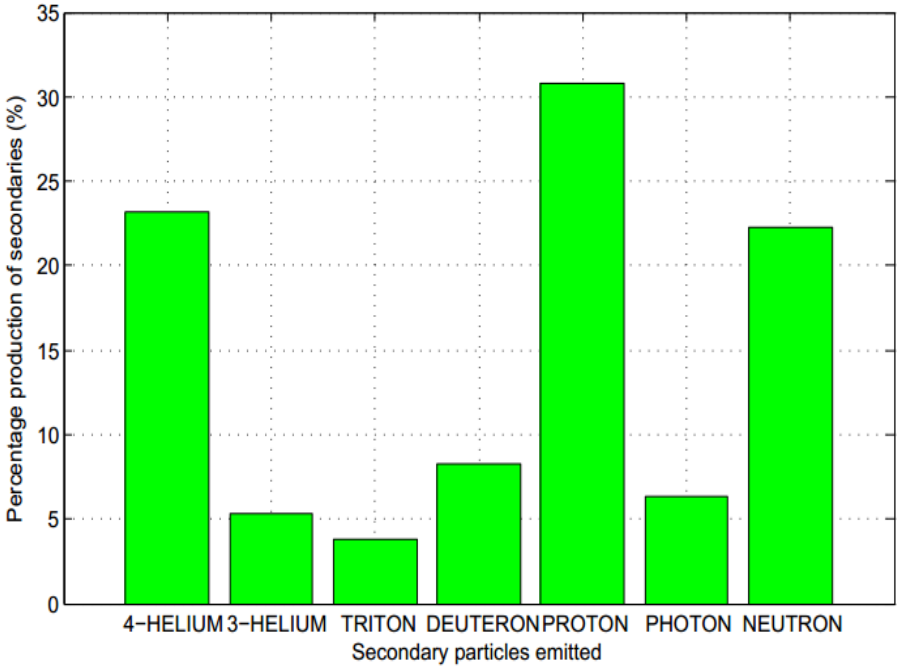

Figure 5.12: Production yield of secondary particles as a result of 300 MeV/u carbon ion beam of 10^7 primaries irradiated into a soft tissue phantom.

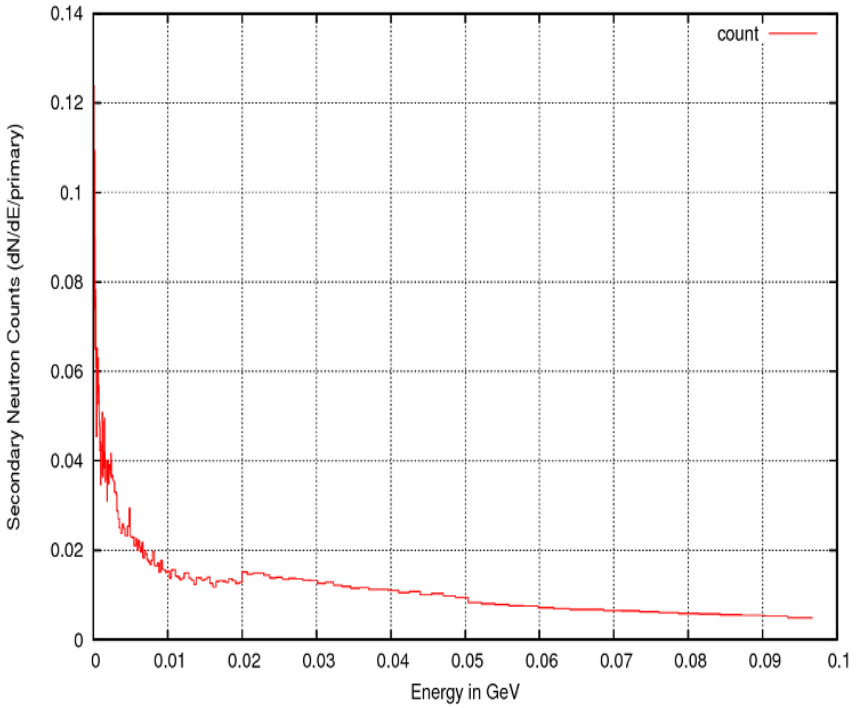

Figure 5.13: Neutron energy spectrum produced during the 300 MeV/u ^{12}C ion pencil beam simulation of 10^7 primaries for all angles of neutron emission.

In this simulation, 30.8% of the secondaries generated in inelastic interactions per beam particle are protons with a wide range of energies. High counts of protons are registered in figure 5.14 with most protons having energies in the range 50 to 100 MeV. The energy spectrum of

protons illustrates a wider yield of protons emanating from the soft tissue sample and this is attributed to the two categories of protons origin. Some of them as secondary protons are due to nuclear interaction between the primary carbon ion beam and soft tissue atomic nuclei and the rest of the proton contribution is due to composition of protons as part of carbon ion beam moving in the beam direction which undergoes elastic collisions in the soft tissue volume.

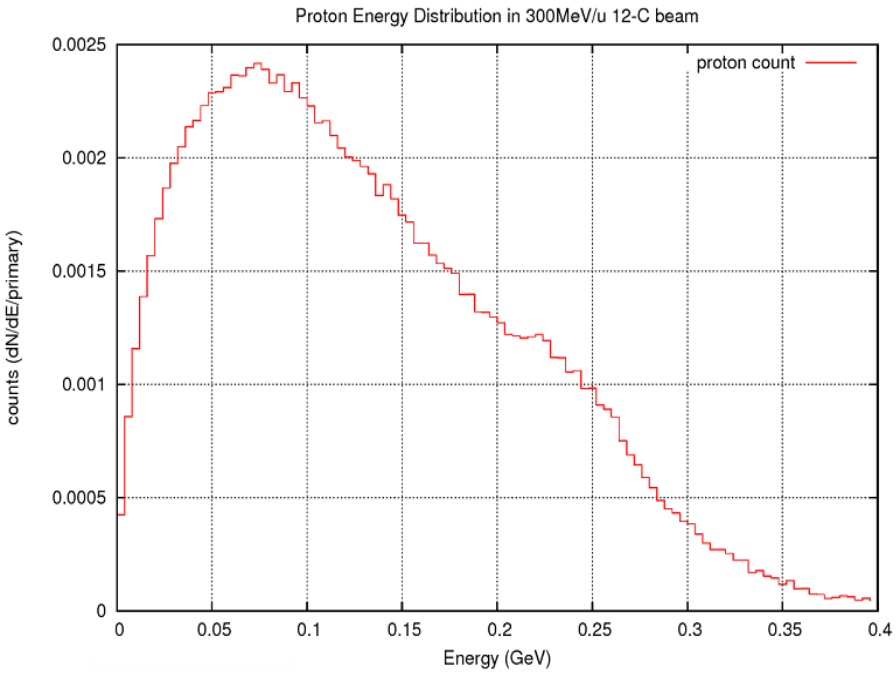

Figure 5.14: Energy spectrum of secondary protons during the 300 MeV/u ^{12}C ion pencil beam simulation.

Up to 400 MeV of protons are registered in figure 5.14 and from figure 15.15 a two dimensional representation of the tracking of protons during particle transport, protons are drifted in the forward direction of the primary beam with less deviation from the primary beam direction. Figure 15.16 plots the angular distribution of protons in radians. The angle used for this study is that made between the primary ^{12}C pencil beam direction and the direction of the emitted proton and from the histogram, a high count of protons is recorded for those leaving the target volume through an angle less than 45^0 an equivalent to 1 radian. No proton is reportedly presented to leave the soft tissue cube volume at orthogonal angles and beyond. Less deviation of protons from the main proton beam is attributed to highly energetic ^{12}C beam that overcomes the strong coulombic repulsion forces at close range distances between ^{12}C beam protons and soft tissue atomic protons that very less protons are deflected off the incident primary particle path at large angles.

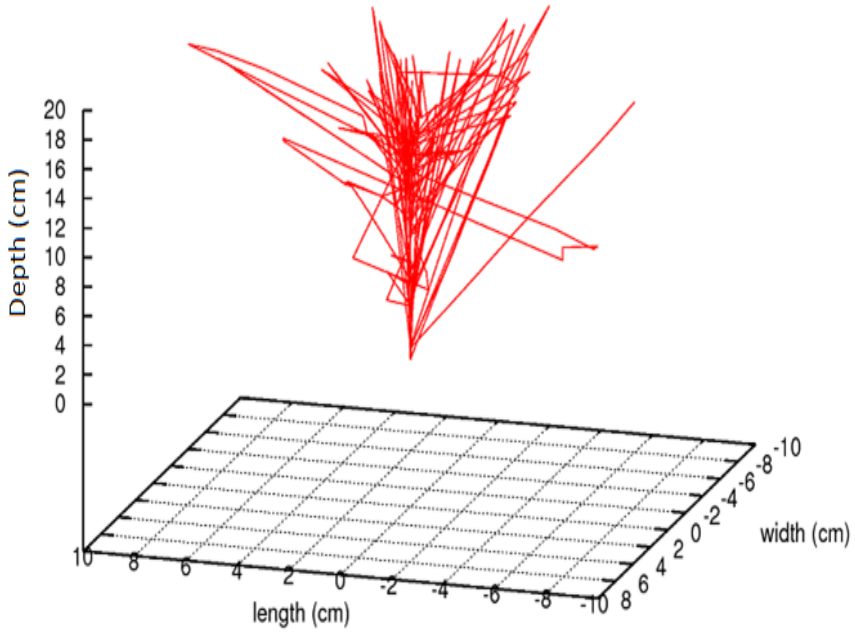

Figure 15.15: 3D view of propagation of protons with respect to the primary beam direction during a 300 MeV/u carbon ion simulation

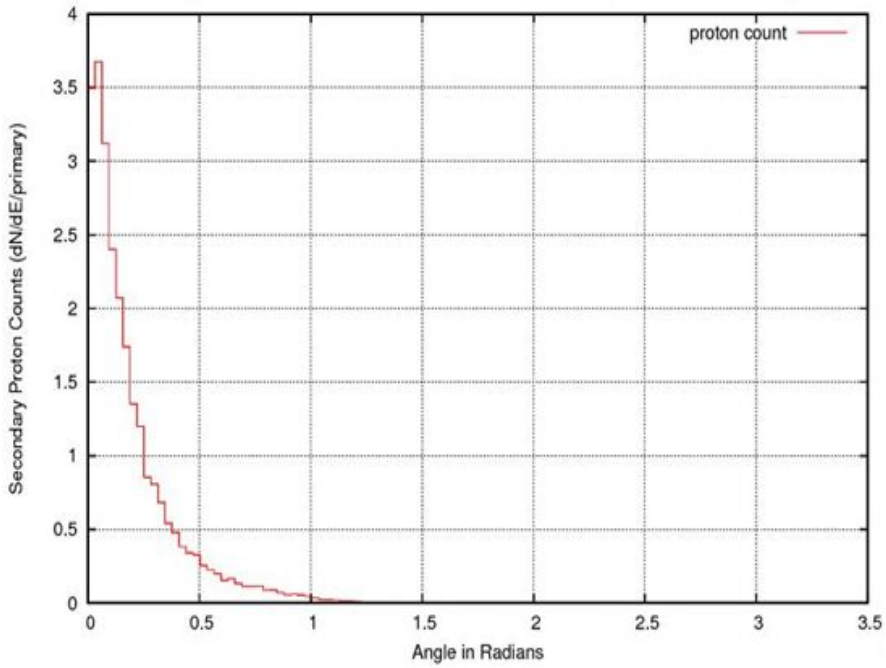

Figure 15.16: Angular distribution of protons in the 300 MeV/u carbon ion simulation.

Angular distribution of prompt gamma radiation during the 300 MeV/u carbon ion irradiation of the soft tissue sample has also been considered during the simulation. The results of the angular distribution are recorded in radians as in figure 5.17 ranging from $0\ ^{0}$ to $180\ ^{0}$, a correspondence in degrees. The angle between the primary carbon ion beam direction and the prompt gamma direction is used for this study and from the plot, gammas are emitted

isotropically in all directions with slightly fewer counts at orthogonal angles to the main primary beam. More gamma counts are recorded for angles less than 0.5 rad an equivalent to 28.6^{0} indicating more prompt gammas were emitted in the forward direction of the primary carbon ion beam. This is attributed to the ability of the incident beam ions to cause forward inelastic nuclear interactions with the soft tissue nuclei. A progressive decline in the gamma count is noted as the angle increases beyond 0.5 radians to a minimum of orthogonality but later gamma count increases with angle increase, a clear difference of prompt gamma distribution from a simulation of 160 MeV proton beam, figure 5.18 in which their count suffers a minimum depression at 0.7 rads an equivalent to 40^{0} from a slow rise for angles less than 40^{0} but beyond the depression in gamma count, a progressive increment in gammas recorded with rise in angles reaching the maximum at 180^{0}. This is because protons are of light mass as compared to ^{12}C ions that they are easily scattered of their main path especially at low energies and inelastic nuclear interactions in the proton beam simulation are not forward directed as in carbon ion simulations. A slightly low gamma count is still evident at 1.571 radians showing very few gamma radiation being emitted at exactly 90^{0} off the incoming beam path.

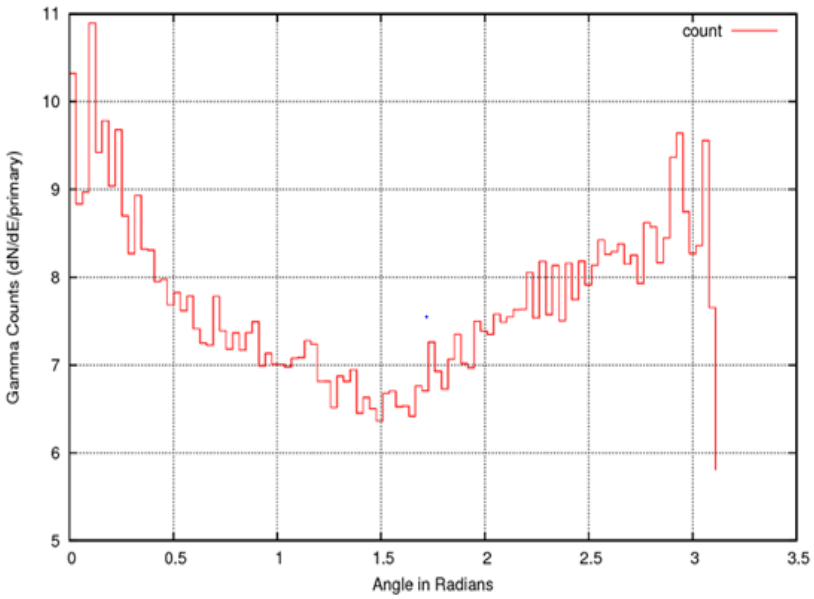

Figure 5.17 Angular prompt gamma distribution in 300 MeV/u ^{12}C ion simulation.

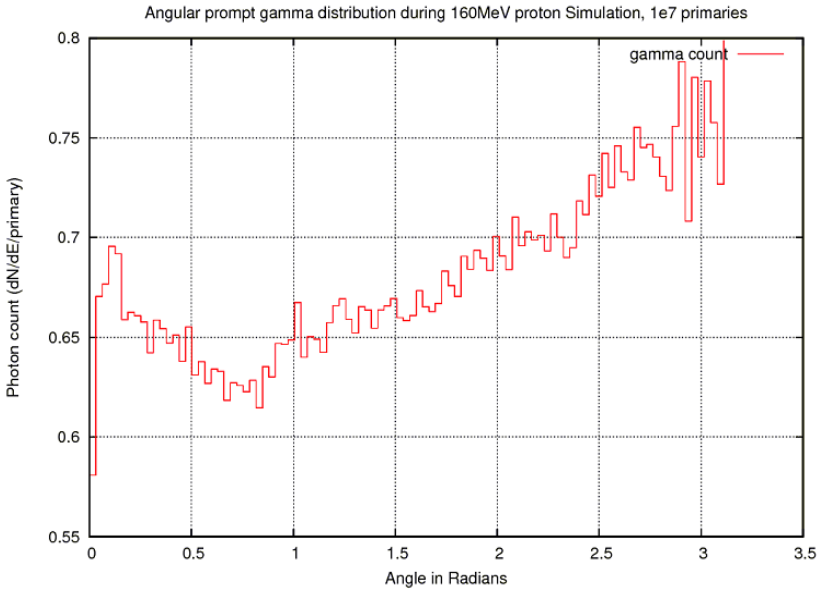

Figure 5.18 Angular prompt gamma distribution in 160 MeV Proton beam simulation

5.4 Fluka estimator error

Estimators for scoring particle quantities in Fluka are associated with errors when used in a simulation. For example, the usrbdx estimator used in these simulations to score angular distribution of protons and photons had a statistical error. Such an error was a measure of how the scored angular parameters deviated from the calculated average value obtained from 5 cycles of a simulation run. The Monte Carlo package calculated this error as 7.5% which is generally reliable and within acceptable limits from the Fluka manual since it is less than 10%. The statistical error in connection to the usrbin estimator for scoring dose deposition of the primary beam was negligible in both 160 MeV proton beam and 300 MeV/u carbon ion beam simulations because a large number of 10^7 primaries was run in these simulations with detector binning width of 1 mm in the 20 cm detector length.

6 Photon imaging detectors

In this chapter, studies have been performed on photon imaging cameras such as pin hole collimated camera, HPGe Compton camera and single scattering Compton camera, photon emission by energy selection and time of flight studies for both photons and neutrons. An iterative computer algorithm for reconstruction of Compton cones from energy deposition of photons has been implemented in this chapter to have a close analysis on the production points of prompt gammas which are Compton scattered at their first interaction and finally photo-absorbed using the two Compton cameras.

6.1 Pin hole camera

To monitor the origin of prompt gamma radiation emitted perpendicular to the primary proton beam as a result of nuclei de-excitation along the beam, a collimated camera consisting of 42 strips of lead each of thickness 0.4 mm separated by 0.1 mm breadth of parallel holes of depth 8 cm placed 20 cm away from the top of the soft tissue cubic volume is used for this study, figure 6.1. Lead collimator is preferred for shielding of emitted gamma radiation because of its high atomic number that favours high photoelectric effect cross section thus greatly absorbing and reducing intensity of scattered photons not orthogonal to the primary pencil beam direction. A gamma sensitive volume detector of thickness 2 cm made of Silicon was placed 1 cm away from the lead collimator to register collimated prompt gamma radiation. Only prompt gamma radiation perpendicular to incident beam direction and parallel through the septa holes reaches the sensitive detector volume as illustrated in figure 23. And to analyse the distribution of photons before they are collimated by the lead septa, another sensitive volume using the Fluka estimator, USRBIN was placed in between the soft tissue phantom and the collimator 4 cm away from the top of the cube with dimensions 30cmx2cmx40cm to study the fluence and distribution of prompt gammas before any collimation is done.

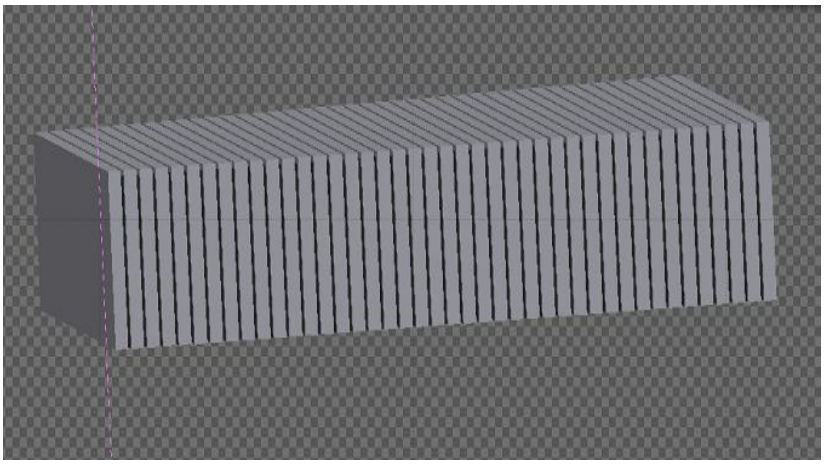

Figure 6.1: Pin hole Camera collimator used in 160 MeV proton beam simulation and made up of 42 strips of Lead with thickness of 0.4 mm separated by holes of 0.1 mm. The Collimator thickness is 8 cm and the image is extracted from Flair Geometry viewer.

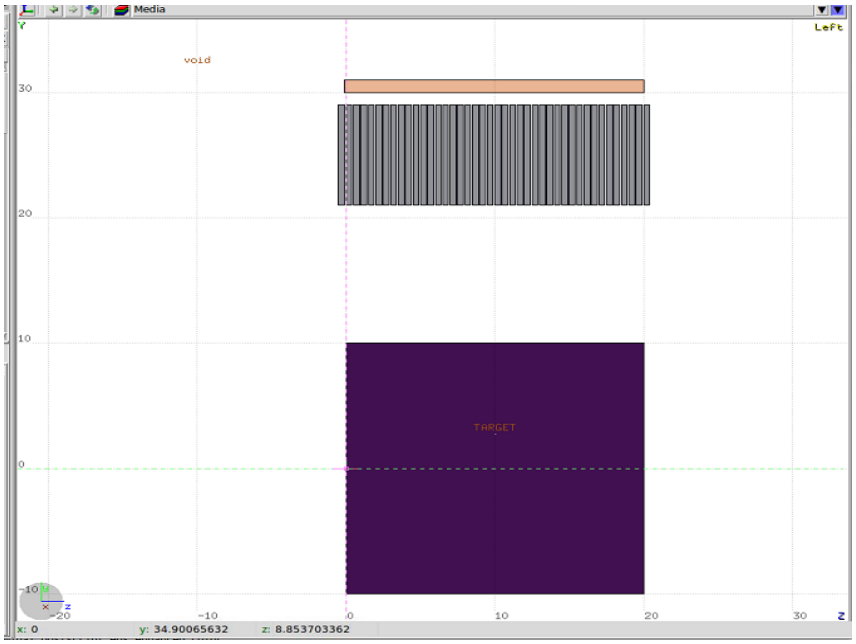

Figure 6.2: Simulation set-up of 160 MeV proton beam irradiance on a soft tissue phantom which emits photons detected by a Lead collimator camera by virtual of their position of origin.

A 160 MeV proton beam of the same configuration as mentioned earlier-on in the result section of this project was projected into the soft tissue phantom and gamma radiation was emitted isotropically throughout the target volume. This is due to unevenly randomized distribution of prompt gammas in terms of emission direction as illustrated in figure 6.3. From this plot, the soft tissue cube depth is positioned from 0 cm to 20 cm in the z-direction of the primary beam and it is evident that most of the photons emitted can be detected perpendicular to the primary beam for on-line imaging using prompt gamma radiation and to the extremes of 10 cm in length included at both forward and backward z-directions of the cube, a few photons are registered. This shows how the photons are unevenly distributed in all directions before being collimated through the pin hole lead camera.

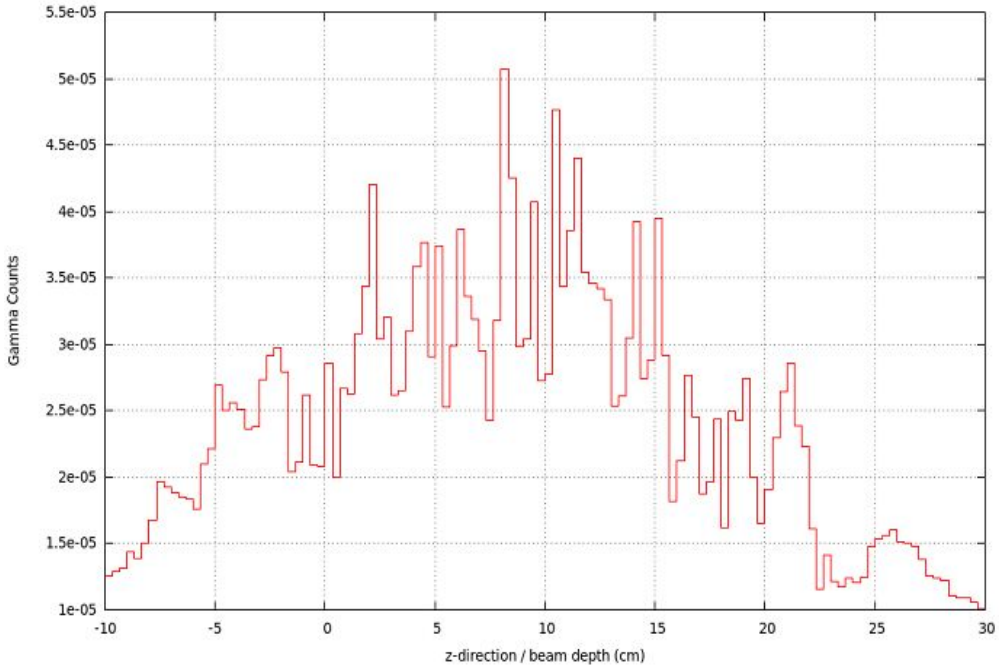

Figure 6.2: Distribution of photons with respect to soft tissue cube depth detected before collimation, by a sensitive volume placed 4 cm to the top of the cube during a 160 MeV proton beam simulation.

Only gamma radiation parallel to the lead holes are allowed to reach the sensitive detector made up of silicon. Gamma radiation emanating at other angles and not perpendicular to the beam direction was photo-absorbed in the lead septa under photoelectric effect and the plot of gamma count recorded after collimation in the beam depth direction (z-direction) has been given a binning of 0.1 mm for each bin, a correlation to the septa holes used.

Considering the count of prompt gamma radiation with pencil beam 160 MeV proton depth, the count of gamma radiation normalized to the primaries progressively increases on average with beam depth into the target soft tissue volume with a highest gamma count on average recorded at about 14 cm depth, 2 cm length before the Bragg peak expected region at 16 cm proton beam range, illustrated in figure 6.4. Further counts of gammas are registered beyond 16 cm beam depth with a decrease in counts as these are a contribution from inelastic secondary neutron nuclei interactions. Capturing of the secondary thermal neutrons explains the decrease in these neutron induced interactions thus a decrease in gamma count.

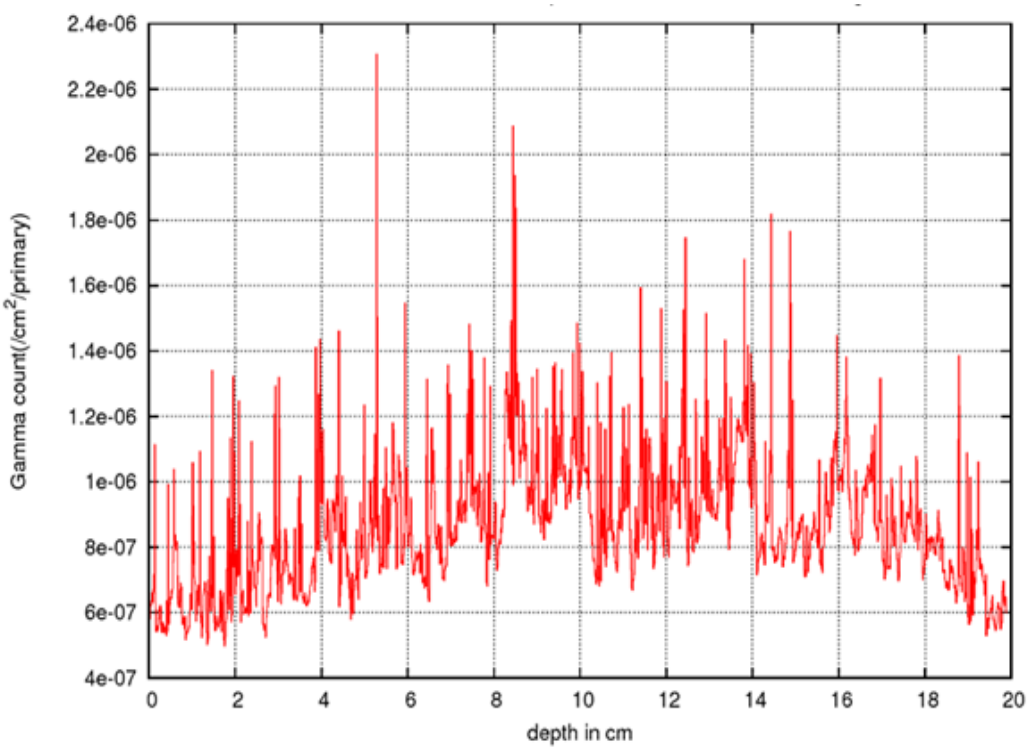

Figure 6.4: Distribution of prompt gammas along the 160 MeV beam trajectory

However due to a wide energy range from a few keV to over 10 MeV of prompt gamma radiation emitted and limited field of view of the camera due to mechanical collimator usage, the results of the simulated Gamma camera with lead collimators produces prompt gamma depth profile which doesn't clearly show the incident primary beam range and Bragg peak position since it is subject to errors, leading to inappropriate determination of maximum dose deposition. Sources of errors may include total photon absorption of perpendicular gamma rays directly to the septa width of 0.4 mm which can not be detected by the detector placed 2 cm above the collimator, very large energy range of emitted photons that the sensitivity of the simulated gamma camera is low and finally Compton scattering of photons within the soft tissue volume that after the scattering event, the scattered photons are parallel to the collimator holes.

To reduce on such undesirable events, tracking of prompt gamma radiation by virtual of their original position of production with out any form of mechanical collimation has been simulated with 10^7 primaries of a 160 MeV proton beam for all photons coming out of the soft tissue volume. The registered count of prompt gammas emitted due to atomic nuclei de-excitation with respect to the primary beam trajectory in figure 6.5 shows that in both x and y dimensional view of the soft tissue cube, 95% of the gammas have their origin exactly within the 0.1 mm FWHM at the primary proton beam path positioned at (0,0) coordinates of the cube where almost all nuclear interactions of the proton beam occur with the soft tissue nuclei and the rest of 5% laying off the 0.1mm especially in the Bragg peak region in which the incident proton beam broadens.

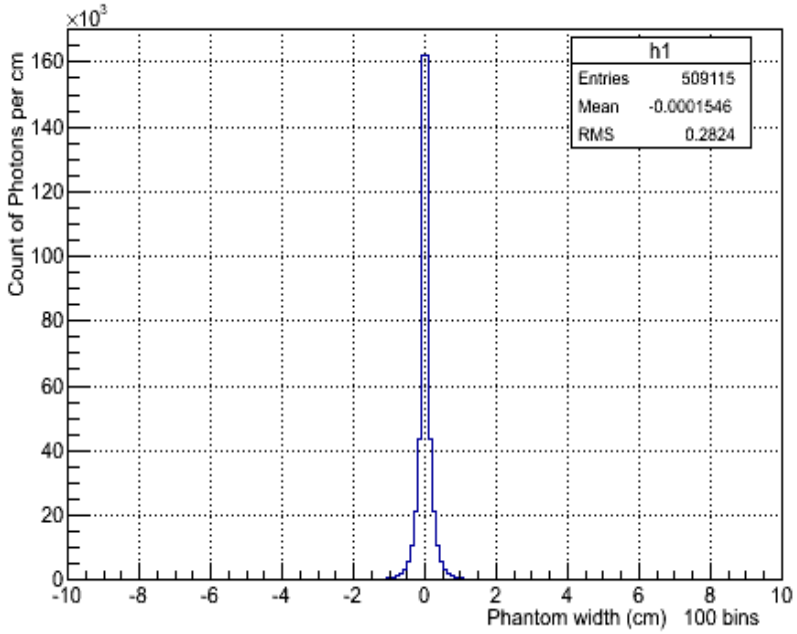

Figure 6.5: X and Y dimensional view of origin of prompt gamma radiation in a 160 MeV proton beam simulation of 10^7 primary particles.

The origin of prompt gamma radiation with respect to the primary beam direction has been investigated in figure 6.6 that with no doubt illustrates the increment in the gamma count as the primary proton beam traverses the soft tissue cube depth. From the Bethe Bloch prediction, increase in energy loss of the primary beam occurs as the charged protons slow down in the target volume raising the number of nuclear interactions that occur per unit of penetration depth moved. This leads to increased production of prompt gammas till a depth of 15.8 cm is reached by the primary incident beam about 0.2cm from the Bragg peak position of maximum energy loss and dose deposition. Beyond 14.8 cm depth, a sharp fall off of the gamma count is registered.

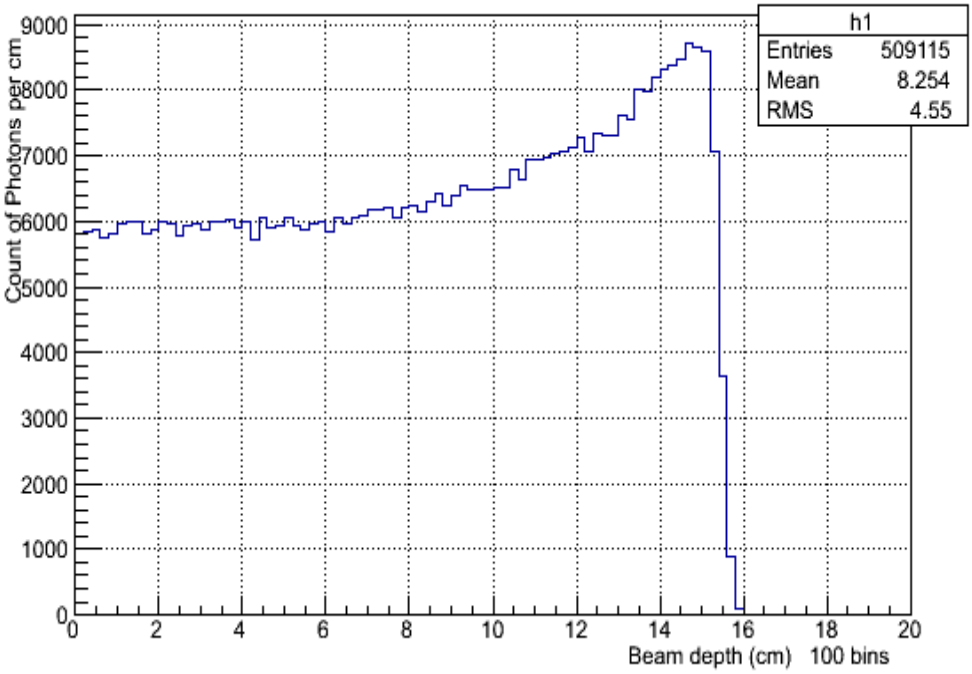

Figure 6.6: Prompt gamma count with respect to penetration depth of the 160 MeV proton beam of 10^7 primary particles. The distribution of the photons closely correlates with the inelastic nuclear interaction yield in figure 5.6, [7].

6.2 Prompt gamma emission by energy selection

The prompt gamma energy spectrum obtained as a result of 160 MeV proton pencil beam irradiance to a soft tissue phantom in figure 5.8 clearly illustrates the distinct dominant gamma peaks at energies of 2.2 MeV, 4.4 MeV, 5.2 MeV and 6.1 to 6.8 MeV in the energy spectrum. A study on the emission of prompt gammas with energy interval selection has been included in this project to closely analyse the gamma yield of specific soft tissue nuclei with respect to the incident proton beam depth. Energy ranges of 0-2 MeV, 2-4 MeV,4-5 MeV, 5-6 MeV and 6-20 MeV have been chosen for this particular study and these have been applied to the detected gamma counts relative to their initial production positions along the primary proton beam trajectory. For all the five energy intervals studied on photon yield, their prompt gamma-ray emission yields show a distinctive correlation with the depth-dose curve which has its maximum dose deposition at a dose-depth curve which has its maximum dose deposition at a depth range of 16 cm but all exhibit few gamma counts beyond the primary proton beam maximum range and a sharp distal fall off at 15.8 cm before the Bragg peak position.

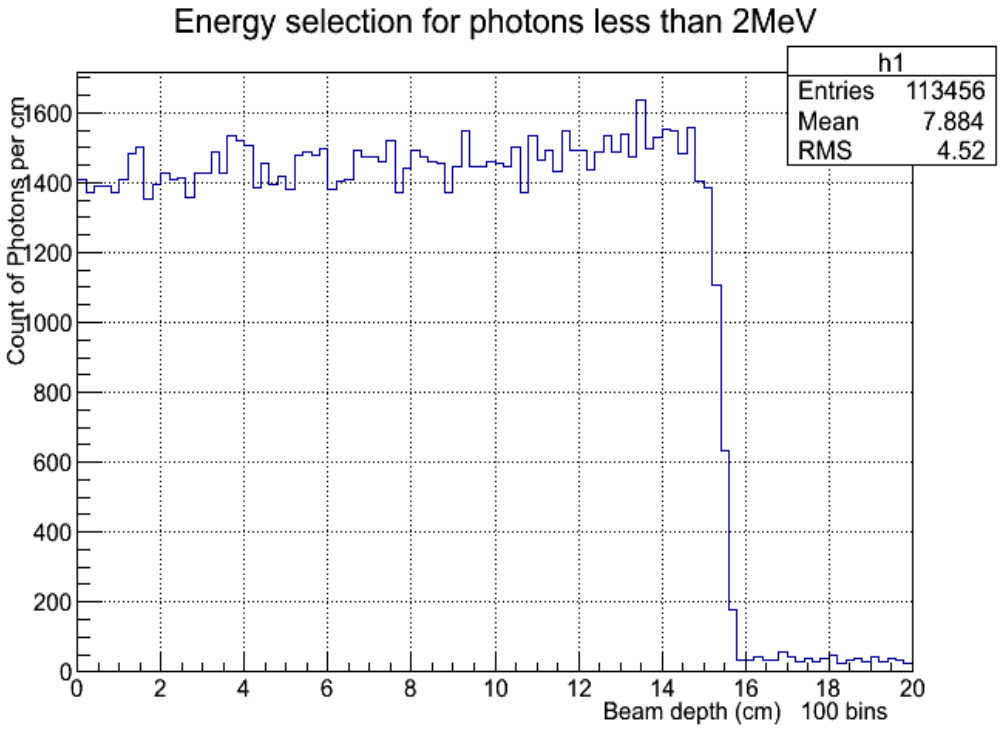

Figure 6.7: Prompt gamma count with respect to penetration depth of the 160 MeV proton beam of 10^7 primary particles with an energy selection interval of 0-2 MeV applied to detected gamma counts.

The prompt gamma emission yield of 0-2 MeV, figure 6.7, shows a low gamma count of an average of 1400 gammas/cm throughout the beam trajectory as this is a contribution from the few produced gamma rays from PET isotopes and neutron induced gamma. The gamma spectrum with energy between 2-4 MeV (figure 6.8) illustrates a gradually increment in photon production with respect to the primary beam depth attributed to increased de-excitation of excited ^{14}N nuclei. A high gamma count of 2-4 MeV energy range is recorded since more prompt gammas are produced from de-exciting ^{14}N nuclei than the PET isotopes which even undergo washout during patient treatment procedures in clinical set-ups.

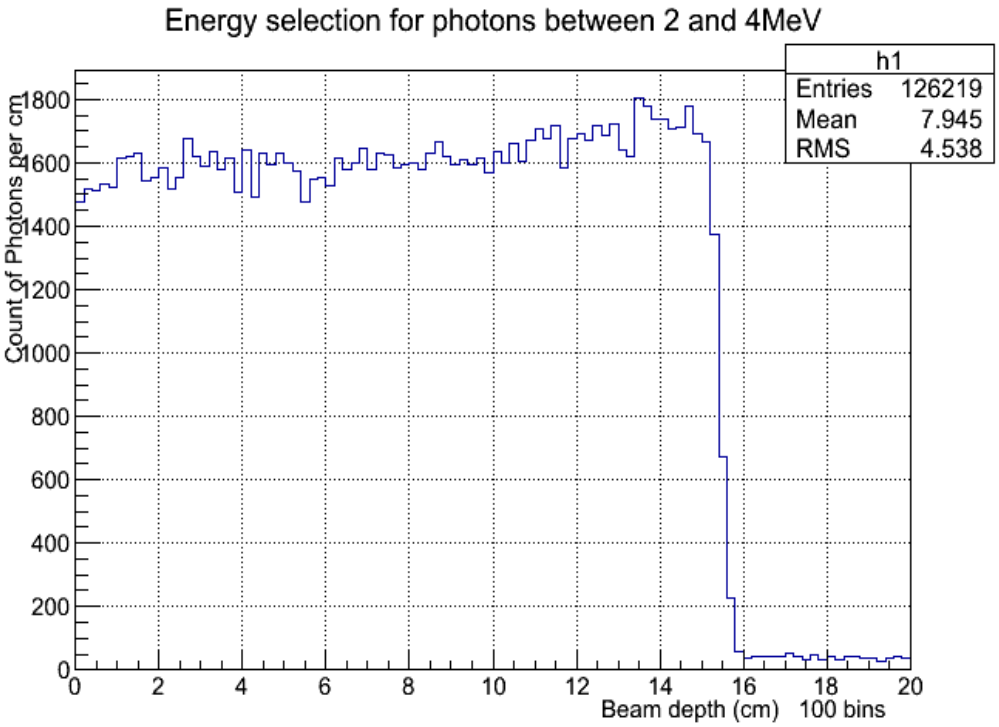

Figure 6.8: Prompt gamma count with respect to penetration depth of the 160 MeV proton beam of 10^7particles with an energy selection interval of 2-4 MeV applied to detected gamma counts.

Prompt gamma photons emitted with an energy range between 4 MeV and 5 MeV exhibits a unique feature of increasingly high photons produced along the primary beam path with a maximum of 2600 photon counts/cm at a penetration depth of 15.8 cm near the end of the proton range, figure 6.9. This is due to increased nuclear inelastic interaction of the primary proton beam, especially at the last few centimetres before its maximum range, with widely abundant ^{16}O atoms producing as a result secondary protons, an alpha particle and excited ^{12}C nuclei. The ^{12}C nuclei in their meta-stable states decay by distinct energy of 4.4 MeV and the energy range of prompt gammas (4-5 MeV) gives a better signal during on-line ion beam range monitoring when using prompt gamma radiation since high photon counts are recorded. Thus this increases the image quality of gamma initial position through improved sensitivity and efficiency of the detecting equipment used during hadron therapy treatment procedures.

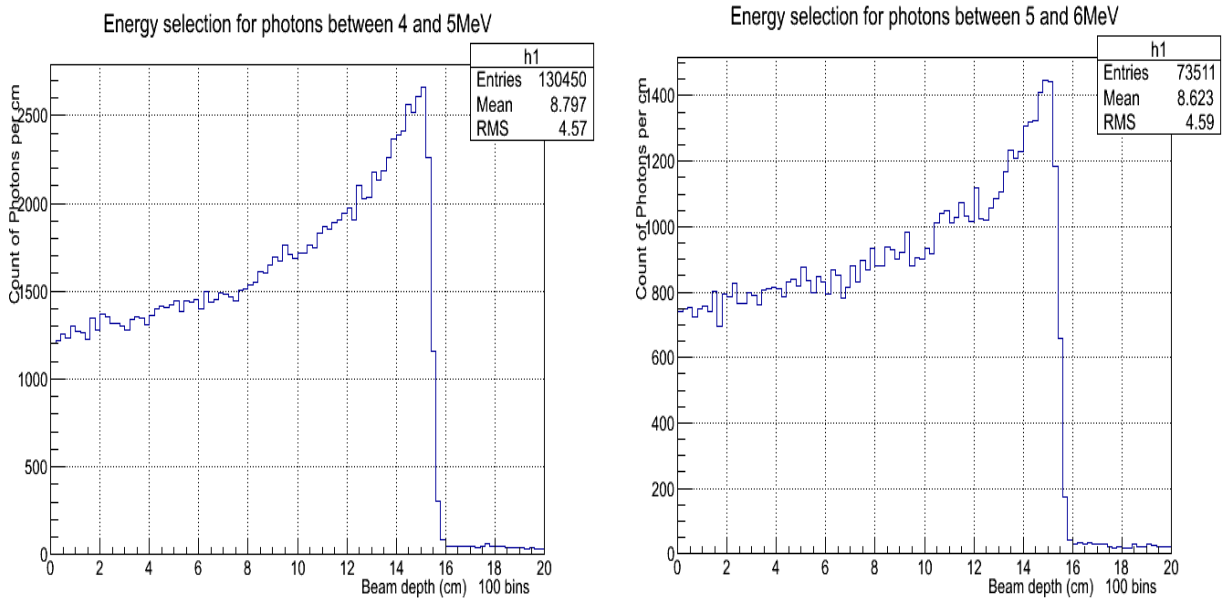

Figure 6.9: Prompt gamma count with respect to penetration depth of the 160 MeV proton beam of 10^7particles with an energy selection interval of 4-5 MeV applied to detected gamma counts. More gamma counts are recorded in this energy range and the same photon distribution exactly applies to photons of energy 5-6 MeV arising due to decay of excited ^{14}N nuclei though with a lower maximum photon count.

Prompt gamma rays with an energy range between 6 MeV and 20 MeV have also been included in the study scope and they exhibit the same increasing characteristic of the photons though with a lower maximum photon count of 1700 counts /cm produced in form of a peak at a penetration depth between 15 cm and 16 cm near the end of the proton range shown in figure 6.10 with an exponential gamma count increase in the plateau region of the dose deposition curve till a depth of 15 cm. The prompt gamma maximum peaking is consistent with the cross sections of the nuclear transition of the excited ^{16}O produced from proton inelastic collisions with stable ^{16}O nuclei in the soft tissue which has its a maximum around the primary proton beam energy of 13 MeV [66] and leads to emission of high energetic gamma photons of energies above 6MeV.

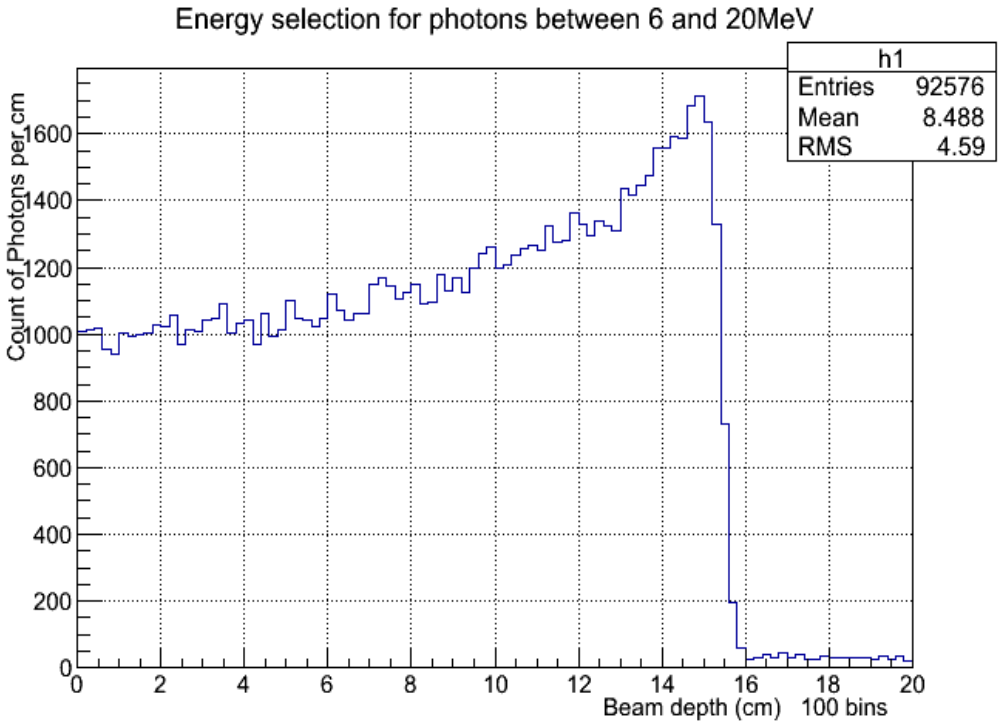

Figure 6.10: Prompt gamma count with respect to penetration depth of the 160 MeV proton beam of 10^7particles with an energy selection interval of 6-20 MeV applied to detected gamma counts. Maximum photon peak exhibited at 15 cm depth mark, 1 cm before the maximum dose deposition region at 16 cm.

6.3 Germanium block Compton camera

Semi conductor crystals preferred to gas ionization detectors are used currently for detecting highly energetic x-rays and gamma radiation due to their high density which enable ionizing radiation to deposit much of its energy in the semiconductor with relatively smaller dimensions than gaseous detector tubes. Commonly used semiconductor detectors include germanium crystals, silicon and diamond detectors. Electron-hole pairs are generated at ionization when the radiation deposits energy in the semiconductor depletion region and the electron hole pairs accelerated to opposite electrodes produce an electric pulse proportional to the energy deposition. Currently research on emission of prompt gamma radiation during radiotherapy just like in [67] has utilised the good features of germanium detectors to monitor treatment beam range and dose distribution in real time.

In this project a high purity block of germanium crystal initially placed 10 cm above the soft tissue cube of dimensions 30x10x30cm^3 in vacuum region figure 6.11, is chosen in preference to other semiconductors due to its good energy resolution. A consideration of the first two photon interaction events has been implemented in the order of Compton scattering as the initial energy deposition event with the second and last event as photo-electric effect which leads to total and complete energy absorption of the initially Compton scattered photon coming out of the soft tissue phantom. A 160 MeV proton pencil beam of FWHM 0.1 mm with a lateral Gaussian distribution has been used to investigate the type of particles reaching the detector region and time of flight for both prompt gamma radiation and neutrons has been analysed to investigate the time difference of arrival to the detector for both radiations. Though in reality, for Compton cameras of such a setting with out a hodoscope, timing of the incident primary beam particles becomes realistically impossible to achieve as a single detector piece at one side of the phantom is only used which isn't the case for PET scanner detection systems.

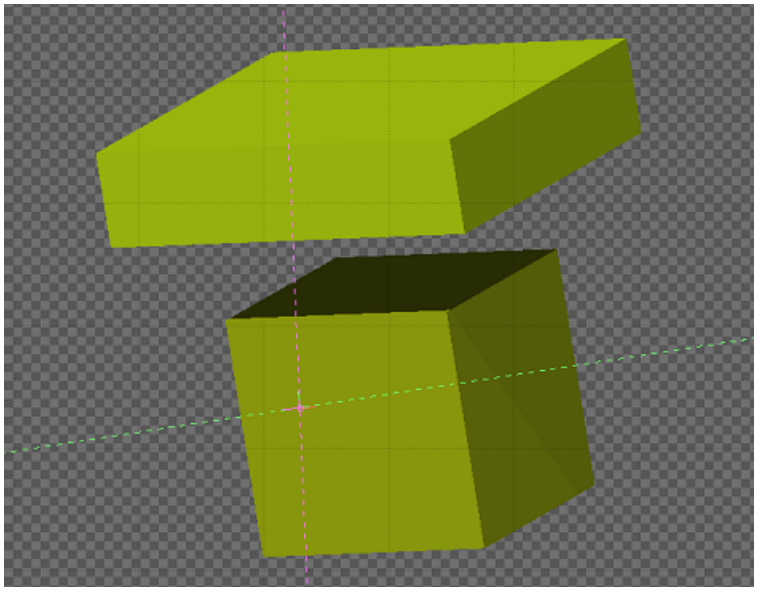

Figure 6.11: Diagrammatic representation of the simulation set-up with a HPGe Compton cone (**top**) for Compton cone reconstruction. **Bottom** is the soft tissue phantom.

During a 160 MeV proton beam simulation, type of secondary radiation reaching the germanium detector has been recorded and from figure 6.12, a high percentage yield of 66% for photons dominates all other secondary radiation so as to produce imaging signal for the germanium block Compton camera. 4-helium, 3-helium, trition and deuteron particles produced with in the soft tissue phantom never reach the detector as they are of high mass and interact within the soft tissue sample not escaping the phantom. Hard inelastic collision products of electrons and pair production products of electrons and positron produced from high energetic photons, reach the germanium region as well since it is surrounded by vacuum that positrons produced near the soft tissue phantom surface escape to the detector region as well as highly energetic electrons. Some electrons reaching the germanium crystal block, are produced as a result of delta rays being completely absorbed by inner atomic electrons, Auger electrons that gain sufficient energy above their ionisation energy to escape away from their atoms. A percentage of 1% for secondary protons is recorded making hits in the germanium region since the detector is placed perpendicular to the primary beam direction. So most proton particles escape without being detected since they are emitted at very narrow angles to the primary incident 160 MeV proton beam. However as expected, neutrons with a percentage yield of 18% from nuclear interactions within the phantom will penetrate the soft tissue sample to the detector making a significant noise contribution which is undesirable in germanium Compton camera.

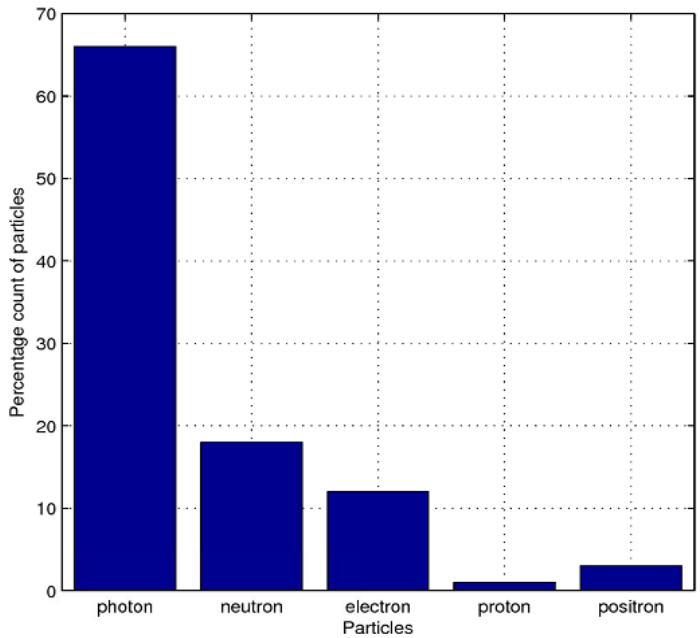

Figure 6.12: Count of secondary radiation reaching the germanium detector during a 160 MeV proton pencil beam simulation.

6.3.1 Time of flight for neutrons and photons

Time of flight technique for both prompt gamma photons and secondary neutrons is being used today clinically as a tool to suppress the noise contribution from fast neutrons reaching the detector especially if primary particles are initially time tagged or if two opposite photons can be detected by cyclic detectors as applied in PET scanners. In this simulation, a study

of the total time taken between when the incident proton primary particles are produced and directed 5 cm before reaching the soft tissue phantom and when the secondary radiation reaches the germanium detector has been carried out for photons and neutrons. Figure 6.13 (left diagram) shows the prompt gamma time of flight spectrum with majority of the photons on average reaching the germanium detector after 1.8 ns. A few counts of photons have their time of flight greater than 1.8 ns because they are neutron induced photons produced when secondary neutrons travel short distances off the incident primary beam trajectory and undergo inelastic nuclear interactions to produce excited nuclei.

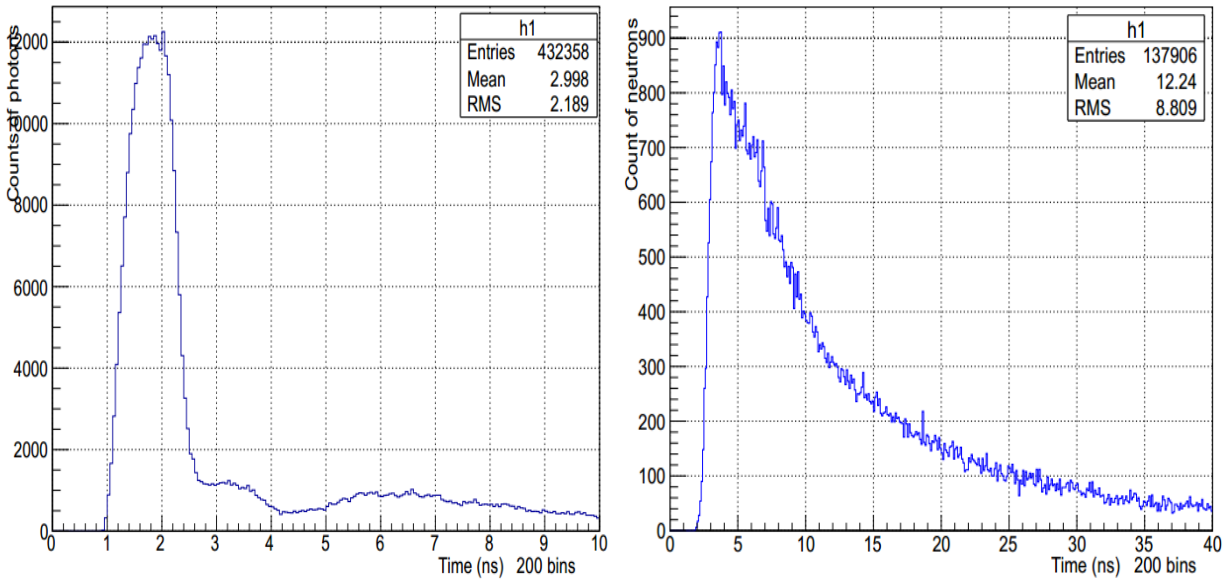

Figure 6.13: Time of flight spectra for prompt gamma photons (**left**) and neutrons (**right**) during a 160 MeV proton beam simulation.

Neutron time of flight spectrum obtained from the 160 MeV proton beam simulation displays a dominant sharp peak at 3.8 ns which is almost twice the time of flight of prompt gammas in the same simulation. An exponential decrease in counts of neutrons reaching the germanium detector region is shown in figure 6.13 (right diagram) which is due to low energy neutrons that are detected with slightly a longer time since they undergo multiple scattering processes within the phantom by interacting with soft tissue nuclei before emanating out of the phantom. The very distinct separation in time of flight for photons and neutrons as 1.8 ns and 3.8 ns respectively is the key aspect in the time of flight technique to eliminate noise contribution from detected neutrons. However for the use of Compton camera to image photon production distribution in patients, the time of flight technique comes with hardships to implement since the timing information of primary particles before interacting with soft tissue is practically difficult to achieve though the time of secondary radiation arrival to a scatterer detector can be easily recorded.

6.3.2 Optimization of HPGE detector performance

The HPGe Compton camera has been optimized in geometry for better performance and detection of gamma radiation by placing it in the vacuum 8 cm to the top of a 20cmx20cmx20cm

soft tissue phantom. The thickness of the HPGe crystal is 8 cm and it has an extension of 6 cm off the phantom vertical plane to take into account the widely scattered photons from the phantom. This maximizes both Compton scattering and photoelectric effect processes for better detection efficiency. The dimension of the crystal is 32cmx8cmx32cm placed at 90^0 to the incident beam direction.

6.3.3 Energy resolution of germanium block Compton camera

Energy resolution is expressed as a ratio of FWHM of a given energy peak in an energy spectrum to a particular photon energy. High purity germanium crystal block was chosen as a detector material for this Compton camera over other semiconductors such as silicon due to its fine energy resolution of 2 keV at 1 MeV (0.2%). This enhances the Compton camera detection ability to clearly distinguish between any two near by photo peaks in the energy spectrum. Figure 6.14 shows the energy spectrum of prompt gammas that were detected by the HPGe Compton camera with peaks at 0.2 MeV, 0.511 MeV, 2.3 MeV, 4.4 MeV and 5.2 MeV.

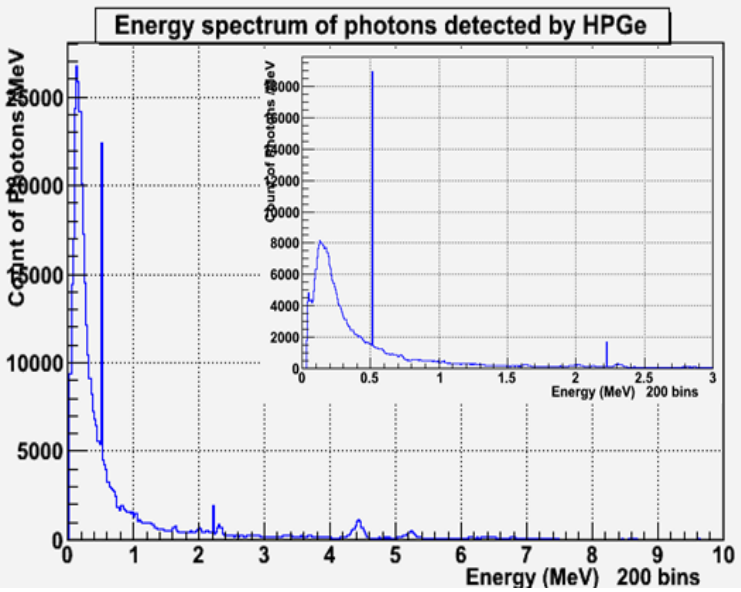

Figure 6.14: Energy spectrum of photons detected by HPGe crystal during a 160 MeV proton beam simulation.

6.3.4 Compton cone reconstruction algorithm

To locate accurately where the incident prompt gamma ray coming out of the soft tissue phantom is located before the first two successively interaction events in the germanium detector using Compton cone reconstruction, a computational algorithm is required to image either 2D or 3D gamma position distribution within the phantom which always lies on the surface of a reconstructed cone or its base circle. Such reconstruction algorithms can be either analytic or iterative in the way they handle generated data from experimental and clinical procedures such as in PET and SPECT or from simulated data as for this study case. In the past few years, Singh, a pioneer in Compton camera imaging presented in

articles of [68] and [69] a series of Compton camera imaging reconstruction methods for locating gamma source distribution mainly concerned with numerical methods like Maximum Likelihood Expectation maximization (ML-EM) and Algebraic Reconstruction Technique (ART). These measures are being put to practice even today in clinical setting for gamma ray detection and image acquisition with of recent developments such as Simultaneous Algebraic Reconstruction Technique (SART) for ART.

6.3.5 The Maximum Likelihood Expectation Maximization Algorithm (ML-EM)

The maximum likelihood maximization algorithm is one of the iterative image reconstruction algorithms widely used in both positron emission tomography and single photon emission tomography for precise location for gamma position of origin. The algorithm is only valid for data that is in a Poison distribution and it aims at computing the most likely distribution of an event from the measured data sample. In spite of data best fit for this algorithm being in a Poison distribution, the technique is also feasible with processed log-converted transmission sinograms that do not meet the Poison distribution requirement however much sometimes it may lead to suboptimal results like streak artifacts appearances in images. Correction techniques of Noise Equivalent Counts (NEC) scaling and NEC-shifting have been studied in [70] to transform arbitrary sinogram noise into noise which is approximately poison distributed so as to apply ML-EM algorithm for image reconstruction.

6.3.6 Algebraic Reconstruction Technique [ART]

This is an iterative algorithm first founded by Gordon, Bender and Herman in 1970's for use in computed tomography to reconstruct images from a series of angular projections in form of a sinogram. This technique solves a system of linear equations with image processing described in a matrix form, however due to lack of speed and accuracy in image reconstruction in the field of medical application, a faster algorithm known as Simultaneous Algebraic Reconstruction Technique (SART) was proposed in 1984 as a major refinement of the ART. Since then, the SART remains a powerful tool for iterative reconstruction. [71].

From [72], the two iterative algorithms require binning of the data obtained from measurements and from dimensionality of the measurement space which is not an optimal approach. Instead, event-based reconstruction techniques which avoided binning, at least in some coordinates, were proposed and from this concept, a general list-mode maximum likelihood estimation algorithm suggested by [72], which was well-suited to both the dimensionality and to the measurement errors in the Compton scatter measurement space was implemented. Further more, the geometry of Compton camera image is abit complex thus from [73], image reconstruction is quite difficult with techniques such as filtered back projection and MLEM. Another quicker reconstruction algorithm known as Stochastic Origin Ensemble Approach (SOEA) was proposed from Markov chains which involved comparison of event density of prompt gammas in a particular location to the rest and if it was higher than the surrounding events, it was taken as the position of gamma origin.

Analytic algorithms which show high speed performance and based on Fourier transform, filtered back projection or Abel transforms have also been proposed to solve the 3D gamma source reconstruction rather than numeric solutions as suggested previously, and in such analytic methods, two distinct steps are performed. [72] suggests an analytic method which limits measurement errors varying from occurrence of event to event with multiple scattering events within the detector crystal in which the first step involves spherical harmonics being used to recover cone-beams from cone-surface projections. Then deconvolution in spherical coordinates is used to obtain a filtered back-projection technique which generates the cone-beam projections directly from the Compton scattered data. To compute the cone surface projection which corresponds to the 3D source distribution from cone-beam projections, reconstruction algorithms such as radon inversion methods are implemented to locate precisely the point of emission of prompt gamma rays within the target volume. Nevertheless, analytic imaging algorithms need noiseless data which is unusual in statistic and physics models. But arithmetic algorithms can precisely incorporate with such models since they work well in noisy data.

In this study, an iterative and numeric algorithm which is an inversion method in nature has being used to locate in 2D the position of gamma quanta which lies on the conical surface or base cone circle after being Compton scattered once in the germanium detector and second interaction as photoelectric effect. The computational algorithm has been written in two high level programming language platforms with an aim of having reduced data computational times and fast Compton cone base surface reconstruction. The programming languages used include; Fortran77, which is a programming language in which Fluka is written in and C++ programming language which has imperative, object-oriented and generic programming features used in this case for fast reconstruction of circular cone surfaces. Data analysis has been handled by two numerical analysis packages and these include ROOT, an object oriented large data handling frame work first developed at CERN for the NA49 experiment written in C++ programming language for scientists and it can analyse data capacity from a few bytes to Terabytes using a C++ interpreter called CINT created by Masa Goto in Japan [74]. The second numerical analysis package is Matlab known as Matrix Laboratory which is an environment for numerical computation, visualization and programming. MATLAB is used for a wide range of applications, including signal processing and communications, image and video processing, control systems, tests and measurements in several areas, such as psychology, medical physics, computational finance and biology [53].

The Compton cone reconstruction algorithm was generally implemented in three steps in order to produce results of photon location by their initial points of production along the circumference of the cone base circles. The first step involved modification of Flair Fluka package through the mgraw.f file which helps the user to access all properties of secondary particles produced after any nuclear interaction event. This file was edited to obtain numeric data in form of 3 Dimensional gamma location data and energy deposition data for interaction events such as nuclear inelastic event in the target volume, Compton scattering of prompt gammas and photon absorption in the detector. Tracking of prompt gamma photons from the soft tissue phantom through the two successive photon interaction processes in the germanium detector was performed with aid of user spare variables offered by Fluka in

the common block scripts of TRACKR including the stupre.f and sturf.f user routines which help in inheriting previous particle history. Stuprf is called before loading into stack hadrons, muons, neutrinos and low-energy neutrons whileas Stupre is called before loading into stack electrons, positrons and photons. This has been of great use for our case of prompt gamma photon interaction in the detector.

The second step involved the use of a Fortran77 script that utilized the extracted file from the previous fluka run to compute a Compton scatter angle for each prompt gamma photon through which it is scattered for each two Compton scattering and Photoelectric events using Compton scattering equation stated earlier in Chapter four equation (27). Each cone slanting length was calculated for reconstruction of 3 dimensional cones. The cone vertices or apexes were taken to lie on the Cartesian coordinate point of Compton scattering event with the cone axis produced by the two positions of Compton Scattering and Photoelectric effect points. Prior to the main beam information of positioning through the soft tissue phantom, the incident pencil beam is projected in the positive z-direction at a zero cm mark in the y-plane of the phantom geometry and the cone axis intersects this plane always at the y=0 cm mark. This assumption helped in calculating of the centre of the cone base circle for each cone. The radius of the base circle was calculated as a function of the Compton scatter angle using the cone slanting length, cone height or axis and energy deposition of a photon at Compton scattering and photoelectric effect points. This computational algorithm has been based on vector calculus of planes and vectors in euclidean geometry space.

The generated data file that contained centre of cone base circles with their corresponding radii was proceeded to step three in which a Root script was used to draw out cone base circles in the detector x-z plane for each data set and the script was incorporated to read out points of interaction of any two circles. Since the position of gamma production in the Compton camera kinematics is taken to be lying on the circumference of reconstructed cones that is by their base circles, intersection points of cone base circles especially those crossed by more than three cone base circles contain the precise location of where exactly prompt gamma photons were produced in the phantom and thus were read out by the C++ script. Such points of intersection were seen to be recorded more than thrice in the generated data files in order to confirm gamma emission locality and to eliminate noise from the collected data. Intersection points of cone base circles that appeared less than thrice were rejected since in actual sense they were never intersection points in the three dimension space but only viewed as intersection points in 2 Dimension geometry of x and z axes.

6.3.7 Algorithm results

A proton therapy beam of energy 160 MeV made up of $1x10^7$ primaries with exact properties as previously discussed earlier on in this chapter was run through the soft tissue phantom to study the distribution of prompt gamma by their points of initial emission or production in the phantom. Majority of the emission points lie within 1 cm length off the primary beam trajectory. For use of the Compton cone reconstruction algorithm, only emission points of photons that corresponded to successive Compton scatter and photoelectric effect in the germanium detector were considered. Figure 6.15 shows the 2D distribution of such points in the x-z phantom plane with much of the point distribution as expected are along the incident proton beam path till 15.8 cm depth. From the plot, photon emission points in the first 2 cm depth tend to align completely along the beam path and as the beam transverses through the phantom, they are scattered off the beam path since the incident proton beam particles lose energy and due to strong repulsive coloumbic force between the soft tissue atomic nuclei and positively charged incident protons, they are deviated off the main beam path causing nuclear excitation and gamma emission at distant regions away from the x=0 cm mark.

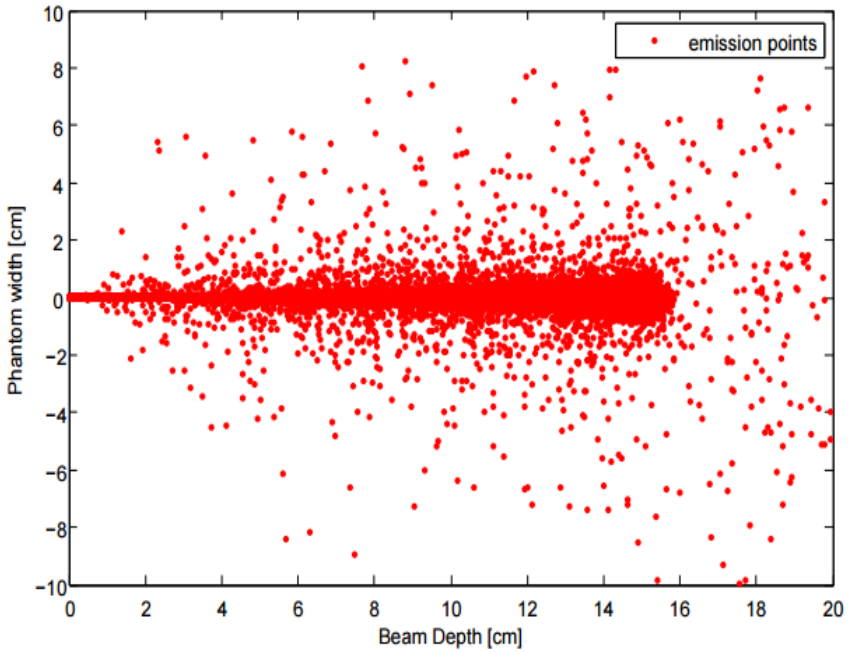

Figure 6.15: x-z (width-beam depth) phantom plane showing photon production points that corresponded to the first two interaction events in the germanium detector during the 160 MeV proton beam simulation.

Investigated earlier on in figure 5.8, the energy spectrum of prompt gammas leaving the phantom volume ranges from a few keV to 10 MeV however not all photons undergo their first two interaction events as Compton scattering and Photoelectric effect successively. It has been noticed from figure 6.16 that majority of photons with energies less than 1.6 MeV for 160 MeV proton beam simulation and 300 MeV/u carbon ion simulation undergo the successive two interactions as a few keV is deposited to the recoiling scatter electron and the rest of their energy deposited to the photo-electron. Most of the prompt gamma radiation

in the 160 MeV proton beam simulation have an average of 0.2 MeV so as to interact with the germanium crystal in the two processes while as for the 300 MeV/u carbon ion simulation, the dominance of such photons peaks at 0.18 MeV but with both simulations having a common second peak at 0.511 MeV corresponding to photons formed as a result of electron-positron annihilation in phantom. This has been discussed further in the next section of results under the crystal block Compton camera made up of germanium. Majority of prompt gamma undergo a variety of interaction events other than the case study required two events needed with most of them being multiple Compton scattered before being photon absorbed in the crystal due to their high energies. Other highly energetic photons never lose all their energies at energy deposition points in the germanium detector and as a result end up escaping the detector volume.

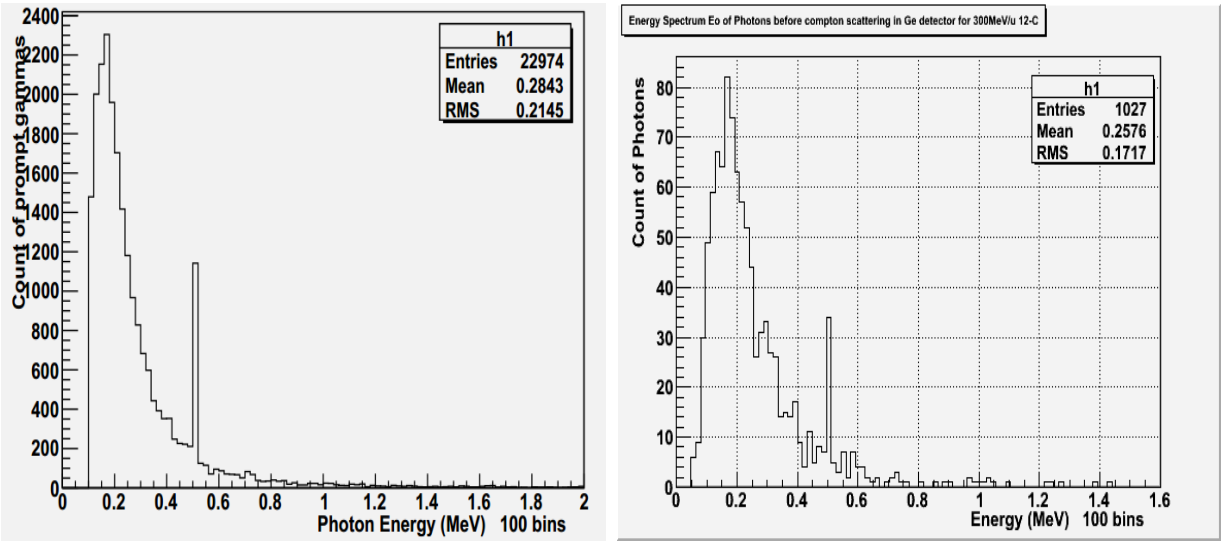

Figure 6.16: Energy spectrum of prompt gamma radiation that was first Compton scattered before having photoelectric effect as their final interaction event in the germanium crystal. To the **left**, results from 160 MeV proton beam simulation and to the **right** is the spectrum from 300 MeV/u carbon ion simulation.

Prompt gamma radiation Compton scattered at their first interaction event in the detector region in the 160 MeV proton beam simulation show a large variation of the Compton angle through which they are scattered off their initial path of propagation out of the soft tissue phantom. A higher count of prompt gamma rays is reported in figure 6.17 for photons scattered at angles greater than 90^0 which corresponds to photon energy of 0.2 MeV and below than those forwarded scattered in their path direction of scatter angles less than 90^0. The decrease in Compton scatter angle corresponds to the increasing count of high energy photons greater than 0.2 MeV and a count of 40 photons/MeV is recorded at angles less than 2^0. Such small angles are exhibited by a few photons of 1 MeV and above and some of 0.511 MeV photons which deposit less energy to Compton electrons thus scattered very less as shown in figure 6.17 (Right). The decreasing count of photons as the angle increases is explained by the few photons of energies less than 0.2 MeV being Compton scattered widely almost to a back scatter at 180^0 which would lead to the Compton edge.

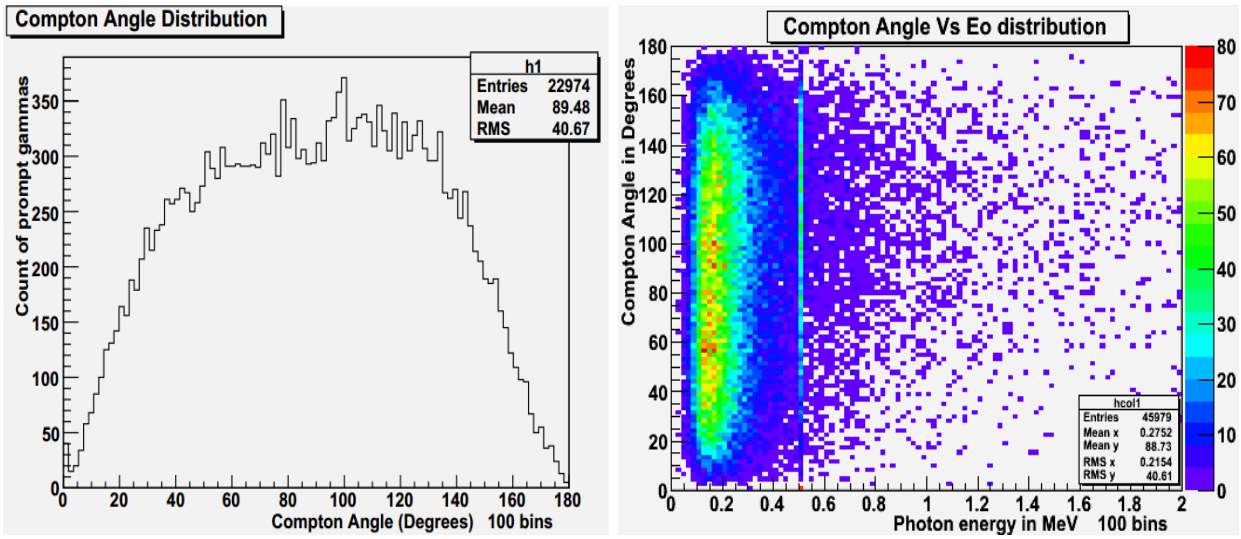

Figure 6.17: Distribution of Compton scatter angles of prompt gamma radiation in the energy range between 0.1 MeV and 1.8 MeV during a 160 MeV proton beam simulation.

6.3.8 Detection of 0.511 MeV prompt gammas

The energy spectrum of prompt gamma detected by the HPGE Compton camera in figure 6.16 before Compton scattering has exhibited a distinct photon peak at 0.511 MeV. This corresponds to the electron rest mass energy of 0.511 MeV/c^2 and such photons are formed as a result of positron-electron annihilation in the phantom. The incident proton or carbon ion beam of energy 160 MeV or 300 MeV/u respectively undergoes non elastic nuclear interactions with soft tissue nuclei that nuclear fragments, positron emitting in nature mostly ^{11}C, ^{13}N and ^{15}O, are formed and secondary particles such as protons, deuterons, tritons, alpha particles or photons are emitted as a result of formation of such positron emitters. The major six channels through which positron emitters are formed from widely abundant stable nuclides of ^{14}N, ^{16}O and ^{12}C in human soft tissue, despite the occurrence of other nuclear reactions, have been listed in Table 5.

Nuclear Reaction	Threshold Energy (MeV)	Half Life (min)	Positron Max. Energy (MeV)
^{16}O(p,pn)^{15}O	16.79	2.037	1.72
^{16}O(p,2p2n)^{13}N	5.66	9.965	1.19
^{14}N(p,pn)^{13}N	11.44	9.965	1.19
^{12}C(p,pn)^{11}C	20.61	20.39	0.96
^{14}N(p,2p2n)^{11}C	3.22	20.39	0.96
^{16}C(p,3p3n)^{11}C	27.50	20.39	0.96

Table 5: Summary of six major nuclear interactions that lead to formation of positron emitters in a proton beam simulation. Other nuclear interactions that lead to formation of the same positron emitters can be found in [75].

Just like photons of other energies emitted out of the soft tissue phantom, the 0.511 MeV photons deposit a significant amount of energy to the recoiling electron at Compton scattering in the germanium crystal block and from figure 6.18, photons deposit an average energy

of 0.33 MeV to the electrons with fewer photons depositing less energy than this average number, explaining the exponential rise in energy deposition from a few keV to a maximum energy value of 0.34 MeV. The plot still shows that some photons deposit a few keV to recoiling electrons recorded by a high photon count in the energy range between 0 and 0.01 MeV. This is because at such photon energies, the cross section for photoelectric effect is much higher than that of Compton scattering for 0.511 MeV photons that once Compton scattered, they undergo through small deviation Compton scatter angles before being photo absorbed at their second interaction in the detector. This explains the occurrence of the second dominant peak of photons in figure 6.19 at an energy value of 0.510 MeV for energy deposition to the photo-electron. However on average, most photons deposit an energy value of 0.17 MeV to the photo-electron in their last interaction and the energy range of deposition at photoelectric effect is from 0.17 MeV to 0.510 MeV with an exponential decrease in photon count as photon energy increases in this range (Figure 6.19)

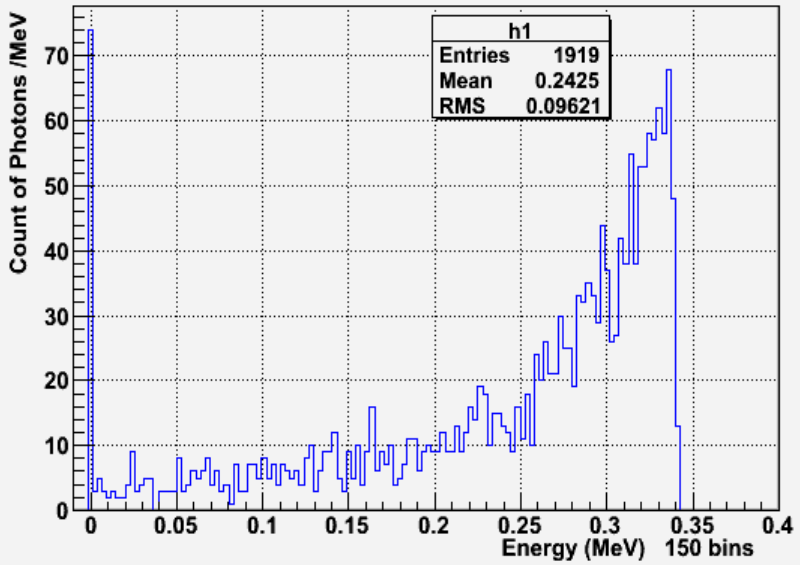

Figure 6.18: Spectrum of energy deposited to recoiling electrons at Compton scattering during a 160 MeV proton beam simulation.

The Angular distribution of the Compton scatter angles through which the 0.511 MeV photons are deviated off their original path before Compton scattering in the detector shows from figure 6.17 (Right) that a high count of photons undergoes through very small Compton scatter angles which corresponds to less energy deposition to Compton electrons and very high energy deposition to photo-electrons in figure 6.19. Other photons are Compton scattered through angles greater than 70^0 with a very low count to those that were almost back scattered to their original path of propagation.

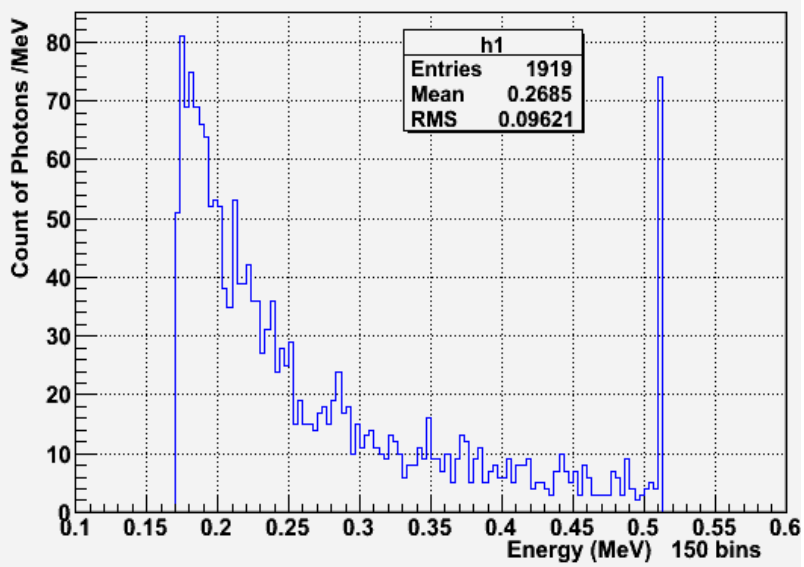

Figure 6.19: Spectrum of energy deposited to Photo-electrons. The few photon counts per MeV can be explained by the limited view capture of the Compton camera to the emitted 0.511 MeV photons since they are emitted back to back and some signal is missed out since the camera doesn't round about the phantom geometry like the case is for PET crystal detectors.

Investigating the production of 0.511 MeV photons with respect to the incident particle beam trajectory into the phantom, the distribution of such photons shows an accurate prediction of the main 160 MeV proton beam range depth into the soft tissue phantom with an increasing count of photons peaking at 15 cm depth and a sharp fall off before the 16 cm mark. The increase in production of 0.511 MeV photons till their peaking depth is due to increased energy loss of the incident proton beam particles that they deposit much of their energies at their extreme range so as to produce more positron emitters in the regions near the Bragg peak at 16 cm depth. From the facts of 0.511 MeV photon production point distribution, this can be used to precisely foretell the location of Bragg Peak which is targeted to be in the tumour site for maximum dose delivery to cancer cells and spare sensitive organs a few millimetre beyond the tumour as shown in figure 6.20 in which no photons are produced after 16 cm depth in the soft tissue phantom.

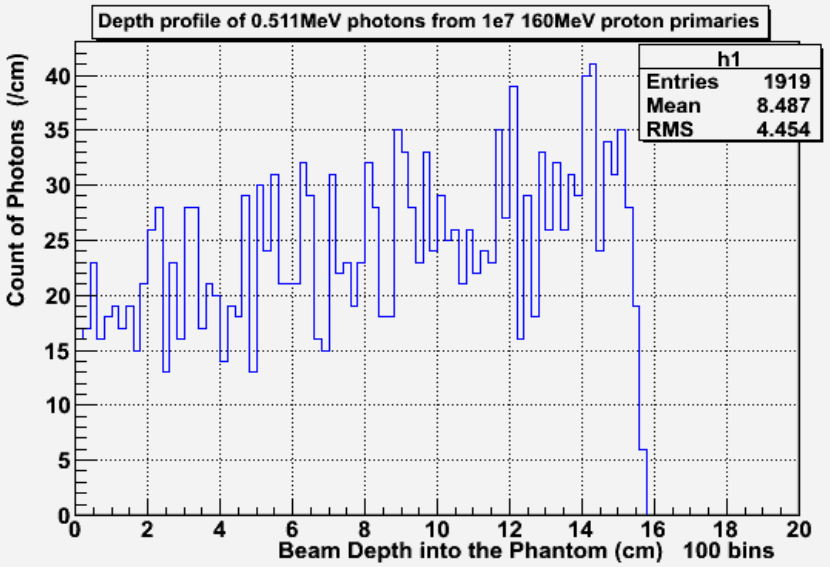

Figure 6.20: Production depth profile of 0.511 MeV photons during a 160 MeV proton beam simulation.

6.3.9 Angular resolution of the germanium block

Angular resolution of a Compton camera defined as the ability of the camera to clearly distinguish between any two near-by small objects is measured in imaging detectors using a parameter known as **Angular Resolution Measure** [ARM]. This is defined as the smallest angular distance between the reconstructed Compton cone from the energy measurements in the detector and the actual gamma point of emission if a cone was reconstructed using the exact emission, Compton scatter and photon absorption points. ARM estimates the values of angular resolution of the camera for high photon interaction events in the crystal detector and the smaller ARM is, the better angular resolution of the camera is attainable. From the Compton equation (27) in Chapter four, this equation is affected by energy uncertainties that arise from energy deposition events of photons to detector crystal electrons such as Compton recoil electrons and photo-electrons. This energy uncertainty leads to reconstruction of Compton cones with their circular base not precisely locating the original position of the gamma source emission point, Figure 6.21 and this effect becomes worse for low energy photons as it is in our case of study since the prompt gammas detected for the successive two interaction are in a range of 0.1 MeV and 1.6 MeV. The higher the incident gamma ray energy, the less energy uncertainty is felt in cone reconstruction so an improvement in spatial or angular resolution of the camera. The measure of energy uncertainty ($\Delta\theta_{Energy}$) is calculated by equation (30) below;

$$(\Delta\theta_{Energy})^2 = \left[\frac{m_e c^2}{E_0 sin\theta}\right]^2 (\Delta Edep_1)^2 + \left[\frac{m_e c^2}{sin\theta}\left(\frac{1}{E_o^2} - \frac{1}{E_1^2}\right)\right]^2 (\Delta Edep_2)^2 \qquad (30)$$

Where $(\Delta Edep_1)^2$ and $(\Delta Edep_2)^2$ are uncertainties in energies deposited at the compton scattering event site and photoelectric effect point respectively arising due to changes in the exact energy deposited and what amount is expected to be deposited at any particular event.

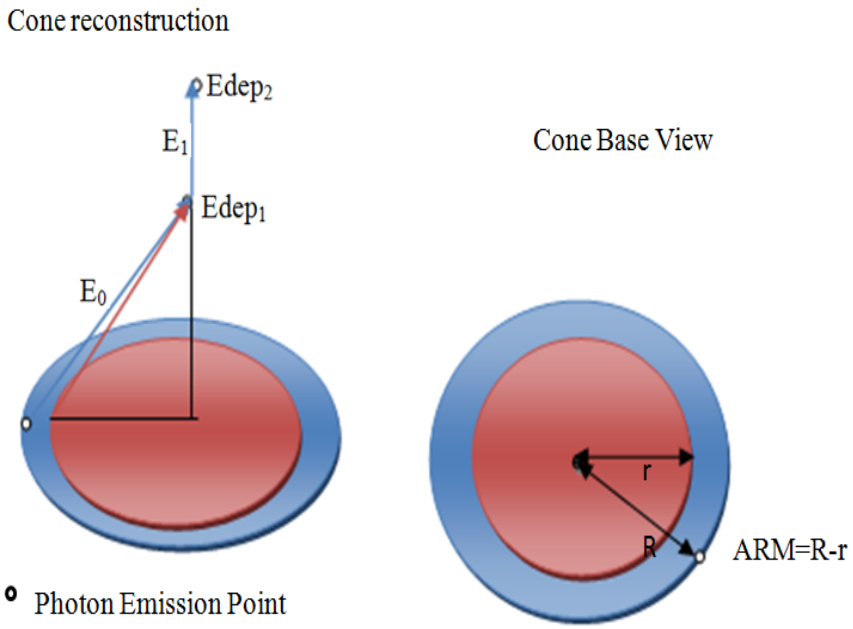

Figure 6.21: Illustration of Compton cone reconstruction uncertainties due to energy deposition in the detector causing a change in Compton angle measurement. Blue circle represents actual cone reconstruction from measurement of interaction points while as the brown cone base circle is as a result of cone reconstruction using energy measurements in the germanium detector.

Comparing each reconstructed Compton cone, using energy deposition, by its circular base (brown circle) with the expected reconstructed cone (blue) in the Compton cone reconstruction algorithm, a distribution of variation of ARM values in centimetres which inversely corresponds to Angular resolution, (figure 6.23) was analysed in the range difference between 0 and 70 cm for proton simulation and 0 and 160 cm for carbon ion simulation. For the proton beam simulation, cones that were reconstructed with an angular deviation of 15 cm and above have an exponential decrease in count because it is the low energy photons of less than 0.3 MeV greatly affected by energy uncertainty measures as the calculated Compton angle from energy deposition widely deviates from the actual and expected Compton angle without energy uncertainties however it is still in the same energy of 0.1 and 0.25 that the lowest energy uncertainty is recorded for precise Compton cone reconstruction (figure 6.22). And for the carbon ion beam simulation, a large deviation of reconstructed cones from energy deposition is noticed upto 160 cm. This is explained by the count of very low energy photons of less than 0.1 MeV that are affected by Doppler broadening leading to increased errors in precise and accurate Compton cone reconstruction. For better detector Angular resolution, the ARM values should be as low as possible so as to accurately reconstruct Compton cones for precise photon location by their origin in the phantom. Figure 6.23 shows that a high reconstructed cone count per centimetre for ARM values less than 1 cm would give appropriate imaging results of improved angular resolution of the detector reducing some of the noise though this comes with a cost of reduced utilization of reconstructed Compton cones hence less signal picked from the detector. Simulated results obtained from variation of ARM values from 5mm to 0.2mm with the aim of reducing energy uncertainties and improving

angular resolution of the detector are shown in figure 6.24. Distribution of photons by their emission points and location of maximum incident beam range are clearly shown until 3 mm, and increased reduction of ARM values tends to distort the distribution of photons by their position since few reconstructed cones are utilized. The gamma count recorded after the 16 cm depth mark into the phantom is as a result of detected photon emission points off the main primary 160 MeV proton beam path as illustrated also in figure 6.15. Such emission points are caused by secondary protons that have inelastic nuclear interactions with soft tissue nuclei that excited nuclei emit prompt gamma radiation at de-excitation.

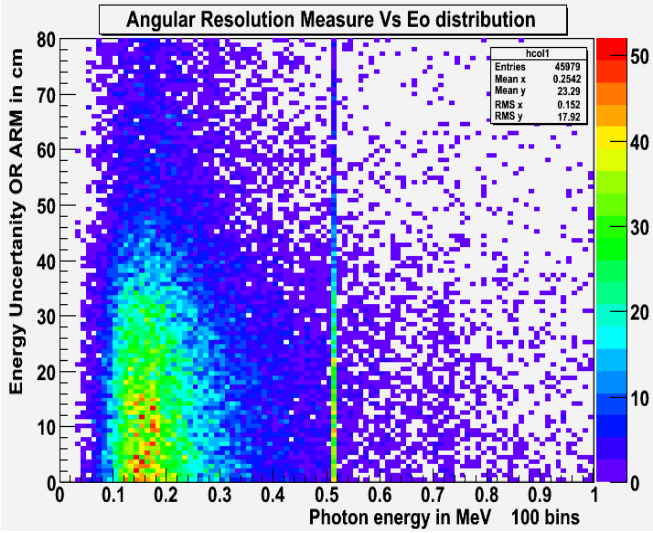

Figure 6.22: Variation of ARM with photon energy before Compton scattering occurs.

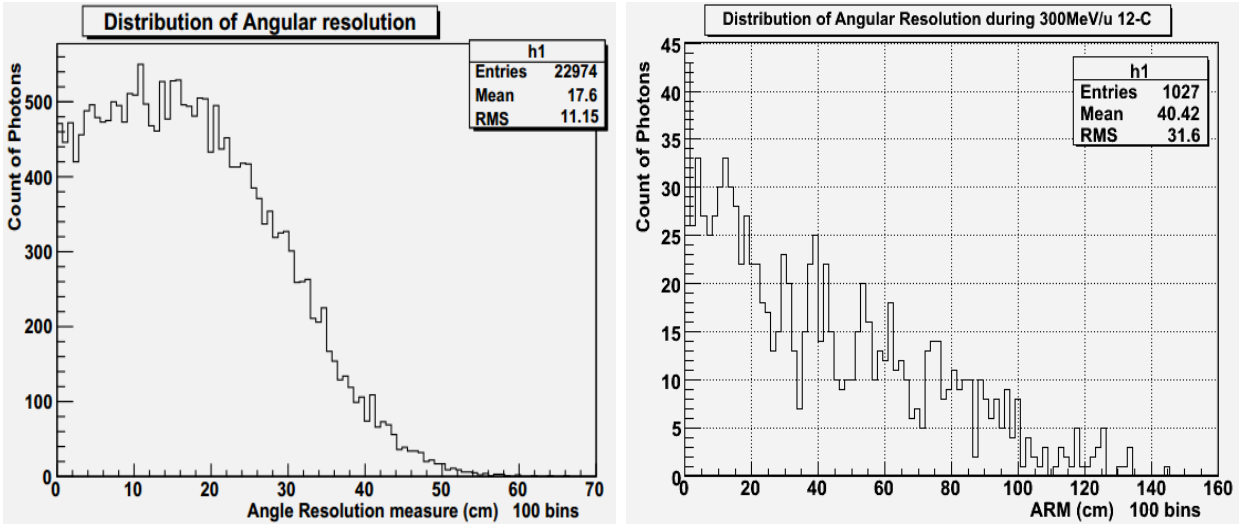

Figure 6.23: Distribution of ARM values showing the range through which reconstructed cones are deviated off the desired emission points of interest during a 160 MeV proton beam simulation (left) and 300 MeV/u carbon ion simulation (Right). Reduction in ARM improves Angular resolution and so does image quality improve.

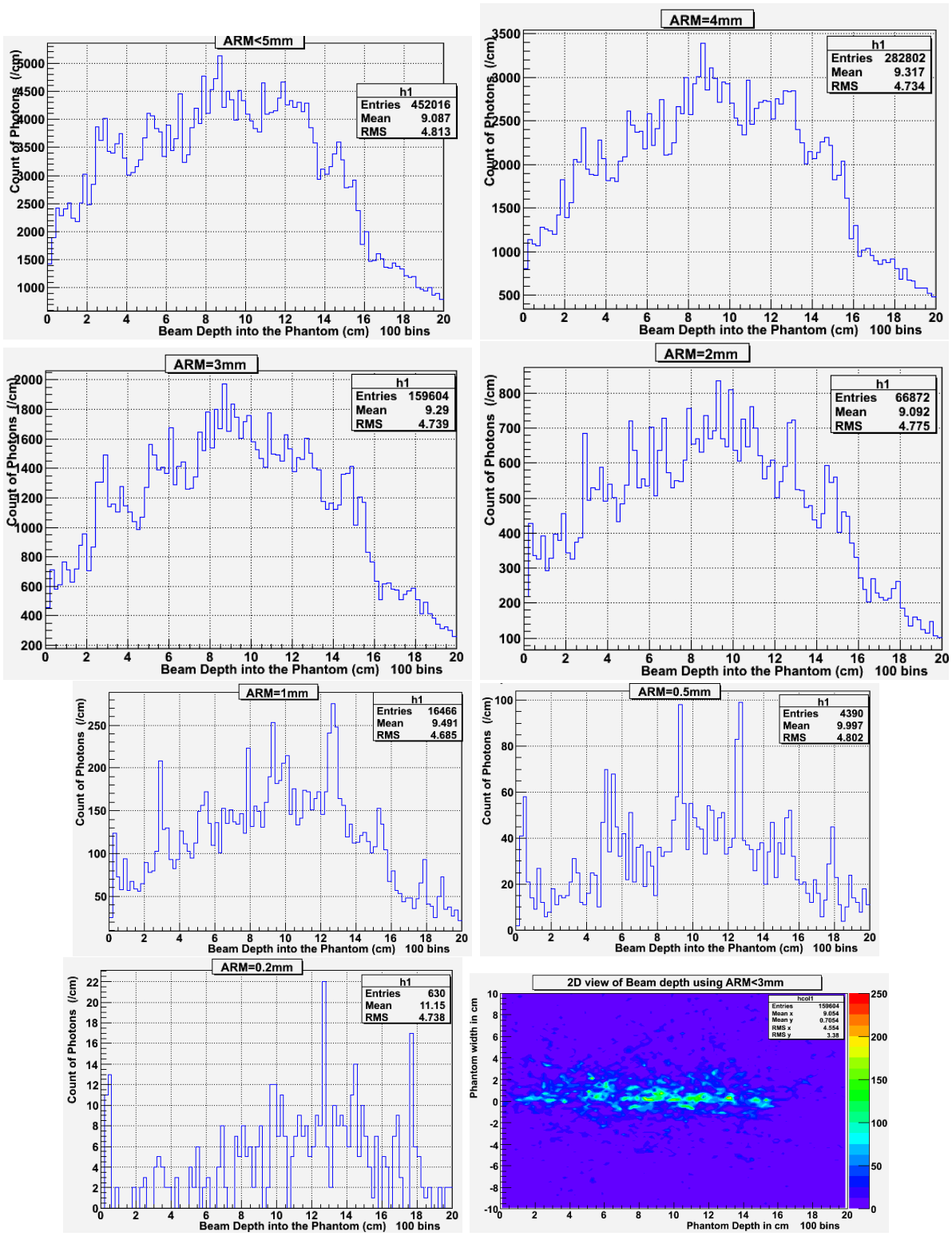

Figure 6.24: Simulated results of ARM variation. To the **bottom Right**, two Dimension view of the primary beam depth using ARM of less than 3 mm

6.3.10 Angular uncertainty and Doppler broadening

In the Compton scatter equation derived by Klein and Nishina for cross section of Compton scattering, the orbital electron is assumed to be unbound and at rest in the detector crystal however in reality, this is not the case. The electron is bound to the nucleus with a particular momentum and this leads to a slight variation in Compton scattering cross section predicted by Roland Ribberfors in 1975, different from that of Klein and Nishina. This effect is known as Doppler Broadening discovered by Jesse DuMond in 1929. To describe the Compton scattering cross section for such bound electrons, Roland Ribberfors in 1982 modified the cross section prediction of Klein and Nishina to the equation (31)

$$\left(\frac{d\sigma}{d\Omega}\right)_{bC,i} = \left(\frac{d\sigma_e(E_o,\Omega)}{d\Omega}\right)_{uBC} S_i^I(E_o,\theta,Z) \tag{31}$$

where S_i^I was the incoherent scattering function of the i^{th} shell electrons and Z, the atomic number of the detector material. This is the bound Compton scatter cross section expression taken into account for low energy photons that undergo Compton scattering at their first interaction event in a imaging detector. This effect of Doppler broadening is more pronounced in low energy photons of energies less than 0.1 MeV, illustrated by figure 6.25 and for photons of sufficient energy above 0.1 MeV, the effect is negligible that the unbound and bound Compton scatter cross sections come in agreement.

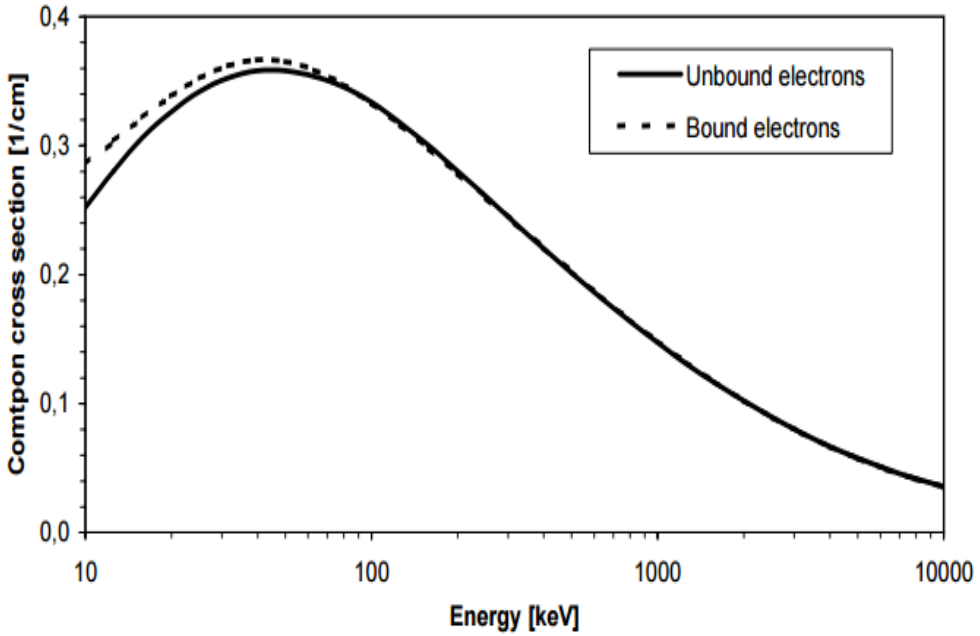

Figure 6.25: A variation of Compton scatter cross section for bound and unbound electrons with respect to incident photon energies. Image extracted from [76].

Doppler broadening causes a variation in the energy distribution between the recoiling electron and the scattered photon. As a result, there is a change in the measured Compton angle leading to broadening of the reconstructed cones off the desired emission points increasing angular uncertainties in the detector block. Doppler Broadening is more pronounced for

low energy incident photons before Compton scattering, high atomic number material of the detector and for intermediate Compton scatter angles between 30^0 and 130^0. Figure 6.26 extracted from [76] shows the variation of Compton cross section of bound and unbound Compton scattering as a function of Compton scattering angles at 0.1 MeV. And for our 160 MeV proton beam simulation studies, the results were never affected by Doppler broadening since the prompt gamma spectrum in figure 6.16 shows the energy range from 0.1 MeV to 1.6 MeV for photons undergoing successive Compton scattering and photoelectric effect however for the 300 MeV/u carbon ion simulation from the energy spectrum in figure 6.16, the spectrum ranges from 0.05 MeV to 1.6 MeV and 5% of these photons had their energies less than 0.1 MeV and were affected by Doppler Broadening. To minimise the uncertainties in angular resolution measurements, such photons were ignored in the reconstruction algorithm.

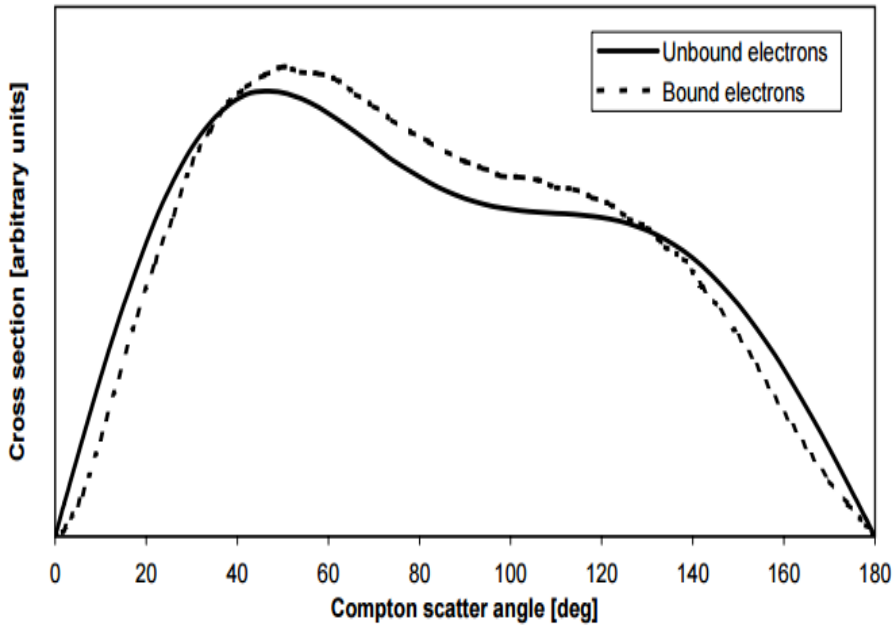

Figure 6.26: Variation of Compton scatter cross section for unbound and bound electrons predicted by Klein-Nishina and Roland Ribberfors respectively with respect to Compton scatter angles. A suppression as a result of Doppler broadening is noticed at extreme (very small and very large) angles. This effect of angle suppression is reduced for high energy photons [76].

6.4 Single scattering Compton camera

Another kind of Compton camera proposed for use today in medical imaging is a single scattering Compton camera that consists of a separate scattering crystal called a scattering detector and a second detector as absorber detector for photon absorption. To maximize its gamma detection performance through increasing the number of Compton scattering events since the camera technique is based on such scattering events first discovered by H.G. Compton in 1923 [77], a low atomic number material that favours Compton scattering for a wide range of photon energies has been chosen as silicon over a high atomic number materials like germanium however for sufficient signal acquisition, a high atomic number crystal is required since at reduced energies of scattered photons, materials of high atomic number exhibit a high cross section for photoelectric effect and in this case, germanium crystal has been chosen. Two successive photon interaction events are still considered as before in the HPGe Compton camera in the order of single Compton scattering first in the scattering detector and such a photon undergoing photoelectric effect in the absorber detector placed a few centimetres away from the scattering detector assuming that all its energy is fully deposited in the germanium crystal. Reconstruction of photon position from the soft tissue phantom has been performed in the same way as in the crystal block germanium Compton camera using the Compton kinetics of calculating the Compton angle and reconstructing back projected cones which contain the possible location of photon origin identified by common intersection point of the reconstructed cones.

The single scattering Compton camera used in this project has been optimized in geometry for better performance and gamma ray detection. The scattering silicon detector has been optimised to dimensions of 24x2x24cm^3 placed perpendicular to the incident pencil beam and 5 cm at the top of the human soft tissue phantom of dimensions 10x10x10cm^3 having an extension of 2 cm at its edge to cater for the widely spreading photons emanating out of the phantom. The scattering silicon detector of 2 cm thickness was placed 8 cm away from the absorber germanium crystal of dimensions 36x6x36cm^3 and still placed 15 cm away from the soft tissue phantom. A wider separation distance between the scattering and absorber detector of 8 cm was implemented in the detector design so as to cover very low energetic photons that are widely Compton scattered in the silicon detector. The two detector sets of this Compton camera are in a vacuum region surrounded by a black hole as shown in figure 6.27

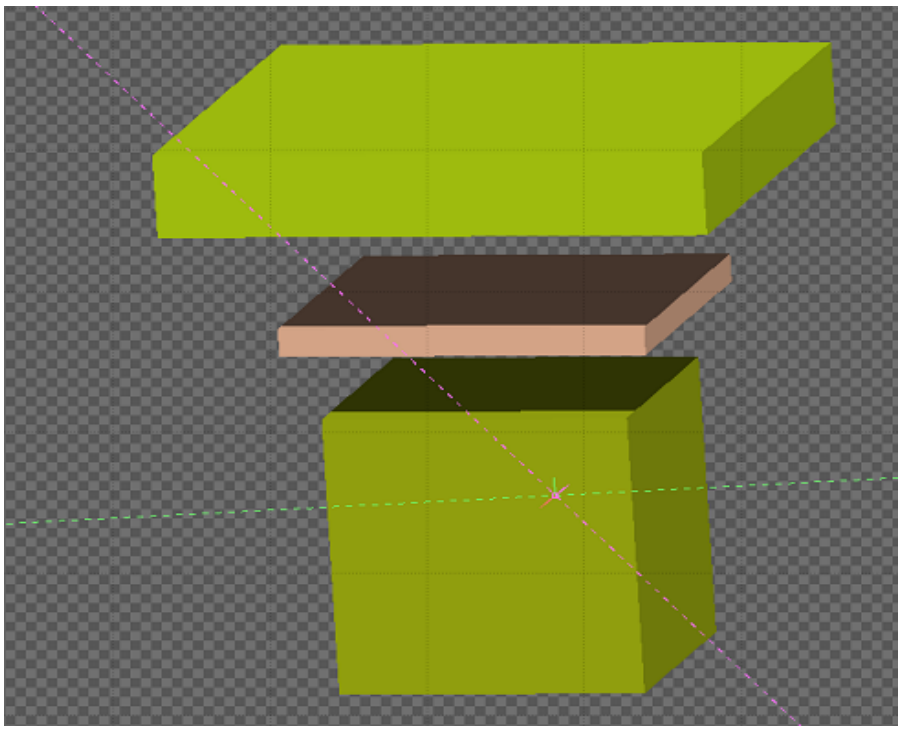

Figure 6.27: Simulation set up for the single scattering Compton camera. **Top** most is the absorber detector followed by silicon scattering detector. These first two set-ups are the basic components of the single scattering Compton camera and to the **bottom** is the soft tissue phantom.

6.4.1 Energy spectra of photons

Similar to the energy spectrum of prompt gamma rays incident on the germanium crystal Compton camera in figure 6.16, the energy spectrum of photons before being Compton scattered in the silicon detector exhibits two distinct peaks with a dominant at 0.14 MeV and the second due to 0.511 MeV photons resulting from positron emitters. Beyond this energy values with increase in photon energy (figure 6.28), few counts of photons are recorded upto 3 MeV showing that the single scattering Compton camera made up to a separate scattering detector and absorber detector has a wide photon energy span utilized for photon position imaging compared to the HPGE block Compton camera with an energy spectrum range from 0.1 MeV to 1.6 MeV. This improvement in the performance of the single scattering Compton camera can be best explained by the use of a low atomic number material (Si) with a very good cross section for Compton scattering of photons at their first interaction in the silicon detector though a cost of reduced energy resolution of the camera is incurred other than if germanium was used as a scatterer detector.

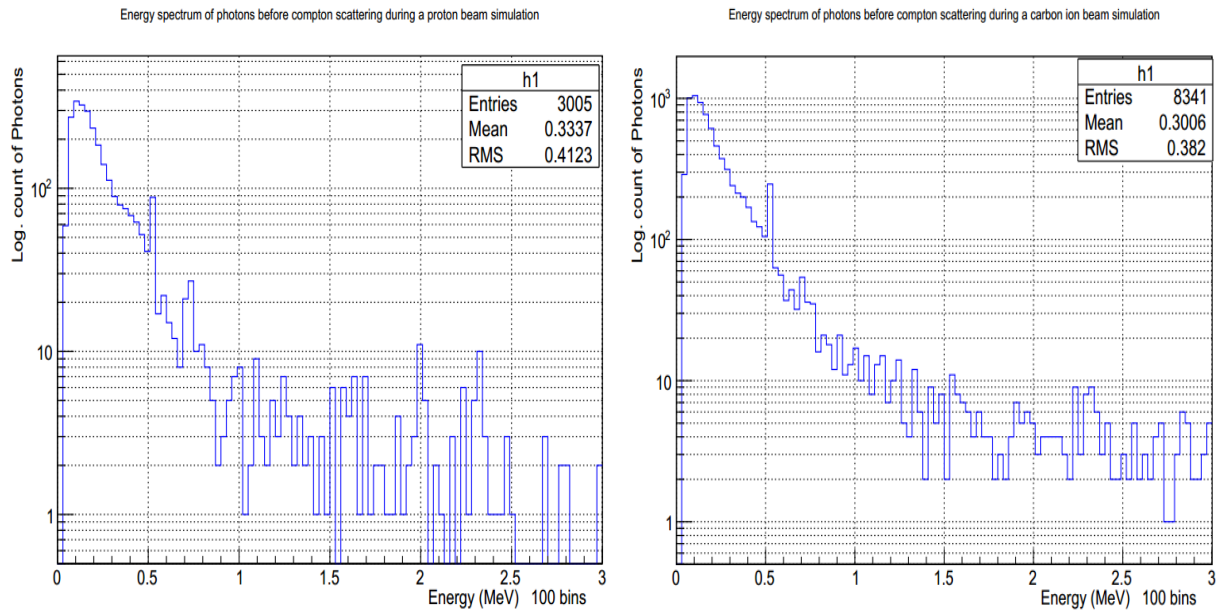

Figure 6.28: Logarithmic nergy spectra of photons before being Compton scattered in the silicon detector of the single scattering Compton Camera during a 160 MeV proton beam simulation (**Left**) and 300 MeV/u ^{12}C simulation (**Right**). Two small peaks at 0.511 MeV and 0.7MeV correspond to photons produced from electron-positron annihilation and photons from de-excitation from ^{10}C nuclei respectively

From equation (27), the incident photon to the silicon crystal deposits energy at the Compton scattering site. This energy is supplied to the assumed to be unbound stationary electron that it is set into motion with in the silicon detector and part of the deposited energy is transferred to detector atom equal or greater than the binding energy of an electron to be ionised off that particular atom. The recoiling electron can have sufficient kinetic energy that it escapes out of the silicon detector or undergoes energy loss within the scattering detector through multiple elastic and inelastic scattering that can result into bremsstrahlung. These bremsstrahlung photons can be absorbed in the germanium detector causing noise in the detected signal however, if the recoiling electrons deposit all their kinetic energy in the silicon detector, they can be used to have a precise Compton cone reconstructed for accurate prediction of photon emission points using the cone reconstruction algorithm. Figure 6.29 shows the spectrum of prompt gamma energy deposited in the silicon scattering detector for our simulated Compton camera varying from a few keV with a sharp exponential fall in the photon counts per MeV recorded as the deposited energy increases.

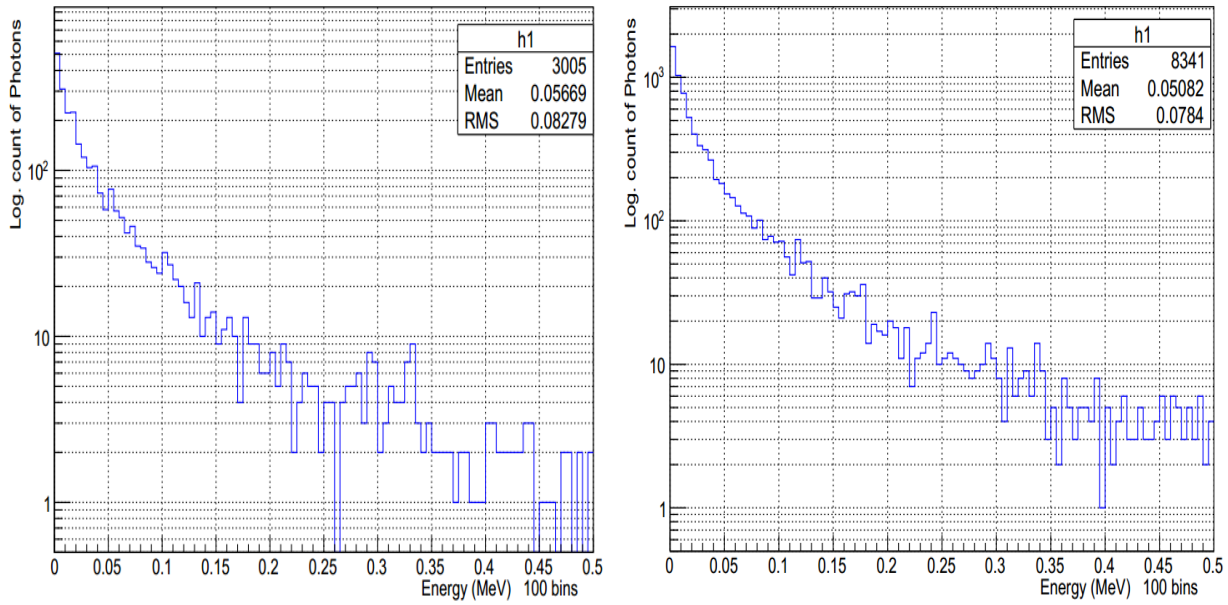

Figure 6.29: Logarithmic spectra of energy deposited in the silicon detector of the single scattering Compton camera during a 160 MeV proton beam simulation (**Left**) and 300 MeV/u ^{12}C simulation (**Right**).

In all our calculations involved in the Compton camera kinematics, the scattered photons from the silicon detector deposit all their energies in the germanium absorber detector and no gamma Compton scattering in the absorber detector is catered for. Figure 6.30 shows the energy deposited in the germanium absorber detector which is supplied to the photo-electron at occurrence of photoelectric effect.

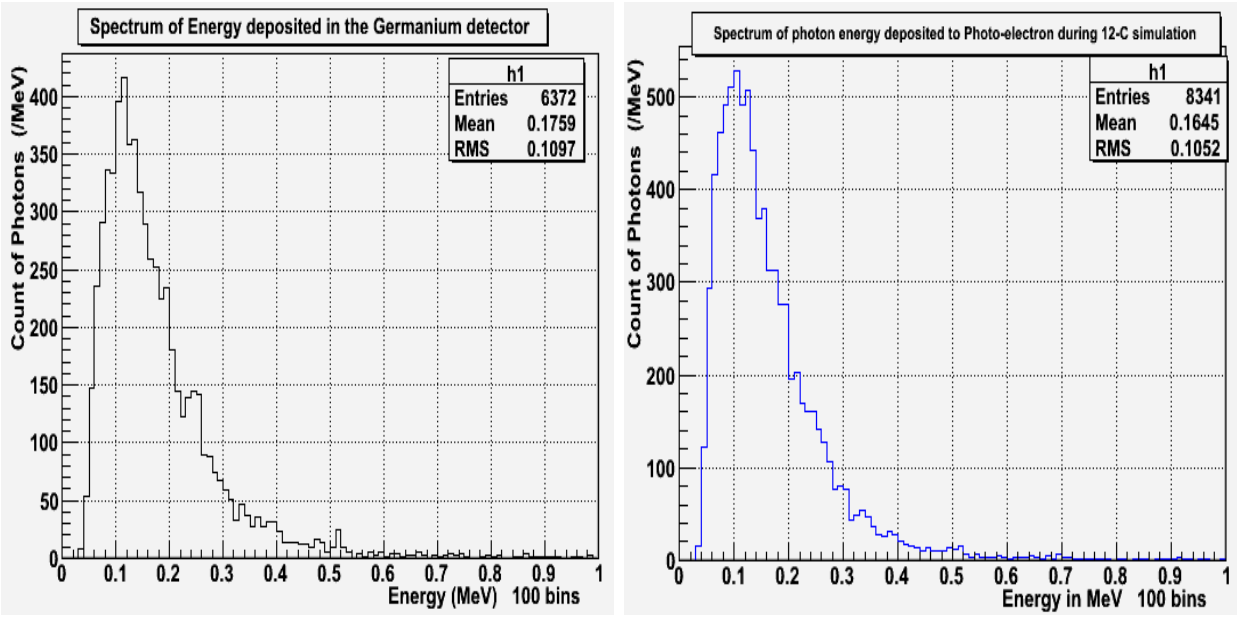

Figure 6.30: Spectra of energy deposited in the germanium detector of the single scattering Compton camera during a 160 MeV proton beam simulation (**Left**) and 300 MeV/u ^{12}C simulation (**Right**). A peak corresponding to electron-positron annihilation photons is evident at 0.511 MeV.

6.4.2 Algorithm results for single scattering Compton camera

The same iterative algorithm as previously applied to the germanium block Compton camera has been used to reconstruct Compton cones formulated from energy deposition at both Compton scattering and photoelectric effect points in the scattering and absorber detectors of the camera respectively. The apex for each back projected cone is positioned at the Compton scattering point in the silicon detector and the cone axis is obtained from joining both photoelectric effect and Compton scattering points. The opening angle of such cones is twice the Compton scatter angle calculated from energy deposition using equation 27. All reconstructed cones are projected to the incident beam trajectory to accurately locate production points of prompt gammas by intersection of reconstructed base cone circles in the incident beam plane through the soft tissue phantom.

For accurate Compton cone reconstruction, the Angular Resolution Measure (ARM) has been implemented in the algorithm to improve the angular resolution of the camera and studies on ARM values of 8 mm, 7 mm, 6 mm, 5 mm, 4 mm and 3 mm have been analysed using the graphical representation of prompt gamma production points in the phantom as shown in figure 6.31. Results show that ARM value of 6 mm and below would give a better angular resolution for the single scattering Compton camera with sufficient utilisation of reconstructed cones for monitoring of the primary beam range and Bragg peak position at 16 cm depth. The 0.511 MeV photon peak in figure 6.28 was never exploited using this camera as it would give a very small signal with low photon counts at the absorber detector. This is due to such photons being photo-absorbed in the silicon detector since the cross section for photoelectric effect is higher than that of Compton scattering for 0.511 MeV photons in-spite of the low atomic number of silicon in comparison to that of germanium.

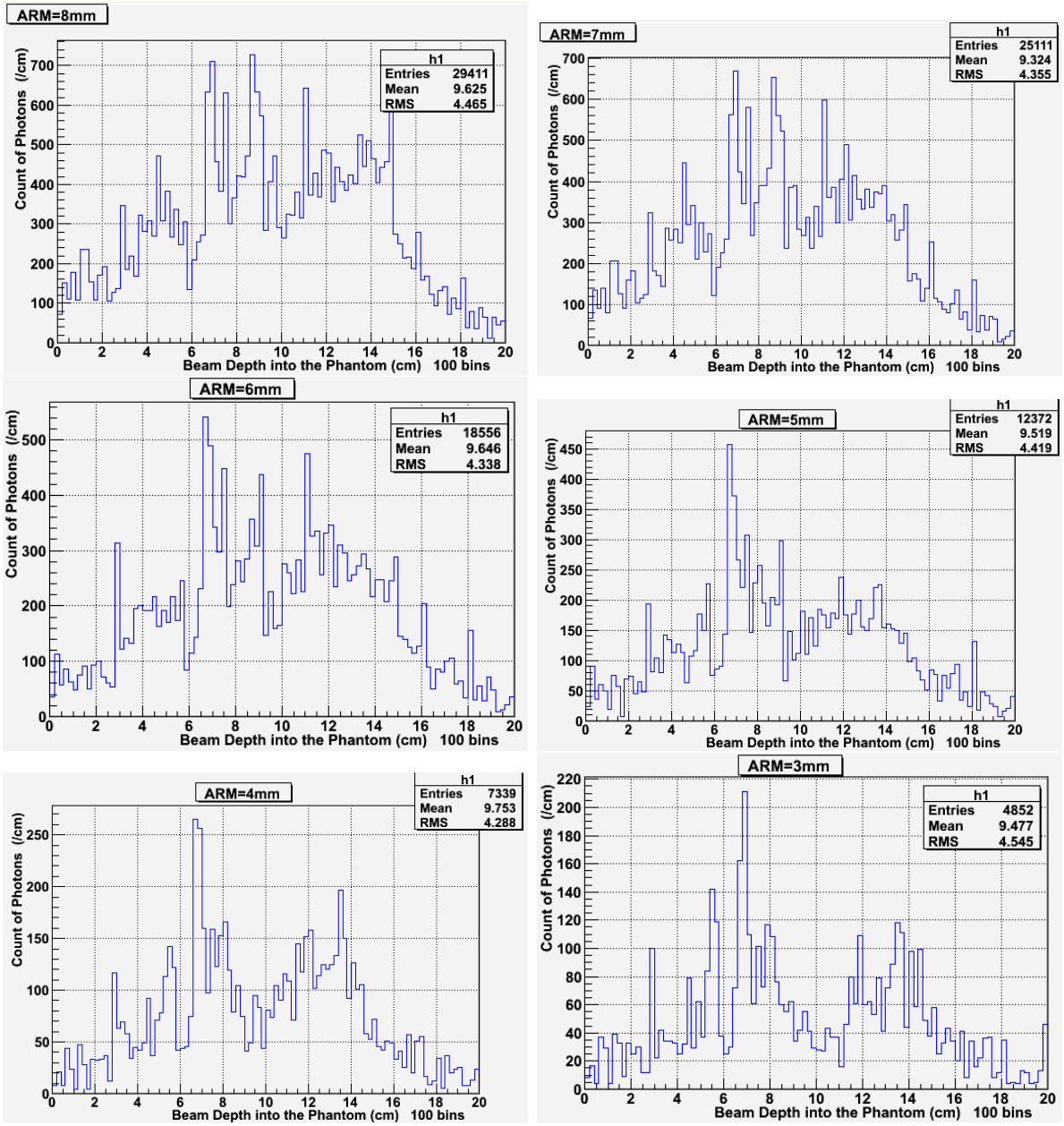

Figure 6.31: Simulated results of ARM variation using single scattering Compton camera for 160 MeV proton beam simulation.

6.5 Overall reconstruction efficiency

6.5.1 Geometrical acceptance

This has been defined as the fraction of photons hitting the detector to the number of all photons produced and emitted out of the soft tissue phantom. For the HPGe Compton camera, it was calculated as 8% and that of single scattering Compton camera calculated as 5%. This implied that the single scattering Compton camera utilized more of detected photons to study location of photon production with respect to the proton incident pencil beam due to the increased cross section for Compton scattering in the silicon detector and increased cross section of photoelectric effect at germanium detector.

6.5.2 Intrinsic efficiency

This has been defined as the fraction of photons registered by the camera from the Bragg peak region for Compton cone reconstruction to the number of photons hitting the detector from the same region. Using the HPGe Compton camera, the intrinsic efficiency was calculated to be 0.4% using ARM value less than 3 mm applied to image the Bragg peak in the region between 15 cm and 16 cm during a proton beam simulation. For the single scattering Compton camera, it was calculated to be 1.4% using ARM value less than 6 mm. This implied that the single scattering Compton camera had a better efficiency over the HPGe Compton camera in imaging photon production points in the soft tissue phantom though the efficiency was still low. Higher efficiency than that of HPGe Compton camera was due to the use of silicon as scatterer detector that favoured more of high energy photons to be scattered to reduced energies for photo-absorption in germanium detector.

6.5.3 Total efficiency

Total efficiency has been defined as a product between the intrinsic efficiency and the geometrical acceptance of the detector. For the HPGe Compton camera, it was calculated to be 0.032% while as for the single scattering Compton camera, it was 0.07%. From the calculated overall efficiency, the single scattering Compton camera proves to be a better imaging device for photons. This is attributed to the use of a separate scattering detector of silicon with a low atomic mass that increases the cross section for Compton scattering of photons in a wide energy range. Since a Compton camera functions on the principle basics of photon Compton scattering, increment in such scattering would increase its detection efficiency because such photons are absorbed by the absorber detector placed 8 cm away from scatterer detector with a wide detection plane to increase cross section for photon absorption.

6.6 Comparison of results

A comparison of results obtained using the proposed Compton cone reconstruction algorithm with the exact photon production distribution shown in figure 6.6 and the dose deposition curve of the 160 MeV proton beam have been analysed using figure 6.32 below for both HPGe Compton camera and single scattering Compton camera. Spatial resolution of less than 3 mm for HPGe Compton camera and less than 6 mm for single scattering Compton camera have shown a precise prediction of photon production used to image incident proton beam range in the soft tissue phantom. The algorithm result curve in black color has been scaled by a factor 3 to magnify the maximum photon yield with respect to the proton beam depth and the fall off near the Bragg peak. The rapid fall off occurs at 15.8 cm which is just 0.2 cm behind the Bragg peak at 16 cm. This is in agreement with the exact photon production yield in the blue plot.

Inflection points on both algorithm photon yield and actual photon yield curves were used to calculate how precise the algorithm method was to locate the distal fall off. To find the inflection points on both curves, 50% of the photon yield was calculated at the distal fall off. The inflection point of the actual photon yield curve was located at 15.49 cm with respect to the incident particle beam depth while for algorithm results in both HPGe Compton camera and single scattering Compton camera was located at 15.5 cm. Thus, the algorithm results precisely located the distal off of the original photon yield by precision of 0.1 mm.

The high counts of photons in the algorithm results were recorded before the fall off as these arose from the few energy uncertainties that the constructed cones incorrectly predicted photon production points especially those off the primary beam trajectory. Low count of photons after the distal fall off at 15.8 cm in the algorithm results were due to neutron induced photons off the primary proton beam trajectory.

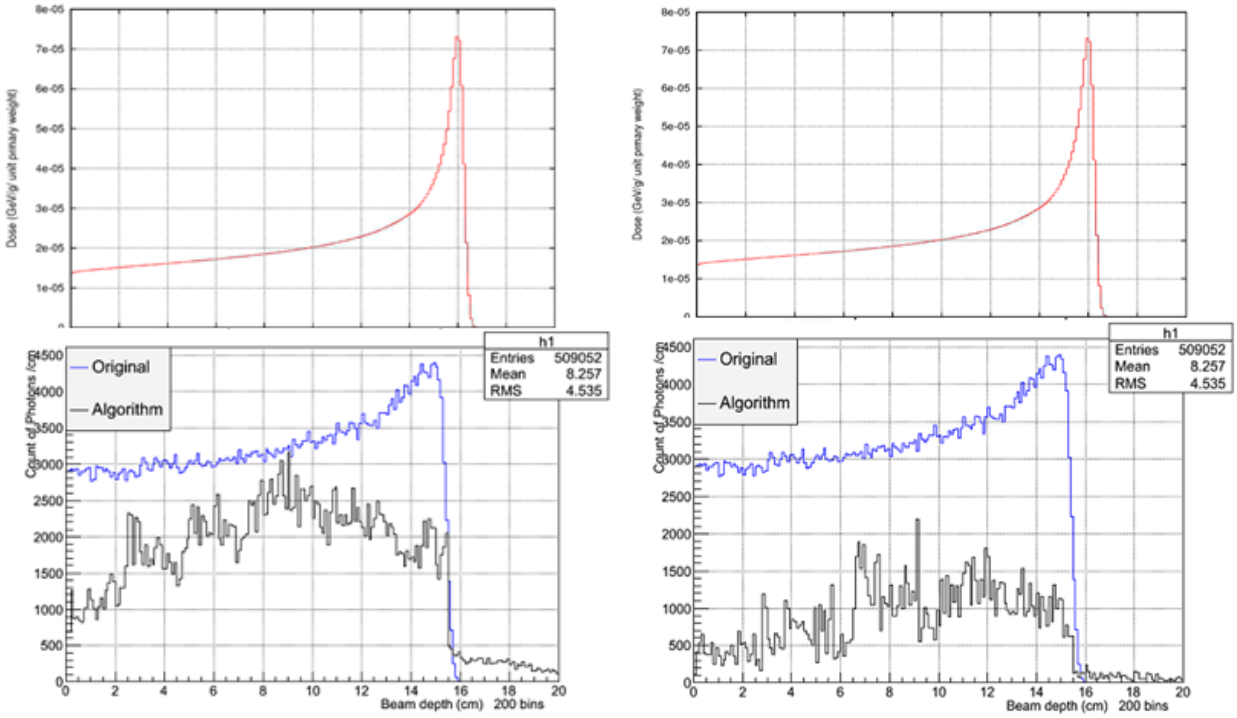

Figure 6.32: Comparison of algorithm photon production results with exact yield of photons and dose-depth curve for HPGe Compton camera (**left**) and single scattering Compton camera (**right**). The algorithm results have been scaled by a factor of 3.

7 Conclusion

The aim of hadron therapy in medicine practice is to sufficiently deliver radiation dose to tumour volumes with a safety precaution of sparing any organs at risk which may be in the vicinity of the cancer location so as to prevent secondary cancer development after patient treatment. Both protons and carbon ions are in use today for oncology purposes and in this project, protons and carbon ion beam simulations have been critically analysed to study the physical properties of photons emitted as secondary radiation and how they interact with semi conductor detectors during hadron therapy. The detection systems included in the simulations are; germanium block Compton camera and single scattering Compton camera made up of silicon scatter detector and germanium absorber detector.

The energy loss computed from Bethe Bloch formula shows a maximum energy deposition of incident primary beams in the Bragg peak at 16.6 cm and 16.3 cm with FWHM of 2 cm and 4 mm for 160 MeV proton beam and 300 MeV/u carbon ion beam simulations respectively. A negligibly low energy deposition is exhibited in the proton beam simulation beyond the Bragg peak position while in carbon ion simulations, some energy is deposited by secondary neutrons and protons in regions beyond the distal falloff of the Bragg peak. This feature of carbon ions should be taken care of during therapeutic procedures as it deposits unwanted dose to body organs a few centimetres after the targeted tumour volume. The number of nuclear inelastic interactions per centimetre between the primary beams and soft tissue show an increasing count till a 15.8 cm depth into the phantom for a carbon ion simulation while as for the proton beam simulation, it shows an increasing count till a 14.8 cm. For carbon ion simulations, a significant count of stars is noted after the maximum count attributed to secondary neutrons and protons interacting with soft tissue nuclei in inelastic collisions.

In both simulations, secondary protons are emitted through small angles less than 90^o to the primary beam trajectory, a characteristic of secondary protons that has been exploited in Proton Vertex Imaging (PVI) through accurate tracking detector positioning to precisely locate the vertex of emission point of secondary protons for beam range monitoring. Most of secondary neutrons produced in the soft tissue phantom are thermal neutrons of energies less than 0.7 MeV which undergo multiple scattering to increase their cross section for neutron capture within the phantom however, a few fast neutrons from both simulations are ejected out of the phantom after being scattered in the soft tissue sample and reach out to the Compton camera detection system. Photons emitted out of the soft tissue sample are isotropically distributed in all phantom direction with a poly-energetic nature exhibited in the energy spectrum with distinct peaks at 2.3 MeV, 3.4 MeV, 4.4 MeV, 5.2 MeV and 6.3 MeV corresponding to atomic nuclei de-excitation of ^{14}N, ^{20}Ca, ^{12}C, ^{14}N and ^{16}O respectively. With an even distribution of secondary photons, the detection setting of a Compton camera was placed orthogonal to the incident primary beam trajectory, top of the phantom even though scattered photons show a higher count at angles greater or less than 90^o.

A study on a gamma camera known as a pin hole camera showed that such a detector was not appropriate for detection of high energetic photons of range from 0.001 MeV to 10 MeV since from the results, the production of orthogonal photons to lead septa holes never

showed a precise location of the primary beam range. This called for an alternative in the way photons are collimated before detection. The solution to such a limitation was the use of a mechanical collimator free Compton camera.

The study on prompt gamma emission by energy selection of photons in the ranges 0-2 MeV, 2-4 MeV, 4-5 MeV and 6-20 MeV showed that the energy interval of 4-5 MeV exhibited the highest photon count with a maximum of 2600 photons/cm reported 0.2 cm before the Bragg peak in a 160 MeV proton pencil beam simulation of 10^7 primaries while as other energy intervals yielded their maximum count less than 1800 photons/cm. The high count contribution of 4-5 MeV was attributed to the abundance of ^{12}C excited nuclei in the soft tissue that de-excited by emission of 4.4 MeV photons thus providing adequate photon count of signal acquisition to study prompt gamma production in patients during treatment procedures. The time of flight between photons and neutrons was found to have a difference of 2 ns. This concept has been utilised in PET scanners called TOF PET scanners to eliminate background noise from photon signal for image processing. The energy resolution of the germanium block Compton camera was assumed to be 2 keV at 1 MeV (0.2%) photon.

The iterative computational algorithm for Compton cone reconstruction using the germanium block Compton camera reported the energy spectrum of prompt gammas before Compton scattering exhibiting dominant photon peaks at 0.2 MeV and 0.18 MeV for proton beam and carbon ion beam respectively showing that lower energy photons from the carbon ion beam simulation are favourable for both Compton scattering and photoelectric effect as their two successive interaction processes in this Compton camera. However, the energy spectrum of such photons from the carbon ion simulation was affected by Doppler broadening since photons of energy less than 0.1 MeV were recorded as compared to those in the proton beam simulation which were above 0.1 MeV. This effect of Doppler broadening was eliminated from the simulation by truncation since it was only 5% of the photon energy spectrum. For both beam simulations, their energy spectra exhibited a characteristic photon peak of 0.511 MeV that corresponded to the contribution from electron-positron annihilation photons. Such 0.511 MeV photons deposited average energy values of 0.33 MeV to recoiling electrons and 0.17 MeV to photon-electrons at Compton scattering and photoelectric effect events respectively. The cross section for photoelectric effect is higher than that of Compton scattering for 0.511 MeV photons and this led to occurrence of the second dominant photon peaks at a few keV in the spectrum of photon energy deposited to recoil electrons and 0.510 MeV in the spectrum of energy deposited at photoelectric effect events.

The quantity of ARM which was a measure of detector angular resolution showed for germanium block Compton camera, better prediction of the incident particle range at 3 mm for proton beam simulation while as when using a single scattering Compton camera, the ARM value less than 6 mm showed better photon production and emission results. Decrease in ARM values for both cameras would lead to incorrect prediction since few Compton cones reconstructed from the algorithm would be used limiting the Compton camera efficiency. Meanwhile, a single scattering Compton camera utilised more of the prompt gamma energy spectrum for the two successive photon interaction events since photons in the range from 0.03 MeV to 3 MeV were used for photon imaging while the germanium block Compton

camera only just covered a photon energy spectrum ranging from 0.1 MeV to 1.6 MeV. But the single scattering Compton camera results were affected by Doppler broadening. The single scattering Compton camera was found to have a better overall efficiency of 0.07% over 0.032% for HPGe Compton camera.

Finally, a comparison of cone reconstruction algorithm results with dose deposition curve showed a good prediction of the incident beam range with a distal fall off at 15.8 cm. For both Compton cameras, the reconstruction source distribution tracked the original one at the distal fall off by a precision of 0.1 mm.

References

[1] L. U. Malcolm R Alison, Imperial College School of Medicine, "Cancer,"

[2] B. Shayegan, S. O. Head, *et al.*, "Surgery for prostate cancer," *UTMJ*, p. 182.

[3] D. o. O. P. M. H. Dr. Carol Kwok, Clinical Oncologist, "Management of side effects from chemotherapy,"

[4] N. P. Brodin, P. M. A. Rosenschöld, M. C. Aznar, A. Kiil-Berthelsen, I. R. Vogelius, P. Nilsson, B. Lannering, and T. Björk-Eriksson, "Radiobiological risk estimates of adverse events and secondary cancer for proton and photon radiation therapy of pediatric medulloblastoma," *Acta oncologica*, vol. 50, no. 6, pp. 806–816, 2011.

[5] U. Amaldi, "Hadrontherapy in the world and the programmes of the tera foundation.," *Tumori*, vol. 84, no. 2, pp. 188–199, 1997.

[6] M. T. Studenski and Y. Xiao, "Proton therapy dosimetry using positron emission tomography," *World journal of radiology*, vol. 2, no. 4, p. 135, 2010.

[7] F. Le Foulher, M. Bajard, M. Chevallier, D. Dauvergne, N. Freud, P. Henriquet, S. Karkar, J. Létang, L. Lestand, R. Plescak, *et al.*, "Monte carlo simulations of prompt-gamma emission during carbon ion irradiation," *Nuclear Science, IEEE Transactions on*, vol. 57, no. 5, pp. 2768–2772, 2010.

[8] F. Le Foulher, M. Bajard, M. Chevallier, D. Dauvergne, N. Freud, P. Henriquet, S. Karkar, J. Létang, L. Lestand, R. Plescak, *et al.*, "Monte carlo simulations of prompt-gamma emission during carbon ion irradiation," *Nuclear Science, IEEE Transactions on*, vol. 57, no. 5, pp. 2768–2772, 2010.

[9] *Beta Decay Spectrum*, 2015 (accessed May 11, 2015).

[10] D. Groom and S. Klein, "Passage of particles through matter," *The European Physical Journal C-Particles and Fields*, vol. 15, no. 1-4, pp. 163–173, 2000.

[11] *Dose-Depth Curves*, 2015 (accessed May 01, 2015).

[12] H. Nikjoo, S. Uehara, and D. Emfietzoglou, *Interaction of radiation with matter*. CRC Press, 2012.

[13] J. Hubbell, "Review of photon interaction cross section data in the medical and biological context," *Physics in medicine and biology*, vol. 44, no. 1, p. R1, 1999.

[14] H. Hirayama, "Photon interactions and cross sections," November 2000.

[15] O. U. C. B. L. I. Marie-Helène Richard, "Design study of a compton camera for prompts-gamma imaging during ion beam therapy," 2012.

[16] P. Rinard, "Neutron interactions with matter," *Passive Nondestructive Assay of Nuclear Materials*, pp. 357–377, 1991.

[17] C. Robert, G. Dedes, G. Battistoni, T. Böhlen, I. Buvat, F. Cerutti, M. Chin, A. Ferrari, P. Gueth, C. Kurz, *et al.*, "Distributions of secondary particles in proton and carbon-ion therapy: a comparison between gate/geant4 and fluka monte carlo codes," *Physics in medicine and biology*, vol. 58, no. 9, p. 2879, 2013.

[18] A. B. K. B. A. C. P. Schaffer1, F. Bnard, "Direct production of metastable 99-tc via 100-mo(p,2n) on small medical cyclotrons,"

[19] T. B. W. Schlegel and H. A.-L. Grosu Springer Verlag, "Proton beam radiotherapy - the state of the art1," 2005.

[20] D. Schlyer, P. Van den Winkel, T. Ruth, M. Vora, M. Pillai, and M. Haji-Saeid, "Cyclotron produced radionuclides: Principles and practice," tech. rep., Technical Reports Series.

[21] W. R. Hendee, "Proton and carbon ion therapy," *Imaging In Medical Diagnosis and Therapy*, 2013.

[22] D. E. H. J. E. K. T. S. P. A. J. Timothy W. Koeth, George A. Hine, "Comparison of azimuthally varying with constant gradient magnetic fields with the rutgers 12-inch cyclotron," June 23, 2011.

[23] K. Hock, "Sextupole magnet," *transfer*, vol. 5, no. y2, p. 14, 2010.

[24] K. Sato, S. Matsumoto, K. Noda, Y. Miyazawa, H. Suzuki, T. Yamada, S. Yamada, T. Kanai, Y. Hirao, A. Noda, *et al.*, "Heavy ion medical accelerator in chiba (himac)," *Part. Acc*, vol. 33, p. 147, 1990.

[25] K. Endo, K. Mishima, S. Fukumoto, S. Ninomiya, and G. Silvestrov, "Table-top proton synchrotron ring for medical applications," *Proc. EPAC2000, Wien*, pp. 2515–2517, 2000.

[26] Y.-G. J. Hyung-Suck Suh and H.-S. Kang, "Magnet design of a proton and carbon-ion synchrotron for cancer therapy," *Journal of the Korean Physical Society*, vol. 56, no. 6, pp. 1947–1952, June 2010.

[27] E. Levichev, V. Parkhomchuk, S. Rastigeev, A. Skrinsky, V. Vostrikov, B. S. RAS, and M. Kumada, "Carbon ion accelerator facility for cancer therapy,"

[28] F. M. Khan, *The physics of radiation therapy, Third Edition.* Lippincott Williams & Wilkins, 2003.

[29] P. J. B. Ph.D, "Therapy physics review course: Radiation generators," *Biological Effects of Ionizing Radiation*, July 17th, 2010.

[30] D. Brenner and W. Huda, "Effective dose: A useful concept in diagnostic radiology?," *Radiation protection dosimetry*, vol. 128, no. 4, pp. 503–508, 2008.

[31] J. SEUNTJENS, W. STRYDOM, and K. SHORTT, "Dosimetric principles, quantities and units,"

[32] U. Food and D. Administration, "Principles of radiation protection," *Biological Effects of Ionizing Radiation*, January 2006.

[33] S. Khaled and K. D. Held, "Radiation biology: a handbook for teachers and students," *International Journal of Radiation Biology*, vol. 88, no. 11, pp. 858–859, 2012.

[34] N. Franken, R. ten Cate, P. M. Krawczyk, J. Stap, J. Haveman, J. Aten, and G. W. Barendsen, "Comparison of rbe values of high-let alpha-particles for the induction of dna-dsbs, chromosome aberrations and cell reproductive death.," *Radiat Oncol*, vol. 6, pp. 64–64, 2011.

[35] N. Fukunaga-Johnson, H. M. Sandler, P. William McLaughlin, M. S. Strawderman, K. H. Grijalva, K. E. Kish, and A. S. Lichter, "Results of 3d conformal radiotherapy in the treatment of localized prostate cancer," *International Journal of Radiation Oncology* Biology* Physics*, vol. 38, no. 2, pp. 311–317, 1997.

[36] I. M. R. T. C. W. Group *et al.*, "Intensity-modulated radiotherapy: current status and issues of interest," *International Journal of Radiation Oncology* Biology* Physics*, vol. 51, no. 4, pp. 880–914, 2001.

[37] E. J. Hall, "Intensity-modulated radiation therapy, protons, and the risk of second cancers," *International Journal of Radiation Oncology* Biology* Physics*, vol. 65, no. 1, pp. 1–7, 2006.

[38] E. M. Quan, X. Li, Y. Li, X. Wang, R. J. Kudchadker, J. L. Johnson, D. A. Kuban, A. K. Lee, and X. Zhang, "A comprehensive comparison of imrt and vmat plan quality for prostate cancer treatment," *International Journal of Radiation Oncology* Biology* Physics*, vol. 83, no. 4, pp. 1169–1178, 2012.

[39] D. Palma, E. Vollans, K. James, S. Nakano, V. Moiseenko, R. Shaffer, M. McKenzie, J. Morris, and K. Otto, "Volumetric modulated arc therapy for delivery of prostate radiotherapy: comparison with intensity-modulated radiotherapy and three-dimensional conformal radiotherapy," *International Journal of Radiation Oncology* Biology* Physics*, vol. 72, no. 4, pp. 996–1001, 2008.

[40] S. Kumar, R. Holla, P. Sukumar, S. Padmanaban, and N. Vivekanandan, "Treatment planning and dosimetric comparison study on two different volumetric modulated arc therapy delivery techniques," *Reports of Practical Oncology & Radiotherapy*, vol. 18, no. 2, pp. 87–94, 2013.

[41] *Proton therapy: scattering versus scanning*, 2015 (accessed April 01, 2015).

[42] S. Yonai, N. Kanematsu, M. Komori, T. Kanai, Y. Takei, O. Takahashi, Y. Isobe, M. Tashiro, H. Koikegami, and H. Tomita, "Evaluation of beam wobbling methods for heavy-ion radiotherapy," *Medical physics*, vol. 35, no. 3, pp. 927–938, 2008.

[43] J. Krimmer, L. Balleyguier, J. Baudot, S. Brons, L. Caponetto, M. Chabot, X. Chen, M. Dahoumane, D. Dauvergne, M. De Rydt, *et al.*, "Real-time online monitoring of the

ion range by means of prompt secondary radiations," in *Proceedings of Advancements In Nuclear Instrumentation Measurement Methods And Their Applications (ANIMMA), 2013 3rd International Conference On*, 2013.

[44] W. Enghardt, P. Crespo, F. Fiedler, R. Hinz, K. Parodi, J. Pawelke, and F. Pönisch, "Charged hadron tumour therapy monitoring by means of pet," *Nuclear Instruments and Methods in Physics Research Section A: Accelerators, Spectrometers, Detectors and Associated Equipment*, vol. 525, no. 1, pp. 284–288, 2004.

[45] R. Cédric and J. M. LETANG, "Design study of a compton camera for prompt-gamma imaging during ion beam therapy,"

[46] G. W. Phillips, "Gamma-ray imaging with compton cameras," *Nuclear Instruments and Methods in Physics Research Section B: Beam Interactions with Materials and Atoms*, vol. 99, no. 1, pp. 674–677, 1995.

[47] M. Singh and D. Doria, "Single photon imaging with electronic collimation," *Nuclear Science, IEEE Transactions on*, vol. 32, no. 1, pp. 843–847, 1985.

[48] J. Martin, G. Knoll, D. Wehe, N. Dogan, V. Jordanov, N. Petrick, and M. Singh, "A ring compton scatter camera for imaging medium energy gamma rays," *Nuclear Science, IEEE Transactions on*, vol. 40, no. 4, pp. 972–978, 1993.

[49] T. Kamae, N. Hanada, and R. Enomoto, "Prototype design of multiple compton gamma-ray camera," *Nuclear Science, IEEE Transactions on*, vol. 35, no. 1, pp. 352–355, 1988.

[50] J. McKisson, P. Haskins, G. Phillips, S. King, R. August, R. Piercey, and R. Mania, "Demonstration of three-dimensional imaging with a germanium compton camera," *Nuclear Science, IEEE Transactions on*, vol. 41, no. 4, pp. 1221–1224, 1994.

[51] T.-T. Chang, "Extremely high-granularity digital tracking calorimeter for the detection of scattered protons in proton computed tomography,"

[52] P. Ortega, I. Torres-Espallardo, F. Cerutti, A. Ferrari, J. Gillam, C. Lacasta, G. Llosá, J. Oliver, P. Sala, P. Solevi, *et al.*, "Noise evaluation of compton camera imaging for proton therapy," *Physics in medicine and biology*, vol. 60, no. 5, p. 1845, 2015.

[53] I. L. Castelhano, "Development of a compton camera for prompt-gamma detection in hadron therapy," 2014.

[54] Y. Matsuoka, T. Tanimori, H. Kubo, A. Takada, J. Parker, T. Mizumoto, Y. Mizumura, S. Iwaki, T. Sawano, S. Komura, *et al.*, "Performance of a new electron-tracking compton camera under intense radiations from a water target irradiated with a proton beam," *arXiv preprint arXiv:1412.3918*, 2014.

[55] J. H. P. C. H. K. C. S. L. S.-J. L. D. S. L. Soo Mee Kim, Hee Seo and J. S. Lee, "Resolution recovery reconstruction for a compton camera," *Medical physics and Nuclear Medicine*, 8 April 2013.

[56] P. Henriquet, E. Testa, M. Chevallier, D. Dauvergne, G. Dedes, N. Freud, J. Krimmer, J. Létang, C. Ray, M. Richard, *et al.*, "Interaction vertex imaging (ivi) for carbon ion therapy monitoring: a feasibility study," *Physics in medicine and biology*, vol. 57, no. 14, p. 4655, 2012.

[57] T. Li, Z. Liang, J. V. Singanallur, T. J. Satogata, D. C. Williams, and R. W. Schulte, "Reconstruction for proton computed tomography by tracing proton trajectories: A monte carlo study," *Medical physics*, vol. 33, no. 3, pp. 699–706, 2006.

[58] M. Petterson, N. Blumenkrantz, J. Feldt, J. Heimann, D. Lucia, A. Seiden, D. Williams, H.-W. Sadrozinski, V. Bashkirov, R. Schulte, *et al.*, "Proton radiography studies for proton ct," in *Nuclear Science Symposium Conference Record, 2006. IEEE*, vol. 4, pp. 2276–2280, IEEE, 2006.

[59] D. Aadnevik, "Diagnostic imaging ii student project compton camera," pp. XV, 157 s. : ill., 2014.

[60] R. Schulte, V. Bashkirov, T. Li, Z. Liang, K. Mueller, J. Heimann, L. R. Johnson, B. Keeney, H.-W. Sadrozinski, A. Seiden, *et al.*, "Conceptual design of a proton computed tomography system for applications in proton radiation therapy," *Nuclear Science, IEEE Transactions on*, vol. 51, no. 3, pp. 866–872, 2004.

[61] S. Raychaudhuri, "Introduction to monte carlo simulation," in *Simulation Conference, 2008. WSC 2008. Winter*, pp. 91–100, IEEE, 2008.

[62] A. Ferrari, J. Ranft, P. R. Sala, and A. Fassò, *Fluka Manual*. No. INFN-TC-2005-11, CERN, 2005.

[63] J. R. Styczynski, *Assessment of the use of prompt gamma emission for proton therapy range verification*. PhD thesis, Massachusetts Institute of Technology, 2009.

[64] R. M. Lindstrom, "Prompt-gamma activation analysis," *Journal of Research of the National Institute of Standards and Technology(USA)*, vol. 98, no. 1, pp. 127–133, 1993.

[65] H. M. Sommermann, "Microscopic description of giant resonances in highly excited nuclei," *Annals of Physics*, vol. 151, no. 1, pp. 163–203, 1983.

[66] J. M. Verburg, K. Riley, T. Bortfeld, and J. Seco, "Energy-and time-resolved detection of prompt gamma-rays for proton range verification," *Physics in medicine and biology*, vol. 58, no. 20, p. L37, 2013.

[67] S. Peterson, D. Robertson, and J. Polf, "Optimizing a three-stage compton camera for measuring prompt gamma rays emitted during proton radiotherapy," *Physics in medicine and biology*, vol. 55, no. 22, p. 6841, 2010.

[68] M. Singh, "An electronically collimated gamma camera for single photon emission computed tomography. part i: Theoretical considerations and design criteria," *Medical Physics*, vol. 10, no. 4, pp. 421–427, 1983.

[69] T. Hebert, R. Leahy, and M. Singh, "Three-dimensional maximum-likelihood reconstruction for an electronically collimated single-photon-emission imaging system," *JOSA A*, vol. 7, no. 7, pp. 1305–1313, 1990.

[70] J. Nuyts, C. Michel, and P. Dupont, "Maximum-likelihood expectation-maximization reconstruction of sinograms with arbitrary noise distribution using nec-transformations," *Medical Imaging, IEEE Transactions on*, vol. 20, no. 5, pp. 365–375, 2001.

[71] M. Jiang and G. Wang, "Convergence of the simultaneous algebraic reconstruction technique (sart)," *Image Processing, IEEE Transactions on*, vol. 12, no. 8, pp. 957–961, 2003.

[72] L. C. Parra, "Reconstruction of cone-beam projections from compton scattered data," *Nuclear Science, IEEE Transactions on*, vol. 47, no. 4, pp. 1543–1550, 2000.

[73] A. Andreyev, A. Sitek, and A. Celler, "Stochastic image reconstruction method for compton camera," in *Nuclear Science Symposium Conference Record (NSS/MIC), 2009 IEEE*, pp. 2985–2988, IEEE, 2009.

[74] R. Brun, F. Rademakers, P. Canal, I. Antcheva, and D. Buskulic, "Root users guide 5.16," 2007.

[75] J. Beebe-Wang, P. Vaska, F. Dilmanian, S. Peggs, and D. Schlyer, "Simulation of proton therapy treatment verification via pet imaging of induced positron-emitters," in *Nuclear Science Symposium Conference Record, 2003 IEEE*, vol. 4, pp. 2496–2500, IEEE, 2003.

[76] A. Zoglauer and G. Kanbach, "Doppler broadening as a lower limit to the angular resolution of next-generation compton telescopes," in *Astronomical Telescopes and Instrumentation*, pp. 1302–1309, International Society for Optics and Photonics, 2003.

[77] A. H. Compton, "The spectrum of scattered x-rays," *Physical Review*, vol. 22, no. 5, p. 409, 1923.

A APPENDIX

APPENDIX ONE

FLUKA SCRIPT

A1) INPUT CARD

Input for the simulation of 160MeV Proton Pencil beam into Soft Tissue Phantom while using the HPGe block Compton Camera to detect Prompt Gammas

```
TITLE
* Set the defaults for precision simulation
DEFAULTS                                              HADROTHE
* Define the beam characteristics
BEAM         -0.16                   -0.01     -0.01         PROTON
* Define the beam position
BEAMPOS                      -5.
GEOBEGIN                                              COMBNAME
    0    0
* Black body
SPH blkbody    0.0 0.0 0.0 100000.0
* Void sphere
SPH void       0.0 0.0 0.0 10000.0
RPP target     -10. 10. -10. 10. 0.0 20.
RPP Ge         -16. 16. 18. 26. -6. 26.
END
* Void around
void         5 +void -target
             -Ge
BLKBODY      5 +blkbody -void-Ge
Ge           5 +Ge
* Target
TARGET       5 +target
END
GEOEND
MATERIAL        15.            1.82                   PHOSPHO
MATERIAL        16.            2.07                   SULFUR
MATERIAL        17.          0.003214                   CHLORINE
MATERIAL        19.           0.862                   POTASSIU
MATERIAL        30.           7.133                   ZINC
MATERIAL        32.           5.323                   GERMANIU
* Tissue soft (ICRP)
*
MATERIAL                      1.0                     TISSUEIC
COMPOUND   -0.104472  HYDROGEN  -0.23219    CARBON  -0.02488  NITROGENTISSUEIC
COMPOUND   -0.630238    OXYGEN  -0.00113    SODIUM  -0.00013  MAGNESIUTISSUEIC
COMPOUND    -0.00133   PHOSPHO  -0.00199    SULFUR  -0.00134  CHLORINETISSUEIC
COMPOUND    -0.00199  POTASSIU  -0.00023   CALCIUM    -5E-05     IRONTISSUEIC
COMPOUND      -3E-05      ZINC                          TISSUEIC
ASSIGNMA      VACUUM       void
ASSIGNMA    BLCKHOLE    BLKBODY
ASSIGNMA    TISSUEIC    TARGET
ASSIGNMA    GERMANIU         Ge
EMF
* energy threshold cutoffs for transporting photons in selected regions. Only Gammas of energy more than stated E-value are considered.
EMFCUT               0.0060            TARGET      void
* used to set Energy threshold for star scoring. hadron beam with E>50MeV is able to form star density. below this E, no stars are scored.
THRESHOL                          0.050            0.050
* Gamma thershold of 1MeV for their transport, E>1MeV for prompt gamma allowed else gamma  with E<1 due to
```

nuetrons and Annihilation gammas-PET not transported
PART-THR -0.001 PHOTON PHOTON 1. 0.0
* dose scoring
*USRBIN 10. DOSE -21. 10. 10. 20.EQdoseP
*USRBIN -10. -10. 0.0 50. 50. 120. &
* dose scoring
*USRBIN 10. ENERGY -21. 10. 10. 20.EnergyDep
*USRBIN -10. -10. 0.0 50. 50. 120. &
* dose scoring
*USRBIN 10. PHOTON -21. 10. 10. 20.gammaTar
*USRBIN -10. -10. 0.0 50. 50. 120. &
* stars formed due to incident Heavy-ion beam. Stars correlate to gamma yield. threshold=50MeV for star formation considered
*USRBIN 5. PROTON -21. 10. 10. 20.StarsDue2C
*USRBIN -10. -10. 0.0 50. 50. 120. &
* scoring stars produced by carbon ion particle
*SCORE BEAMPART
* gamma fluence
*USRBIN 10. PHOTON -21. 10. 5. 20.GammaFLU
*USRBIN -10. 4. 0.0 50. 50. 120. &
* gamma fluence by position
*USRBIN 10. PHOTON -21. 12. 32. 20.GammaPOS
*USRBIN -12. 30. 0.0 50. 50. 120. &
* filtering of photons from GammaFLU
*AUXSCORE USRBIN PHOTON GammaFLU 1.
*USRYIELD 124. PHOTON -24. TARGET void 1.yield
*USRYIELD 180. 0.0 100. 0.01 0.0 3. &
* dumping secondary gamma radiation
USERDUMP 100. 23. 7. 1. Dump
* Set the random number seed
RANDOMIZ 1.0
* Set the number of primary histories to be simulated in the run
START 1E7
STOP

APPENDIX TWO

A2) MGDRAW.F SCRIPTS

A2a.)
For extracting prompt gamma data using HPGE block Compton Camera

```
*=====================================================================*
*                                                                     *
*    USer dependent DRAWing:                                          *
*                                                                     *
*    Icode = 10x: call from Kaskad                                    *
*          100: elastic   interaction secondaries                     *
*          101: inelastic interaction secondaries                     *
*          102: particle decay  secondaries                           *
*          103: delta ray  generation secondaries                     *
*          104: pair production secondaries                           *
*          105: bremsstrahlung  secondaries                           *
*          110: decay products                                        *
*    Icode = 20x: call from Emfsco                                    *
*          208: bremsstrahlung secondaries                            *
*          210: Moller secondaries                                    *
*          212: Bhabha secondaries                                    *
*          214: in-flight annihilation secondaries                    *
*          215: annihilation at rest   secondaries                    *
*          217: pair production        secondaries                    *
*          219: Compton scattering     secondaries                    *
*          221: photoelectric          secondaries                    *
*          225: Rayleigh scattering    secondaries                    *
*          237: mu pair     production secondaries                    *
*    Icode = 30x: call from Kasneu                                    *
*          300: interaction secondaries                               *
*    Icode = 40x: call from Kashea                                    *
*          400: delta ray  generation secondaries                     *
*  For all interactions secondaries are put on GENSTK common (kp=1,np) *
*  but for KASHEA delta ray generation where only the secondary elec-  *
*  tron is present and stacked on FLKSTK common for kp=npflka          *
*                                                                     *
*=====================================================================*
*
      ENTRY USDRAW (ICODE, MREG, XSCO, YSCO, ZSCO )
      IF ( .NOT. LFCOPE ) THEN
        LFCOPE = .TRUE.
        IF ( KOMPUT .EQ. 2 ) THEN
          FILNAM = '/'//CFDRAW(1:8)//' DUMP A'
        ELSE
          FILNAM = CFDRAW
        END IF
*         OPEN ( UNIT = 55, FILE = "COMPTON.txt", STATUS = 'NEW')
*        OPEN ( UNIT = 56, FILE = "PHOTOELEC.txt", STATUS = 'NEW')
*         OPEN ( UNIT = IODRAW, FILE = FILNAM, STATUS = 'NEW', FORM =
*     &         'UNFORMATTED' )
      END IF
*      No output by default:
**********************************************************************************************************
* Output code following below:
**********************************************************************************************************
      IF (MREG .EQ. 4) THEN                                  ! if in the Target volume=blood phantom
```

```
      IF (LINEVT .AND. LOFLK (NPFLKA).EQ. 1) THEN                    !*Checking for inelastic collision events
c       *Loop over the secondaries of the inelastic interactions
        do 10 ip = 1, NP                                    ! Loop over all secondaries
          IF (KPART(ip) .EQ. 7) THEN                              ! if secondary is a gamma
            SPAUSR(1)=xsco                                  ! store x,y,z position of emitted photon
            SPAUSR(2)=ysco
            SPAUSR(3)=zsco
            SPAUSR(11)=TKI(ip)
            SPAUSR(7) = 130          !****£****!                ! tracking number linking prompt gammas emitted for
CS
       WRITE(41,*) XSCO,ysco,zsco,TKI(ip)                          ! position of secondaries in Target and emitted
KInetic Energy
          END IF                                            ! end photon selection
 10       continue
      END IF                                                ! end LINEVT selection
      END IF                                                ! end of Target volume

*************************TEST FOR INTERACTIONS IN THE Ge DETECTOR**********************
c  test tracking of a gamma for the first two interactions
      IF ( MREG .EQ. 3 ) THEN                                  !Check if in the Ge detector region
           if ( ICODE .EQ. 219 ) then                         ! if gamma is compton scattered
             ISPUSR(1) = JTRACK                               ! store type of incident particle
             sparek(4,npflka) = ETRACK                         ! use flag to store particle Energy before scattering [Eo]
        do 100 ip = 1, NP                                   !make a loop over all secondaries
        IF(KPART(ip).EQ. 7 .and. SPAUSR(7) .eq. 130) THEN       ! selecting only prompt photons using tracking
number=130
           ISPUSR(4)=KPART(ip)
           sparek(8,npflka) = 140        !****£****!           ! tracking number linking prompt gammas scattered for PE
           sparek(6,npflka) = TKI(ip)                         ! use flags to store position and
            sparek(7,npflka) =XSCO                            ! Kinetic energy values
            sparek(9,npflka) =YSCO
            sparek(10,npflka) =ZSCO
        WRITE(44,*) xsco,ysco,zsco,sparek(4,npflka),TKI(ip),            ! position of interaction, Eo, kine

    &     sparek(1,npflka),sparek(2,npflka),sparek(3,npflka)            ! Energy of scattered Gamma, recorded
                                                ! corresponding Gamma position in the Target
        END IF                                              ! end secondary gamma selection
 100      continue
            end if                                          ! end scatttering event
        IF (ICODE .EQ. 221) THEN                                ! test for occurrance of PhotoElectric effect
        sparek(5,npflka) = ETRACK                               ! Store Energy of Incident Photon in flag
        ISPARK(9,npflka) = Jtrack                           ! Store Incident particle = gamma in flag
c         sparek(11,npflka) = SPAUSR(1)
          if( sparek(8,npflka).EQ. 140) then                    ! if photon was CS first in the scattering Ge detector

     WRITE(61,*) xsco,ysco,zsco,sparek(5,npflka),sparek(7,npflka),       ! print all quantities of tracked photon
    &  sparek(9,npflka),sparek(10,npflka),sparek(4,npflka),             ! from PE to CS and finally to LINEVT
    &  sparek(6,npflka),sparek(1,npflka),sparek(2,npflka),              ! using flags
    &  sparek(3,npflka),sparek(11,npflka)
          else
C           WRITE(61,*) 'PE not from first CS'
          end if                                            ! end prompt gamma selection
        END IF                                              ! end PE process
      END IF                                                    ! end detector region

******************** EXTRA TEST*********************************************
      IF (MREG .EQ. 4) THEN                                     ! if in the Target volume=blood phantom
      IF (LINEVT) THEN                                         !*Checking for inelastic collision events
```

```
c       *Loop over the secondaries of the inelastic interactions
         do 20 p = 1, NP                                    ! Loop over all secondaries
            IF (KPART(p) .EQ. 7 .and. TKI(p).le. 0.002) THEN          ! if secondary is a gamma
        WRITE(100,*) ZSCO,TKI(p)                            ! position of secondaries in Target and emitted KInetic
Energy
        ELSE IF(KPART(p) .EQ. 7 .and. TKI(p).GT. 0.002 .and.
     &      TKI(p).LE. 0.004) THEN                          ! ENERGY selection between 2-4MeV
        WRITE(200,*) ZSCO,TKI(p)
       ELSE IF(KPART(p) .EQ. 7 .and. TKI(p).GT. 0.004 .and.
     &      TKI(p).LE. 0.005) THEN                          ! ENERGY selection between 4-5MeV
        WRITE(200,*) ZSCO,TKI(p)
       ELSE IF(KPART(p) .EQ. 7 .and. TKI(p).GT. 0.005 .and.
     &      TKI(p).LE. 0.006) THEN                          ! ENERGY selection between 5-6MeV
        WRITE(200,*) ZSCO,TKI(p)
       ELSE IF(KPART(p) .EQ. 7 .and. TKI(p).GT. 0.006 .and.
     &      TKI(p).LE. 0.020) THEN                          ! ENERGY selection between 6-20MeV
        WRITE(200,*) ZSCO,TKI(p)
            END IF                                          ! end photon selection
 20      continue
      END IF                                                ! end LINEVT selection
      END IF                                                ! end of Target volume
************************************ END OF EXTRA TEST ******************************
* End of Active test code
       CONTINUE
      RETURN
*============= End of subrutine Mgdraw ====================================*
      END
```

A2) MGDRAW.F SCRIPT

A2b.)

For extracting prompt gamma data using Single scattering Compton Camera

```
*      No output by default:
*********************************************************************************************
* Output code write by SSENTONGO MARTIN follows below:
*********************************************************************************************
      IF (MREG .EQ. 5) THEN                                 ! if in the Target volume=blood phantom
      IF (LINEVT .AND. LOFLK (NPFLKA).EQ. 1) THEN          !*Checking for inelastic collision events
c       *Loop over the secondaries of the inelastic interactions
         do 10 ip = 1, NP                                   ! Loop over all secondaries
            IF (KPART(ip) .EQ. 7) THEN                            ! if secondary is a gamma
               SPAUSR(1) =xsco                              ! store x,y,z position of emitted photon
               SPAUSR(2)=ysco
               SPAUSR(3)=zsco
               SPAUSR(11)=TKI(ip)
               SPAUSR(7) = 130          !****£****!               ! tracking number linking prompt gammas emitted for CS
      WRITE(41,*) XSCO,ysco,zsco,TKI(ip),JTRACK                          ! position of secondaries in Target and emitted
KInetic Energy
            END IF                                          ! end photon selection
 10      continue
      END IF                                                ! end LINEVT selection
      END IF                                                ! end of Target volume
*********  TEST FOR INTERACTIONS IN THE SCATTER DETECTOR eg (Si)*************
      IF ( MREG .EQ. 3 ) THEN                                   !Check if in the si detector region
            if ( ICODE .EQ. 219 ) then                          ! if gamma is compton scattered
               ISPUSR(1) = JTRACK                               ! store type of incident particle
               sparek(4,npflka) = ETRACK                            ! use flag to store particle Energy before scattering [Eo]
         do 100 ip = 1, NP                                  !make a loop over all secondaries
```

```
        IF(KPART(ip).EQ. 7 .and. SPAUSR(7) .eq. 130) THEN           ! selecting only prompt photons using tracking
number=130
            ISPUSR(4)=KPART(ip)
            sparek(8,npflka) = 140        !****£****!               ! tracking number linking prompt gammas scattered for PE
            sparek(6,npflka) = TKI(ip)                             ! use flags to store position and
             sparek(7,npflka) =XSCO                                 ! Kinetic energy values
             sparek(9,npflka) =YSCO
             sparek(10,npflka) =ZSCO
          WRITE(44,*) xsco,ysco,zsco,sparek(4,npflka),TKI(ip),            ! position of interaction, Eo, kine
     &     sparek(1,npflka),sparek(2,npflka),sparek(3,npflka)             ! Energy of scattered Gamma, recorded
                                                                 ! corresponding Gamma position in the Target
        END IF                                                    ! end secondary gamma selection
 100      continue
            end if                                               ! end scatttering event
      END IF                                                      ! end of Ge scatterer detector region
*---------------------------------------- Final region-------------------------------------------------------
**** TEST OF PHOTOELECTRIC EFFECT IN Ge1 REGION WHICH IS ABSORBER DETECTOR**********
      IF ( MREG .EQ. 4 ) THEN                                     ! if in absorber detector region
         IF (ICODE .EQ. 221) THEN                                  ! test for occurrance of PhotoElectric effect
         sparek(5,npflka) = ETRACK                                 ! Store Energy of Incident Photon in flag
         ISPARK(9,npflka) = Jtrack                                ! Store Incident particle = gamma in flag
           if( sparek(8,npflka).EQ. 140) then                      ! if photon was CS first in the scattering Ge detector
      WRITE(61,*) xsco,ysco,zsco,sparek(5,npflka),sparek(7,npflka),       ! print all quantities of tracked photon
     &  sparek(9,npflka),sparek(10,npflka),sparek(4,npflka),          ! from PE to CS and finally to LINEVT
     &  sparek(6,npflka),sparek(1,npflka),sparek(2,npflka),           ! using flags
     &  sparek(3,npflka),sparek(11,npflka)
         write(63,*)sparek(11,npflka),sparek(4,npflka)
           else
c            WRITE(62,*) 'PE not from first CS'
           end if                                                 ! end prompt gamma selection
         END IF                                                    ! end PE process
      END IF                                                       ! END Ge1 absorber detector region
*****************************end Pe selection*****************************
* End of Active test code
       CONTINUE
      RETURN
*=============== End of subrutine Mgdraw ===================================*
      END
```

APPENDIX THREE

A3) FORTRAN SCRIPT

This Fortran 77 script computes all required calculations for the algorithm of Compton cone reconstruction using the calculated Compton angle

```
      program inpdat
c
c  This program opens a file to calculate cone circle centres with their radii
c Declaration of variables
      integer nmax, n
      parameter (nmax=1000000, u=20)
      double precision w(nmax),x(nmax), y(nmax), z(nmax)
      double precision ww(nmax),xx(nmax),yy(nmax),zz(nmax)
      double precision aa(nmax),bb(nmax),cc(nmax),rr(nmax)
      double precision kk(nmax),pet(nmax),ll(nmax),zw(nmax)
      double precision d(nmax), s(nmax),zzz(nmax),q(nmax)
      double precision j(nmax),k(nmax), l(nmax), m(nmax)
      double precision a(nmax), b(nmax), c(nmax),tt(nmax)
      double precision g(nmax), h(nmax), o(nmax),p(nmax)
      double precision r(nmax), t(nmax), ee(nmax),f(nmax)
      double precision ss(nmax),xo(nmax),yo(nmax),zo(nmax)
      double precision dt(nmax),rc(nmax),qq(nmax),arm(nmax)
      double precision gd(nmax),num(nmax),sl(nmax),gs(nmax)
      double precision son(nmax),sk(nmax),armr(nmax),edep(nmax)
c  Open the data files obtained from mgdraw.f run program
      open (21, FILE='promptSINGLE_1e7proton.txt',
     &          STATUS='OLD')
c  Loop over the data points in the file
      do 10 i= 1, 100000000, 1
c  Read its parameters PE,CS and TARGET (LINEVT) quantities
       read(21,*) j(i),k(i),l(i),m(i),w(i),x(i),y(i),zzz(i),              ! m=E1, zzz=Eo, z= kine of scattered
photon, zw=kine of LINEVT photon
     &    z(i),a(i),b(i),c(i),zw(i)                                    ! j,k,l=PE position, w,x,y= PE position
AND a,b,c= LINEVT position
c calculation of compton angle using energy deposition
      q(i)=1-(0.511*1e-3*((1/m(i))-(1/zzz(i))))
      if (q(i).ge.-1 .and. q(i).le. 1) then
      d(i)=acos(q(i))                              ! calculate the compton angle in radians, 0 to +pi
      t(i)=d(i)*(180.0/3.14159)                         ! convert rad to degrees
c+++++++++++++++++++++++++++++++++++++++++++++++++++++++++++++++++++++++++++++++
      num(i)= ((w(i)-a(i))*(j(i)-w(i)))+((x(i)-b(i))*(k(i)-x(i)))+
     &   ((y(i)-c(i))*(l(i)-y(i)))
      sk(i)=sqrt(((a(i)-w(i))**2.0)+((b(i)-x(i))**2.0)+
     &       ((c(i)-y(i))**2.0))
      sl(i)=sqrt(((j(i)-w(i))**2.0)+((k(i)-x(i))**2.0)+
     &       ((l(i)-y(i))**2.0))
      gs(i)= num(i)/(sk(i)*sl(i)
```

```
      son(i)=acos(gs(i))
      gd(i)=son(i)*(180.0/3.14159)
c ----------------------------Detailed calculations for 3D geometry---------------------------------
* Equation of the line joining the CS and PE points in 3D space
* xx=j(i)+(tt(i)*(w(i)-j(i)))
* yy=k(i)+(tt(i)*(x(i)-k(i)))
* zz=l(i)+(tt(i)*(y(i)-l(i)))
*
* Direction vector of this line
* A=[(w(i)-j(i)) (x(i)-k(i)) (y(i)-l(i))]
*
* Lets calculate the main lengths of a right angled cone (ie) its slanting length and diagonal line
*
      ! calculate the slanting length of the cone in (cm) 3D space
      s(i)=sqrt(((a(i)-w(i))**2.0)+((b(i)-x(i))**2.0)+
     &       ((c(i)-y(i))**2.0))    ! for 3D (x,y,z)
!       *diagonal line or height
       h(i)=sqrt(((xo(i)-w(i))**2.0)+((yo(i)-x(i))**2.0)+
     &    ((zo(i)-y(i))**2.0))
*********************************************************************************************
* Drawing circles in the y-plane where the primary beam passes, yy=0
        tt(i)= (-k(i))/(x(i)-k(i))
        xo(i)=j(i)+(tt(i)*(w(i)-j(i)))
        yo(i)= 0.0
        zo(i)=l(i)+(tt(i)*(y(i)-l(i)))
! radius of cone base circle from position measurement
      rr(i)=sqrt((xo(i)-a(i))**2.0+(yo(i)-b(i))**2.0+(zo(i)-c(i))**2.0)
*********************************************************************************
! radius of a cone base circle calculated a function of the compton angle
     r(i)=sqrt(((h(i)**2.0)+(s(i)**2.0))-(2*h(i)*s(i)*cos(t(i))))
! energy deposited in scatterer detector
      edep(i)=zzz(i)-z(i)
      write(91,*) edep(i)*1000
! calculating ARM for angular resolution
      pet(i)=zzz(i)*1000
      armr(i)=abs(r(i)-rr(i))                    ! ARM measure
      arm(i)=abs(gd(i)-t(i))                     ! measure of angular resolution
      write(39,*) edep(i)*1000,pet(i),m(i)*1000          ! scatter degrees, Eo and E1

      if (pet(i) .lt. 0.1) then                  ! truncating off the 5% below 0.1MeV for Eo spectrum
      write(99,*) pet(i)
      end if
 !      if (armr(i).lt. 2 .AND. pet(i) .gt. 0.510 .and.
 !      if ( pet(i) .gt. 0.510 .and.
 !    &     pet(i).lt. 0.511) then                ! select PET PHOTONS only
!       if (armr(i).lt. .5 .and. pet(i) .ge. 0.1) then    ! for 12-C to illiminate Eo < 0.1MeV
      if (armr(i).lt. .8 ) then                  ! to compensate for energy uncertainities distoriating the
compton angle
  100 FORMAT(' ',F15.10,F15.10,F15.10)                    ! printing format
```

```
      write(31,100) a(i),b(i),c(i)                    ! printing interaction coordinates for proof
      write(32,100) w(i),x(i),y(i)                    !     "
      write(33,100) j(i),k(i),l(i)                    !     "
      write(34,*) arm(i),zzz(i),arm(i)                ! Print Desired Quantities
      write(35,*) t(i),m(i)*1000                      !  "
      write(36,*) pet(i), edep(i)*1000                !  "
      write(37,*) t(i),pet(i),arm(i)                  !  "
      write(38,*) zzz(i)*1000,t(i)                    !  "
  200 FORMAT(' ',F12.5,F12.5,F10.2)                   ! F11.8 means 11 space reserved bt 8 for
decimals
      write(110,200) xo(i),zo(i),r(i)          ! print centre coordinates (xo,zo) and radius of the circle.
      else
      end if                                          ! end compensation of uncertainities
      else
      end if                    ! end compton angle selection between 0 and 180 degrees
   10 enddo
      close (21)                                      ! clsoe .txt file
c  End of proram!
      end
```

APPENDIX FOUR

A4.) C++ SCRIPT

For Reconstruction of Compton cone circular bases to calculate intersection points of circles

```
//#include "Riostream.h"
//Reconstruct Compton Cone circles using centre of circle coordinates and radii
// By Ssentongo Martin
{
gROOT->Reset();
 c1 = new TCanvas("c1","set",600,600);

//        Make canvas square
 Double_t xmin = -10; // min x axis
 Double_t xmax = 10;  // max x axis
 Double_t ymin = 0; // min y axis
 Double_t ymax = 20; //
 c1->Range(xmin,ymin,xmax,ymax);
   string line;
          char buffer[350];
// declaring
  const Int_t n = 500000;                              //  500000 circles
  Double_t d,o,m,h,xx,ww,yy,zz,aa;
  Double_t sum;

  Double_t x[n],y[n],z[n], cnum1, cnum2, cnum3;
   Int_t nlines = 0, iline = 0, mline=1;
  ifstream myfile ("fort.110");                        // open file=point.txt
  if (myfile.is_open())                               // if open
  {
     printf("File opened\n");
    while ( getline (myfile,line) )                   // get line
    {
                if (line.length() > 3)                //  if the line is long enough
                {
                        nlines++;                     // increase count by 1
                                //     mixing C++  and  C  strings
                                sprintf(buffer,"%s",line.c_str());
                                //  NOTE the %lf factor          in reading
                                sscanf(buffer, "%lf  %lf  %lf  ",  &cnum1, &cnum2, &cnum3);
                            // testing printf next line
                            // printf("-- %8.3f, %8.3f, z=%8.3f\n", cnum1, cnum2, cnum3);
                                x[nlines-1]=cnum1;
                                y[nlines-1]=cnum2;
                             z[nlines-1]=cnum3;
                }
    }
  }
  else {
```

```
            cout << "File trouble\n";
  }
 TEllipse *eli[1000];                        //   each circle must be an object
//----------------calculating circle properties-----------------------------
 pFile = fopen("inters.txt","w+");
 for ( iline=0 ; iline<nlines; iline++)                          // start i loop
          {
              for ( mline=1 ; mline<nlines; mline++)              // start inner loop=m
          {
     d= sqrt(pow((x[iline]-x[mline]),2)+ pow((y[iline]-y[mline]),2));    // (d) Distance between two
circles
     sum=(z[iline]+z[mline]);                                    // adding two radii
            if( sum < d )                                  // if sum < d
   {
                                                  // print nothing
   }
   else if ((abs(z[iline]-z[mline])) > d)                          // absolute check
   {
                                                  // print nothing
   }
   else if (d==0 & z[iline]==z[mline])                             // concentric centres
   {
                                                  // print nothing
   }
  else
   {
      aa=(pow((z[iline]),2)-pow((z[mline]),2)+pow(d,2))/(2*d);
      m=x[iline]+(aa*(x[mline]-x[iline]))/d;
      o=y[iline]+(aa*(y[mline]-y[iline]))/d;
//       pp=(m,o)=(px,py)

// distance of intersection point from pp
      h=sqrt(pow(z[iline],2)-pow(aa,2));
// --------------------finding intersection points---------------------
      // first intersection point
      xx=m+(h*(y[mline]-y[iline])/d);
      yy=o-(h*(x[mline]-x[iline])/d);

      // second intersection point
      ww=m-(h*(y[mline]-y[iline])/d);
      zz=o+(h*(x[mline]-x[iline])/d);
   }
      if ((xx > 0 | ww > 0)&(xx != ww)&((zz > 0 & zz <= 20)|(yy > 0 & yy <= 20)))    // eliminating non
value figures
{
       fprintf(pFile," %8.5f  %8.5f \n %8.5f  %8.5f \n",xx,yy,ww,zz);  // print to file inters.txt
}
else
{
```

```
}
      }
//----------------- end of calculations----------------------------
//--------------DRAW CIRCLES FROM COLLECTED DATA-------------------
     eli[iline] = new TEllipse(x[iline],y[iline],z[iline],z[iline]);  // (x,y,r1,r2) equal radius r1=r2 to draw a
circle from an ellipse
     eli[iline]->SetFillStyle(0);
           eli[iline]->Draw();                  // centre of circle is (x,y)=(o,p)
//      printf("point circle  x=%8.3f, y=%8.3f, z=%8.3f\n",x[iline],y[iline],z[iline]);
  }
     fclose(pFile);   // close file
}
}
//---------------------------------------- End of Program----------------------------
```